Interrogating the Chemical Processes that Govern Solid-Electrolyte Interphase Growth with Molecular Simulations

Luke D. Gibson

A dissertation
submitted in partial fulfillment of the
requirements for the degree of

Doctor of Philosophy

University of Washington

2021

Reading Committee:
Jim Pfaendtner, Chair
Christopher J. Mundy
Eric M. Stuve

Program Authorized to Offer Degree:
Chemical Engineering

University of Washington

Abstract

Interrogating the Chemical Processes that Govern Solid-Electrolyte Interphase Growth with Molecular Simulations

Luke D. Gibson

Chair of Supervisory Committee: Jim Pfaendtner, Department of Chemical Engineering

A major cause of capacity fade in lithium-ion batteries (LIBs) can be attributed to the formation of the solid-electrolyte interphase (SEI), which is a layer that forms at the interface between the electrode surface and liquid electrolyte. Although this layer plays a key role in determining the lifetime of a battery, its growth mechanism and composition are still not well understood. In general, it is known that this layer is formed via the reductive decomposition of the liquid electrolyte solvent directly contacting the electrode, but there is still a lack of knowledge associated with the various reaction mechanisms that drive this process. This dissertation will cover three approaches we have taken to better understand the SEI growth process with molecular simulation techniques.

In the first part of this dissertation, I will discuss how we used reaction network exploration and density functional theory (DFT) to elucidate the role of common LIB electrolyte additives (fluoroethylene carbonate, FEC; and vinylene carbonate, VC) in oligomerization reactions during SEI growth. FEC and VC have been shown experimentally to greatly improve a battery's performance and longevity, but the underlying mechanisms driving this marked improvement is not well known. I will demonstrate how these additives modulate the SEI oligomerization process while explaining how these reactions connect to the observed improvement in battery performance.

In the second part of this dissertation, I will shift my focus toward understanding the thermodynamics and kinetics associated with the reduction of ethylene carbonate (EC) at the electrode-electrolyte interface, which is a commonly studied electrolyte solvent. Most studies employ DFT calculations with implicit solvent models to compute the necessary components that comprise the reduction potential, such as the ion solvation free energy. However, I will highlight how we used the potential distribution theorem, a statistical mechanics approach, to directly compute single-ion solvation free energies for the calculation of electrolyte reduction potentials and discuss how this differs from literature. In addition, I will present our use of Marcus theory to explore the kinetics of EC reduction, wherein we see an interesting competition between the thermodynamics and kinetics for EC reduction with and without a neighboring Li^+. To conclude the dissertation, I will discuss our ongoing work on using transition path sampling to characterize the role of interfaces on key electrolyte degradation reactions.

Table of Contents

List of Figures ..... **iii**
List of Tables ..... **vi**

1 Introduction **1**
1.1 Background & Motivation **1**
1.2 Computational Methods **4**
1.2.1 Molecular Dynamics 4
1.2.2 Density Functional Theory 5
1.2.3 Umbrella Sampling 6
1.2.4 Metadynamics 6

2 Solvent Oligomerization Pathways Facilitated by Electrolyte Additives During Solid-Electrolyte Interphase Formation **8**
2.1 Abstract **8**
2.2 Introduction **8**
2.3 Methods **13**
2.4 Results & Discussion **15**
2.4.1 Proposed Alkoxide Formation Mechanism 17
2.4.2 S_N1 Oligomerization Mechanism 18
2.4.3 S_N2 Oligomerization Mechanism 21
2.4.4 Acetal Carbon Formation 23
2.5 Conclusions **25**

3 Probing the Thermodynamics and Kinetics of Ethylene Carbonate Reduction at the Electrode-Electrolyte Interface with Molecular Simulations **27**
3.1 Abstract **27**
3.2 Introduction **27**
3.3 Methods **32**
3.3.1 Classical Molecular Dynamics (MD) 33
3.3.2 Potential Distribution Theorem (PDT) 33
3.3.3 Reduction Potentials 34
3.3.4 Reorganization Energies 34
3.4 Results & Discussion **36**
3.4.1 Solvation Free Energy 36
3.4.2 Reduction Potentials 40
3.4.3 Reorganization Energy 43
3.4.4 Prediction of Electron Transfer Rate Constants 45
3.5 Conclusions **46**

4 Reaction Coordinate Analysis of Electrolyte Degradation in Bulk vs. Interfacial Environments **48**
4.1 Introduction **48**
4.2 Methods **50**

4.2.1 Computational Details 50
4.2.2 Aimless Shooting 51
4.2.3 Likelihood Maximization 54
4.3 Preliminary Results 56
4.4 Future Work 57

5 Summary and Perspective for Future Work 59
5.1 Summary of Work 59
5.2 Outlook on Future Work 60

Appendix A: Commonly Used Notations 62
Appendix B: Supplementary Information for Chapter 2 63

References 69

List of Figures

Figure 1.1: Molecular structures of common electrolyte components. Acronym definitions can be found in the main text and in Appendix A. 2

Figure 2.1: (a) S_N1 and (b) S_N2 mechanisms for nucleophilic attack of an EC molecule by an ethoxide. (c) EC molecule with atomic labels. "E" subscripts denote atoms are part of, or bonded to, the ethyl group and "C" subscripts denote they belong to the carbonyl group. (d) Ring-opened EC radical anion (o-EC). 12

Figure 2.2: Reaction network of 4 EC molecules and 1 Li^+ with an extra electron. The boxed molecules indicate the node in the reaction network that contains the open-shell S_N1 adduct, as well as two intact EC molecules and CO_2. Constructed from ~50 separate reactive MD trajectories using *mdstates*. Although Li^+ was included in the simulations, it is not pictured in the reaction network. 16

Figure 2.3: Free energy diagram of ethoxide and ethenolate generation via hydrogen abstraction between two o-EC radicals. Reaction progress is shown along the x-axis. A single transition state is denoted by the double dagger (‡). 18

Figure 2.4: Free energy diagrams and mechanisms for a single step of S_N1 oligomerization in which an ethoxide (a) or radical o-EC (b) acts as the nucleophile. The gray pathway denotes that EC is being attacked, green is VC, and orange is FEC. Mechanisms shown below each diagram only depict the FEC case. Analogous mechanisms are seen for EC and VC systems and can be found in **Figure B-3**. Radical locations are denoted with a dot (•) in the radical mechanism in (b). EC-5, FEC-5, and VC-5 correspond to the transition states in the first reactive step. 20

Figure 2.5: Free energy diagrams and mechanisms for a single step of S_N2 oligomerization in which an ethoxide (a) or radical o-EC (b) acts as the nucleophile. The gray pathway denotes that EC is the electrophile in the mechanism and orange is FEC. Mechanisms shown below each diagram only depict the FEC case. Analogous mechanisms are seen for the EC system and can be found in **Figure B-5**. Radical locations are denoted with a dot (•) in the radical mechanism in (b). EC-9, FEC-9, EC-13, and FEC-13 correspond to the transition states in the first reactive step. 23

Figure 2.6: Mechanism for aldehyde formation for each of the terminal species in the FEC pathways. The species names along the right are simply the original molecule's name followed by an asterisk (*) to denote the aldehyde form. 24

Figure 2.7: Reaction energies (enthalpy and free energy) for the nucleophilic attack of an aldehyde by an alkoxide, shown in the upper-right, where X corresponds to each of the four labeled groups. The green bond in each of the groups can be considered the same bond in the shown reaction. The labels on the groups correspond to the reaction energies in the left plot. Radical locations are denoted with a dot (•) in FEC-7* and FEC-15*. 25

Figure 3.1: a) Snapshot of the hydroxyl-terminated graphite surface in contact with liquid EC. b) Molecular structure of EC and Li^+. Side views of the relaxed geometries of c) EC and d) EC^-,

highlighting inner-sphere reorganization. Carbon, oxygen, hydrogen, and lithium are denoted by gray, red, white, and green atoms, respectively. 29

Figure 3.2: Workflow for computing EC reduction potentials from solvation free energies. The same general workflow is also applied when computing Li^+ and s-EC reduction potentials. This highlights the connection between solvation free energies and predicted reduction potentials. 33

Figure 3.3: Thermodynamic cycles for a) $Li^+ + e^- \rightarrow Li$, b) $EC + e^- \rightarrow EC^-$, and c) $Li^+\cdots EC + e^- \rightarrow Li^+\cdots EC^-$ redox reactions. $\mu * X$ denotes the single ion solvation free energy in EC and $\Delta Asub \circ$ denotes the standard free energy of sublimation. E_{IP} and E_{EA} denote the ionization potential and electron affinity in vacuum, respectively. $X_{(solv)}$, $X_{(g)}$, $X_{(s)}$ denote solvated, gaseous, and solid phases, respectively, for species X. $\Delta Ab \circ X, Y$ denotes the standard binding energy between X and Y. The signs of thermodynamic quantities in the cycles arise from the transitions depicted by the arrows..... 37

Figure 3.4: a) Charging free energy profiles of EC and Li. From left to right, the charge of EC transitions from 0 to -1, whereas Li transitions from 0 to +1. b) Comparison of charging free energies computed with SMD (lighter shades) and PDT (darker shades). 38

Figure 3.5: Free energy of cavity formation for a hard sphere in ethylene carbonate up to the radius of Li^+. 39

Figure 3.6: Marcus parabolas along solvent coordinate for a) EC and b) s-EC. The black and red curves in (a) and (b) denote the reactant and product states, respectively, with outer-sphere reorganization energies labeled. Parabolas are shown for the case of $\Delta A'_{rxn} = 0$, which also corresponds to $\eta = 0$. c) Relationship between predicted rate constant for electron transfer and overpotential, η, for EC and s-EC. 45

Figure 4.1: Projection of two different 2-dimenstional free energy surfaces (top) onto a 1-dimensional free energy profile (bottom). Figure adapted from Ref. 146. 49

Figure 4.3: Example of the possible outcomes for a given shooting point with forward and reverse trajectories and two basins of interest. a) Accepted shooting point: trajectories commit to separate basins. b) Rejected shooting point: trajectories commit to the same basin. c) Inconclusive shooting point: one or both trajectories never commit to either basin. 53

Figure 4.4: Candidate shooting points are generated from accepted shooting points' forward and reverse trajectories. One candidate shooting point is a copy of the original and the other two candidate shooting points are taken Δt time steps into the forward and reverse trajectories.. 54

Figure 4.5: a) Free energy profile of the decarboxylation reaction along the distance coordinate between the CO_2 carbon and oxide oxygen without a Li^+ present. b) Committor probability distribution of the ideal (line) and estimated (bar) reaction coordinate at the transition state. 56

Figure 4.6: 2-dimensional free energy surface of decarboxylation reaction in the presence of a Li^+. 57

Figure A-1: Atom labels for EC, FEC, VC, and PC molecules. 62

Figure B-1: Reaction network of 1 FEC molecule, 3 EC molecules, and 1 Li+ with an extra electron. The boxed molecules indicate the node in the reaction network that contains the open-shell SN1 adduct with FEC, as well as two intact EC molecules and CO2. Constructed from ~50 separate reactive MD trajectories using mdstates. Although Li+ was included in the simulations, it is not pictured in the reaction network. 63

Figure B-2: Reaction network of 1 VC molecule, 3 EC molecules, and 1 Li^+ with an extra electron. The boxed molecules indicate the node in the reaction network that contains the open-shell S_N1 adduct with VC, as well as two intact EC molecules and CO_2. Constructed from ~50 separate reactive MD trajectories using *mdstates*. Although Li^+ was included in the simulations, it is not pictured in the reaction network. 63

Figure B-3: S_N1 mechanisms for combinations of EC and VC electrophiles and ethoxide and o-EC nucleophiles. 64

Figure B-4: Reaction diagram of VC-3 structure oligomerizing with an EC via S_N1(green) and S_N2 (gray) mechanisms. The S_N1 and S_N2 states along the reaction path correspond to the stable structures in Figure 1a and 1b in the main text, respectively. 64

Figure B-5: S_N2 mechanisms for EC with both ethoxide and o-EC nucleophiles. 65

List of Tables

Table 2.1: Model Electrolyte Systems for MD 13

Table 3.1: Reduction potentials for Li^+, EC, and s-EC with solvation free energies computed via PDT. Values in the first column are reported in Volts in the absolute scale, whereas all other columns are reported in Volts vs. Li^+/Li. The $\Phi Li+/Li\circ$ column corresponds to the Li^+/Li scale as computed in this work, whereas the $\Phi Li+/Li\circ,1.4\,V$ column represents reduction potentials in the Li^+/Li scale using the commonly applied relationship $\Phi Li+/Li\circ,1.4\,V = \Phi abs\circ -1.4\,V$. Columns with an additional 1.3 V represent the inclusion of the ring-opening reaction as discussed in the text. Although the last column closely matches the experimental value (0.8 V vs. Li^+/Li)[134], the origin of this lacks the self-consistency of using the Li^+/Li scale as computed in this work as discussed in the main text. 40

Table 3.2: Reduction potentials for Li^+, EC, and s-EC with solvation free energies computed via SMD implicit solvent model. Values in the first column are reported in Volts in the absolute scale, whereas all other columns are reported in Volts vs. Li^+/Li. The $\Phi Li+/Li\circ$ column corresponds to the Li^+/Li scale as computed in this work, whereas the $\Phi Li+/Li\circ,1.4\,V$ column represents reduction potentials in the Li^+/Li scale using the commonly applied relationship $\Phi Li+/Li\circ,1.4\,V = \Phi abs\circ -1.4\,V$. Columns with an additional 1.3 V represent the inclusion of the ring-opening reaction as discussed in the text. 41

Table 3.3: PBE/DZVP energies of bent and flat configurations of EC with net charges of 0 and -1 (relative to flat, neutral EC, i.e., **Figure 3.1c**). Inner-sphere reorganization energies for each charge state are shown on the right. All energies are in kcal/mol. 44

Table A-1: Glossary of acronym definitions used in main text. 62

Table B-1: Transition state (TS) structures with XYZ coordinates in Å. 65

Acknowledgments

This journey has been one of the most challenging experiences of my life and was only made possible through the unending support from everyone close to me. I want to first thank my dissertation committee for your support and guidance throughout my Ph.D.: Dr. Jim Pfaendtner, Dr. Christopher J. Mundy, and Dr. Eric Stuve. I want to give special thanks to my Ph.D. advisor, Dr. Jim Pfaendtner. Your support and mentorship throughout my degree has shaped me into the researcher and person that I am today. I would also like to give special thanks to Dr. Christopher J. Mundy, whose deep enthusiasm for science has taught me that doing good science should always come first.

I would like to thank fellow members of the Pfaendtner Research Group (PRG), past and present, for always being supportive and helpful at work and as friends. I would like to extend a special thank you to Dr. Sarah Alamdari, Dr. Janani Sampath, Dr. Chowdhury Ashraf, Dr. Christopher Fu, Orion Dollar, Jessica Kong, Sabiha Rustam, Nisarg Joshi, Kaylyn Torkelson, Dr. Josh Smith, Dr. Wesley Beckner, Dr. Stephanie Hare, and Isaiah Lemmon for making my time with the PRG always feel fun and welcoming.

I would not have made it to where I am today without the amazing teachers that have guided me throughout my entire academic career. Thank you, Dr. David A. C. Beck, Dr. Keith Forward, Dr. Doug MacIntire, and Elaine Preston.

I am eternally grateful for the many friends that I made during my time at UW. Thank you to Victor Hu, Dr. Neal Dawson-Elli, and Dr. Sheila Goodman—you three helped me find happiness during some of the hardest times, and I look forward to our future adventures. I want to also thank Erica Eggleton, Linnette Teo, Olaf Bergeson, Dr. Jaime Rodriguez, Ryan Gharios, Maria Politi, Evan Komp, and Nida Janulaitis—you all helped to make Seattle feel like home these past five and half years. Thank you to the friends from undergrad who stuck with me during my journey through graduate school, Daniel Adame, Josh Logue, James Bean III, Carmen Ocampo, Matthew Lopez, and LTJG Andrew Quan.

Finally, I want to thank my family for their love and support. Thank you to my parents, Bob and Marlene, you have worked so hard to help me achieve my dreams and I am forever grateful. Thank you to my brothers, Robby and Jackson, I know that I can always count on you for good laughs, as well as support during the hard times.

Dedication

To my Mom and Dad,

for everything you have done to help me succeed

1 Introduction

1.1 Background & Motivation

Energy storage needs are continually rising, especially as advances in alternative energy technology improve energy generation from sources such as solar, wind, and hydro. Further adding to this need, the automotive industry is continually shifting their production toward electric vehicles each year. Currently, many of these needs are expected to be provided by the lithium-ion battery (LIB), an extremely popular battery chemistry due to its high energy density. Despite the power and popularity of LIBs, they are not without their drawbacks.[1–4] A major limitation of LIBs is the loss of total charge capacity over time. Capacity loss can be classified into two categories: calendar aging and cycling aging.[1] Calendar aging refers to chemical degradation of the battery materials, e.g., dissolution of active material, phase changes in active material, and solid-electrolyte interphase (SEI) formation. Cycling aging refers to mechanical failure of the battery, e.g., lithium plating, separation from the current collector, and pulverization of active material due to volume changes.[1–4] It has been shown that calendar aging is the largest source of capacity fade in batteries, especially in the context of electric vehicles.[1] SEI growth is a major contributor to calendar aging and limiting its growth would lead to massive economic gains in the form of improved battery longevity.[1] Thus, this dissertation is focused on elucidating and characterizing the reaction mechanisms that facilitate the growth of this SEI layer that occurs at the electrode-electrolyte interface (EEI) in LIBs.

The SEI is a heterogenous layer that builds up on the anode of a battery during cycling as a result of the reductive decomposition of the electrolyte, which includes the Li^+ salt (commonly $LiPF_6$) and the solvent. Electrolyte solvents are commonly mixtures of ethylene carbonate (EC), dimethyl carbonate (DMC), ethyl methyl carbonate (EMC), etc. with additives that are also cyclic or linear carbonate species. Popular additives include fluoroethylene carbonate (FEC), vinylene carbonate (VC), and propylene carbonate (PC). The molecular structure of each species can be seen in **Figure 1.1** in the left panel. Frequently used acronyms and abbreviations can be found in **Table A-1** in Appendix A:.

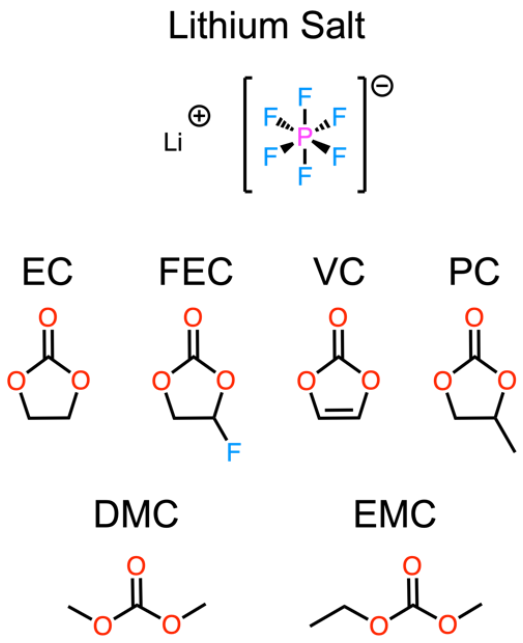

Figure 1.1: Molecular structures of common electrolyte components. Acronym definitions can be found in the main text and in Appendix A:.

The mechanisms by which the SEI layer forms are still debated in literature today,[5] but it is known that two zones exist within the SEI. The inner SEI consists of mostly inorganic compounds such as LiF, Li_2CO_3, and Li_2O, while the outer SEI consists of organic polycarbonates and polyoxides, such as lithium ethyl dicarbonate (Li_2EDC), lithium butyl dicarbonate (Li_2BDC), and polyethylene oxide (PEO). However, the SEI composition likely includes many more species and is highly complex in nature.[6–9]

Many studies have examined the degradation mechanisms of EC following 1 or 2 electron (1*e* or 2*e*) reduction and have agreed upon common degradation pathways.[10–12] Upon 1*e* reduction, the carbonate group in EC will lose its planarity with the carbonyl carbon (herein referred to as C_C) extending out of the plane. This reduced structure of EC that is still cyclic is referred to as c-EC^-. After reduction, c-EC^- can either undergo a ring-opening reaction or accept a second reduction electron. The common ring-opening reaction occurs at the bond between one of the ethyl carbons (C_E) and the adjacent oxygen (O_E) to form an o-EC^- species. Atom labels for electrolyte molecules can also be seen in **Figure A-1** of Appendix A:. Another possible ring-opening reaction can occur at the C_C-C_E bond to form $OCOC_2H_4O^-$. If c-EC^- becomes reduced a second time, it will either degrade into CO and $OC_2H_4O^{2-}$ or CO_3^{2-} and C_2H_4 spontaneously. Alternatively, both ring-opened structures, o-EC^- and $OCOC_2H_4O^-$, can become further reduced to spontaneously form CO +

$OC_2H_4O^{2-}$ and CO_3^{2-} + C_2H_4, respectively. However, these degradation reactions only represent commonly seen species and are not representative of all possible pathways.

Due to the small length scale and high reactivity of the SEI, experiments have struggled to gain insight into the layer's composition with molecular resolution. Despite these difficulties, Li, et al. have used cryo-electron microscopy (EM) to freeze a LIB and image the battery materials without compromising their chemical composition.[13] In their study, they were able to identify crystalline and amorphous regions within the SEI for various electrolytes, as well as Li dendrite formation.[13]

Studies using cryo-EM, however, are limited, likely due to the highly complex nature of the technique. Other common experimental approaches in SEI characterization are spectroscopic techniques. In a two-part study, Shkrob, et al. have used electron paramagnetic spectroscopy to detect reactive radical intermediates during SEI growth[14] and electrospray ionization tandem mass spectroscopy (ESI MS/MS) and nuclear magnetic resonance (NMR) spectroscopy to identify cross-linked polymeric structures in the SEI[15]. In these two studies, Shkrob, et al. proposed mechanisms that form branched polymeric networks in the SEI, which involve 1*e* reduction of the solvent followed by H-abstraction or 1,2-migration reactions to form more stable secondary (EC) and tertiary (PC) radicals, which continue to polyermize.[14,15] These findings support the presence of cross-linked and branched polymeric species that have been found in the SEI.

Despite advances in imaging and spectroscopic techniques, experiments lack the ability to conclusively elucidate reaction mechanisms with molecular-scale resolution. Thus, molecular simulations have played an integral role in characterizing the SEI formation process with mechanistic detail. However, the reactive nature of the SEI and its growth process necessitates the use of expensive quantum chemical methods in order to facilitate the forming and breaking of bonds.

Computational studies have focused on the degradation mechanisms of EC and other carbonate-based electrolytes. The Balbuena group have pioneered the study of electrolyte breakdown with multiple ab initio approaches (DFT and condensed phase AIMD simulations), in which they studied EC, FEC, VC, and PC degradation in gas phase and implicit solvents,[11,12,16,17] electron transfer through SEI on a Si anode,[9] and EC degradation on an alucone coated Si surface.[18] In two studies, Leung, et al. demonstrated that EC degradation involved both 1*e* and 2*e* reduction mechanisms. Prior to these studies, EC degradation was believed to occur following only 1*e*

reduction.[10,19] A semi-empirical method trained on quantum chemistry data, known as ReaxFF,[20] has also been used to study explicit electrolyte degradation on length- and time-scales much larger than what is typically afforded to ab initio methods.[21–23] In these studies, SEI growth was simulated in real time and the results demonstrated the formation of oligomeric species via the reaction of o-EC^- with other c-EC^- or o-EC^- species.[22,23]

Great progress has been made, both computationally and experimentally, in improving our understanding of the SEI growth process, but there still remains large gaps in knowledge regarding the exact molecular mechanisms driving these processes. Elucidating reaction mechanisms with AIMD can be prohibitively computationally expensive due to the timescales on which chemical reactions occur, often ranging from nanoseconds to seconds. However, we leverage enhanced sampling and statistical methods that allow us to overcome the need for long simulation times.

In this dissertation, I will overview the general tools I have used throughout my projects, followed by three chapters that each describe my work on understanding SEI growth with computational methods. Lastly, I will conclude with an overall summary of my work and provide an outlook on potential future projects.

1.2 Computational Methods

This section briefly describes the general computational tools used throughout this dissertation, such as molecular dynamics, density functional theory, and enhanced sampling techniques.

1.2.1 Molecular Dynamics

Molecular dynamics (MD) is an algorithm that propagates a molecular system through time. At each time step (typically < 2 fs), the energy of the system and net forces on each atom are computed. These forces are then used to update nuclear coordinates following Newtonian mechanics.

Ab initio MD (AIMD) is a type of molecular dynamics in which the potential energy function is a quantum chemical Hamiltonian, whereas classical MD uses parameterized, analytical functions to evaluate the energies and forces within the system. In this dissertation, I use Born-Oppenheimer MD, which is a type of AIMD in which the electron structure is allowed to relax to

the ground state each time nuclear coordinates are changed (i.e., each MD time step), and only a single electronic state is considered (i.e., a single potential energy surface).

Due to the high frequency of function calls to the potential energy function, AIMD is limited by the level of theory that is used. Throughout this dissertation, I will use DFT-based AIMD, but I will also use semi-empirical methods that are parameterized from either experimental data (PM6[24]) or DFT data (DFTB[25]). These semi-empirical methods allow for the forming and breaking of bonds but require only a fraction of the time needed for DFT calculations. Thus, semi-empirical methods are leveraged to achieve larger systems and longer simulation times than what is typically feasible with DFT calculations. Phenomena seen in AIMD simulations with semi-empirical Hamiltonians are further examined using DFT.

1.2.2 Density Functional Theory

Kohn-Sham density functional theory (DFT) is a quantum chemistry method that builds off the Hartree-Fock (HF) approach and is used to evaluate energies and forces for a given set of nuclear coordinates. The energy generated from DFT can be broken down into its different components:

$$E_{\mathrm{DFT}} = E_{\mathrm{PE,N}} + E_{\mathrm{PE,N-e}} + E_{\mathrm{KE,e}} + E_{\mathrm{PE,e-e}} + E_{\mathrm{XC}}, \qquad 1.1$$

where $E_{\mathrm{PE,N}}$ is the potential energy of the nuclei, $E_{\mathrm{PE,N\text{-}e}}$ is the Coulombic attraction energy between nuclei and electrons, $E_{\mathrm{KE,e}}$ is the kinetic energy of the electrons, $E_{\mathrm{PE,e\text{-}e}}$ is the Coulombic repulsion between electrons, and E_{XC} is the exchange-correlation energy for electrons. Note that there is no term for the kinetic energy of the nuclei because of the Born-Oppenheimer approximation,[26] which argues that electronic motion is significantly faster than nuclear motion. Thus, the nuclear and electronic wavefunctions can be calculated separately and assumes that the nuclei are static during the evaluation of the electronic energy. In the case of AIMD, the kinetic energy of the system is calculated from nuclear motion classically, but does not affect DFT energy evaluations (i.e., nuclei are still considered frozen during DFT calculation).

DFT differs from HF by using approximate functionals to calculate the last term in Eq. (1.1), which use the electron density as their inputs, whereas HF calculates electron exchange energy exactly while neglecting electron correlation. This E_{XC} term is where the differences in DFT functionals occur, e.g., the Perdew-Berke-Ernzerhof (PBE) functional[27,28] and Becke 3-

parameter[29] Lee-Yang-Parr[30,31] (B3LYP) functional[32] calculate E_{XC} differently, but all other terms in Eq. (1.1) are typically calculated in the same way between the two methods.

1.2.3 Umbrella Sampling

One of the earliest methods of enhanced sampling is known as umbrella sampling (US),[33] in which harmonic restraints are applied to one or more collective variables (CVs) to force the system to sample configurations in high energy regions of phase space. A CV is any quantity that can be computed from the atomic coordinates of a molecular simulation, such as an interatomic distance or coordination number. By forcing the system to explore higher energy regions of phase space, the underlying free energy, *A*, can be recovered by reweighting the frames in the trajectory onto a CV of interest, which removes the effect of harmonic restraint.[34]

$$A\left[s\left(\vec{\boldsymbol{R}}\right)\right] = -k_B T \ \ln\langle\delta\left(s\left(\vec{\boldsymbol{R}}\right) - s^*\right) \beta V_{\text{bias}}(s^*)\rangle_{\text{bias}} \qquad 1.2$$

where $\vec{\boldsymbol{R}}$ denotes the atomic coordinates of the system, $s\left(\vec{\boldsymbol{R}}\right)$ is the CV of interest, k_B is Boltzmann's constant, T is the system temperature, $\beta = 1/k_{\text{B}}T$, δ is the Dirac delta function, $V_{bias}(s^*)$ is the bias from the harmonic restraint at s^*, and $\langle\cdots\rangle_{\text{bias}}$ denotes that averaging is done in the biased ensemble.

By repeating this process at multiple points along *s*, multiple segments of the free energy profile can be generated. Due to the existence of an additive constant to the free energy in each window, the profiles typically must be aligned to create a smooth, continuous free energy profile. This alignment can be achieved by using the weighted histogram analysis method (WHAM)[35] or the multistate Bennett acceptance ratio (MBAR)[36] method.

1.2.4 Metadynamics

Metadynamics (MetaD) is an enhanced sampling technique that allows thermodynamic and kinetic information to be extracted from MD simulations that are much shorter than what is typically required for thermodynamic and kinetic information (i.e., without enhanced sampling).

MetaD works by periodically applying a history-dependent bias potential along one or more CVs, encouraging the system to explore higher energy regions of phase space. The bias is added in the form of Gaussian hills with heights and widths defined by the user and, in the well-tempered variant of MetaD, the hill height is gradually reduced over time.[37] Herein, it is assumed

that all MetaD simulations are run with the well-tempered variant. The MetaD bias has the following functional form[37],

$$V_G(S,t) = \int_0^t dt'\, w(t')\, \exp\left(-\sum_{i=1}^{d} \frac{\left(S_i(\mathbf{R}) - S_i\left(\mathbf{R}(t')\right)\right)^2}{2\sigma_i^2}\right), \qquad 1.3$$

where the last term is the functional form of a *d*-dimensional Gaussian hill with a width of σ_i along S_i and $w(t')$ is the well-tempered hill height and has the form,

$$w(t) = w \exp\left(-\frac{V_G(S,t)}{k_B T}\right). \qquad 1.4$$

At long simulation times, the bias added can be used to reconstruct the underlying free energy landscape. However, for this free energy landscape to be accurate, it is paramount that the simulation first experiences convergence (i.e., all relevant thermodynamic observables have stabilized).

2 Solvent Oligomerization Pathways Facilitated by Electrolyte Additives During Solid-Electrolyte Interphase Formation[1]

2.1 Abstract

The solid-electrolyte interphase (SEI) layer formation is known to play an important role in determining the lifetime of lithium-ion batteries. A thin, stable SEI layer is linked to overall improved battery performance and longevity, however, the factors and mechanisms that lead to optimal SEI morphology and composition are not well understood. Inclusion of electrolyte additives (fluoroethylene carbonate, FEC; and vinylene carbonate, VC) is often necessary for improving SEI characteristics. To understand how these electrolyte additives impact SEI formation, molecular dynamics (MD) and density functional theory (DFT) simulations were employed to study the reaction networks and oligomerization pathways, respectively, for three systems containing ethylene carbonate (EC), a lithium ion, and FEC or VC. MD simulations suggest radical oligomerization pathways analogous to traditional oligomerization with nucleophilic alkoxide species via S_N1 reaction mechanisms. Both S_N1 and S_N2 mechanisms were studied for all three systems using DFT. Oligomerization reactions were studied with both a standard alkoxide species and a ring-opened EC radical as the nucleophiles and EC, FEC, and VC as the electrophiles. For all cases, FEC and VC exhibited lower free energy barriers and more stable adducts when compared with EC. We conclude that one of the roles of additives is to modify the oligomerization process of EC by introducing branching points (FEC) or termination points (VC).

2.2 Introduction

The need for reliable, long-term energy storage is rapidly growing, especially as renewable energy resources such as solar and wind become increasingly efficient. The lithium-ion battery (LIB) is an excellent candidate for long-term energy storage due to its high energy density; however, it suffers from irreversible capacity loss over its lifetime. There are many mechanisms that contribute to this capacity loss, such as lithium plating, dissolution of active material, separation of active material from the current collector, and solid-electrolyte interphase (SEI)

[1] Reproduced from L.D. Gibson and J. Pfaendtner. Solvent oligomerization pathways facilitated by electrolyte additives during solid-electrolyte interphase formation. Physical Chemistry Chemical Physics, 22, 21494-21503 (2020),[90] with permission from the PCCP Owner Societies.

formation.[38] SEI formation is considered a major contributor to overall capacity fade in LIBs and other similar battery chemistries.[5,38] Therefore, the formation of SEI and how this phenomenon proceeds in various chemical environments have remained active areas of research.[5,16,17,39–50]

SEI can form at both the cathode and anode interfaces likely via different mechanisms. At the cathode interface, the mechanisms that govern SEI growth are not yet fully understood. It is seen that the cathode can reduce energy barriers for ethylene carbonate (electrolyte solvent) decomposition and oligomerization in the presence of the PF_6^- anion (common Li^+ counterion).[51–53] However, the $LiPF_6$ pair is also known to decompose into LiF and a reactive PF_5 species independent of a particular electrode interface, which can give rise to PF_5-initiated reaction pathways.[53–55] At the other end of the battery at the anode interface, SEI growth is driven by reductive decomposition.[2,56,57] Further, at the anode side, the SEI is comprised of two zones: the inner, inorganic layer (e.g., Li_2O, LiF, Li_2CO_3) and the outer, organic layer (e.g., Li_2EDC, Li_2BDC, oligomeric species).[48,58,59] This current work is focused on understanding the mechanisms behind outer SEI growth at the anode interface wherein electron transfer is expected to be slow. Any mention of the SEI throughout the remainder of this chapter can be assumed to be referring to the anode side.

The products of these decomposition steps are believed to heavily impact the overall performance of the battery; however, it is difficult to get a clear picture of this product distribution experimentally due to the high reactivity of battery and SEI components. The models that describes how this reductive decomposition ultimately leads to the formation of the SEI layer are not fully developed and is still an ongoing area of research.[5,60] Understanding the mechanisms that drive SEI growth can grant insight into how this process can be controlled—for example, understanding how to minimize the layer thickness while still insulating the electrodes from further electrolyte decomposition.

Traditionally, a LIB is comprised of a graphitic anode, a metal oxide cathode, a separator, and an electrolyte. The electrolyte includes the Li^+ salt and the solvent. Electrolyte solvents are commonly mixtures of ethylene carbonate (EC), dimethyl carbonate (DMC), ethyl methyl carbonate (EMC), etc. with additives that are also cyclic or linear carbonate species. Popular additives are fluoroethylene carbonate (FEC) and vinylene carbonate (VC), which have been reported to increase cycling lifetime.[40] The inclusion of small weight fractions of these additives have been shown to improve a battery's performance and it is proposed that this marked

improvement is due to how the additives modulate the growth mechanisms and compositions of the SEI layer.[39,49] A previous study by Delp, et al.[61] found that the reduction potential for EC was ~0.5 V vs. Li^+/Li (often credited for SEI formation), whereas the FEC and VC calculated reduction potentials were 0.9 and 0.8 V vs. Li^+/Li, respectively. It was also found that FEC and VC do not have high affinities for populating the Li^+ solvation shell. And although FEC and VC have higher reduction potentials, Delp, et al. argue that high solvation shell populations are also important factors when predicting if additives are preferentially reduced over EC, thereby implying that FEC and VC may participate in SEI growth via mechanisms other than direct reduction.[61]

Experimental studies have looked at how FEC and VC affect cycling performance and how these improvements relate to the chemical structure of the SEI.[39,41,49] Wang, et al. performed a study in which they compared the performance of FEC and VC additives in lithium-ion pouch cells.[41] They found that the inclusion of either FEC or VC yielded better coulombic efficiency, increased cycle life, smaller capacity fade, lower gas generation, and lower voltage drop during storage when compared to the control (EC:EMC, 3:7 wt% ratio). Another set of recent studies highlighted the concentration dependence of FEC on Na-battery performance (both experimentally and theoretically), in which it was found that lower concentrations of FEC led to improved SEI characteristics over higher concentrations.[62,63] Two studies by Jin, et al. investigated the impact of FEC and VC additives on SEI composition for silicon nanowire LIBs.[39,49] They demonstrated a reduction in polyethylene oxide (PEO)-like species for FEC-containing systems when compared to EC/DMC systems using NMR techniques. Another important finding was the presence of cross-linking vinoxyl species that were generated from FEC-derived VC molecules. Furthermore, acetal carbons were shown to exist only in additive-containing systems and were attributed to the improved cross-linking of PEO polymeric species in the organic SEI. Jin, et al. argue that the FEC additive helps to suppress the formation of soluble decomposition products by enhancing the formation of insoluble decomposition products that deposit onto the SEI, further preventing electrolyte reduction.[39,41,49]

Although experiments have provided many insights, they are limited by their lack of molecular-scale resolution, which is often required for mechanistic studies. Battery systems are particularly difficult to study experimentally due to their highly reactive components. Therefore, studying the SEI without altering the underlying chemical structures often requires cryogenic temperatures as to mitigate any unwanted side reactions upon examination.[13] Molecular

simulations can help bridge this gap by using quantum chemistry and molecular dynamics to investigate mechanisms that would otherwise be infeasible experimentally. Specifically, molecular simulations have provided great insight into the role of electrolyte additives in SEI growth. In a hybrid Monte Carlo/molecular dynamics study for sodium ion batteries, FEC was linked to improved network formation in the SEI due to its strong dipole moment, which prevented the dissolution of degradation products even in cases when FEC did not participate in any degradation reactions.[47] Another group saw a similar effect in ab initio molecular dynamics (AIMD) simulations wherein FEC decomposed to form LiF and formed connections between lithium ethylene dicarbonate (Li_2EDC) species, thereby preventing the dissolution of the commonly seen degradation product.[43] Energy landscapes for EC oligomerization via S_N1 and S_N2 reaction mechanisms have also been calculated using density functional theory (DFT). Both pathways involve an alkoxide as the nucleophile which reacts with EC to form polyethylene carbonate (PEC) via an S_N1 mechanism or PEO via an S_N2 mechanism—both species that have been detected experimentally in the outer, organic zone of the SEI.[39,49,50] In S_N1 mechanisms, the carbonyl carbon in the carbonate group (C_C) is the electrophilic site of attack, whereas in S_N2 mechanisms, the ethyl carbons (C_E) are the electrophilic sites. A diagram with the atom labels for EC and both mechanisms are depicted in **Figure 2.1**. These PEO and PEC oligomeric species have also been detected in previous experimental studies, along with several other oligomeric compounds.[39,49,64,65]

Although many studied oligomerization mechanisms involve alkoxides behaving as nucleophiles,[15,39,49,50] it is often overlooked how these alkoxides are formed. There are likely many ways in which alkoxide species can form in carbonate-based electrolytes, but the most straightforward mechanism involves the decarboxylation of a terminal carbonate group to form a terminal oxide and CO_2.[48,50]

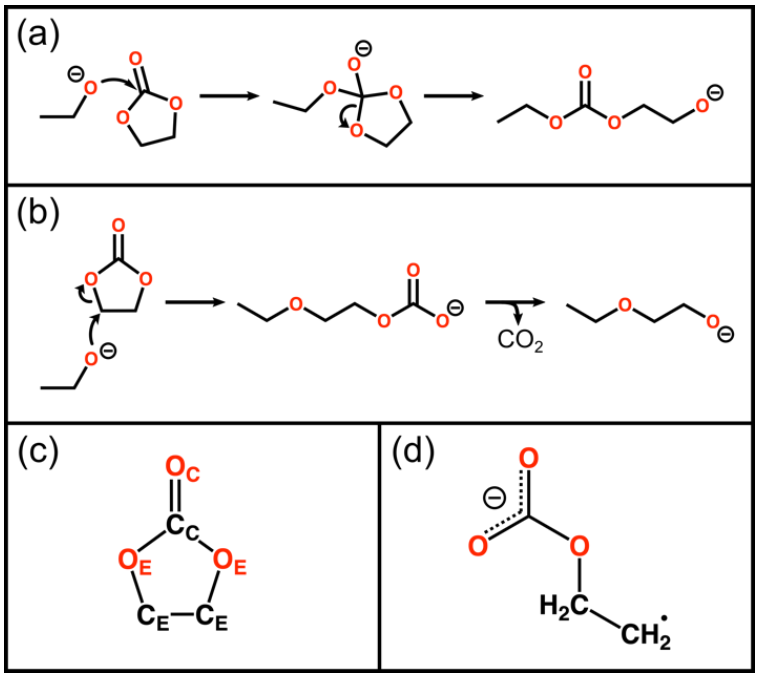

Figure 2.1: (a) S_N1 and (b) S_N2 mechanisms for nucleophilic attack of an EC molecule by an ethoxide. (c) EC molecule with atomic labels. "E" subscripts denote atoms are part of, or bonded to, the ethyl group and "C" subscripts denote they belong to the carbonyl group. (d) Ring-opened EC radical anion (o-EC).

Despite the current progress of simulations in understanding additive effects on SEI, there still exists a need to study these systems due to the highly complex chemical reaction networks involved in SEI growth. The role of electrolyte additives still remains unknown in the context of SEI oligomerization reactions, which is a process that has been shown to be important for EC systems.[50] To this end, we examined nucleophilic substitution pathways that include FEC and VC additives as the electrophiles, as well as ring-opened EC radical anions (o-EC, shown in **Figure 2.1d**) as a potential nucleophile. Firstly, we employed semi-empirical molecular dynamics (SEMD) simulations to explore the reaction networks of FEC or VC in the presence of EC, as well as a pure EC system as a control. For these SEMD simulations, we utilized a cost-effective Hamiltonian and enhanced sampling techniques to permit the exploration of these reaction networks. We then further verified key mechanisms that were observed with more accurate, hybrid functional DFT calculations to support our mechanistic conclusions.

Following the description of computational methods, the remainder of this chapter is organized as follows. We introduce the reaction networks that were sampled and discuss key

pathways that were observed. These key pathways are mechanistically verified with quantum chemistry calculations and the impact of the observed mechanisms are discussed. The chapter concludes with a brief summary of our findings and their impact.

2.3 Methods

To gain a better insight into how FEC and VC additives affect SEI formation mechanisms, we examined three model electrolyte systems, which are listed in **Table 2.1**.

Table 2.1: Model Electrolyte Systems for MD

System Name	System Composition
4EC	4 EC + 1 Li^+ + 1 e^-
3EC+FEC	3 EC + 1 FEC + 1 Li^+ + 1 e^-
3EC+VC	3 EC + 1 VC + 1 Li^+ + 1 e^-

We used molecular dynamics (MD) and density functional theory (DFT) to study SEI formation with molecular-scale resolution. All MD simulations were run with the system temperature set to 300 K using the Nosé-Hoover thermostat[66,67] in the NVT ensemble and with a time step of 1 fs. To emulate 1*e* reduction, the charge and multiplicity of each system were set to 0 and doublet, respectively. The MD simulations were run using the semi-empirical PM6 level of theory[68] in the CP2K quantum chemistry MD simulation package[69–74] with the PLUMED library[75]. While PM6 has not been used to study systems of electrolytes, we have chosen it because of its high computational efficiency as a quantum chemical method that permits reactive events. A recent study from our group demonstrated that PM6 was able to reproduce the reaction network of γ-ketohydroperoxide, a small hydrocarbon used in combustion applications.[76] Although PM6 may not quantitatively reproduce energy barriers or reaction energies for our systems, our MD simulations were aimed at exploring large reaction networks and not on recovering quantitative kinetic or thermodynamic data.

Despite the high efficiency of PM6, sufficiently sampling all of the available pathways remains an intractable problem. This is because chemical reactions are rare events that can often occur on time scales much longer than what is typically afforded to MD simulations. However, we overcome this barrier by utilizing enhanced sampling. Among many enhanced sampling methods, the metadynamics (MetaD) family of methods[34] has found frequent use for studying chemical

reaction networks.[77] To this end, we have used parallel bias MetaD[78] (PBMetaD) to bias all atomic SPRINT coordinates[79], for a total of around 40 CVs in each simulation, to enhance the rate at which chemical reactions occur. The PBMetaD framework allows for simultaneous application of multiple well-tempered MetaD[37] bias potentials, in this case all one-dimensional, on different CVs within a single simulation replica. This method of using PBMetaD+SPRINT has previously been shown to be an effective tool for reaction network exploration.[76,80] The biasing parameters used in this study used a 10 kJ/mol hill height, a hill width (σ) of 0.20 for all CVs, a deposition rate of 250 ps^{-1}, and a bias factor of 150. It should be noted that in the parallel bias framework of MetaD, the hill height is divided and scaled among all CVs that are receiving bias, which merits the rather large bias factor and hill heights compared to what is found in traditional MetaD simulations. Further, in a previous study in our group, there were no significant differences in observed reaction networks when using higher vs. lower biasing rates.[76] Although the biasing rate in this study is still higher than the maximum that is used in Ref. 76, our system contained five disconnected molecules or ions, thereby giving rise to a significantly increased number of CVs, which according to the PBMetaD theory leads to a proportional decrease in the individually applied biases at any given time.

For each system in **Table 2.1**, a minimum of 50 independent MD simulations were run for ~2.5 ns each to ensure sufficient sampling of reactive pathways, following the procedure of Ref. 76 in which a minimum of 45 independent MD simulations were performed due to the large phase space of SPRINT coordinates (i.e., reactive pathways). Simulations were run for ~2.5 ns because after which time, the reaction networks had converged up to secondary products (discussed in Results & Discussion). The respective simulation trajectories were analyzed using an automated reaction detection algorithm first developed in a previous study,[81] in which the molecular system is represented as a connectivity graph and treated as a hidden Markov model (HMM) to estimate the underlying connectivity by decoding the interatomic connection signals with the Viterbi algorithm. We implemented this procedure in a python package called *mdstates* to parse through trajectories and determine structures before and after reactive events, as well as compile the networks of all trajectories into a single reaction network.

All DFT calculations were performed using the quantum chemistry simulation package Gaussian 16[82] with the B3PW91 functional[29] and a 6-311++G(d,p) basis set, as well as an ultra-fine integration grid, which has been shown in literature to closely reproduce post-Hartree-Fock

energies for electrolyte decomposition systems in a cost effective manner.[12,83] An implicit water solvent model was used, as implemented by the conductor polarizable continuum model[84,85] (CPCM), but with a modified dielectric constant of 89.78 to more closely match that of liquid EC.[86] Any transition states reported below were optimized to a saddle point and verified to contain only a single imaginary frequency. Further, intrinsic reaction coordinate (IRC) calculations were performed to confirm the correct reactants and products were connected by their respective transition states. The structures for all transition states noted in this study can be found in **Table B-1**. Free energies reported herein were obtained via frequency calculations, which compute entropic contributions and zero-point energy corrections to enthalpy at a reference state (1 atm and 298.15 K) using the rigid rotor harmonic oscillator (RRHO) approximation.

2.4 Results & Discussion

In the first part of this study, we generated reaction networks for each of the systems in **Table 2.1** using SEMD simulations with the PBMetaD+SPRINT enhanced sampling scheme described above. The reaction network, up to secondary products, for the 4EC system can be seen in **Figure 2.2**. For some of the reaction pathways, many reactions beyond secondary products were discovered but the network only shows up to secondary products given the low likelihood that tertiary and higher order products would factor as important products. The important feature present in this network is the intermediate S_N1 adduct that is highlighted in **Figure 2.2**, which connects the observed pathway to previously seen pathways in literature, namely SEI oligomerization pathways.[50] In our case, the EC molecule has an open-shell ethoxy group bonded instead of the closed-shell molecule seen in **Figure 2.1a**. This adduct forms through the attack of an intact EC molecule by a ring-opened EC radical (o-EC), as opposed to an alkoxide that is proposed in literature.[50] During this process, a CO_2 molecule is lost as the linker oxygen in the carbonate group attacks the sp^2 carbon (C_C) in the neighboring EC, suggesting that this pathway may contribute to the CO_2 evolution that is seen experimentally during SEI growth.[87] This radical mechanism facilitates the initiation of electrolyte oligomerization with only a ring-opened EC radical, which is known to be one of the first species formed during EC degradation following 1*e* reduction.[12] For the FEC- and VC-containing systems, analogous pathways were seen that included the additives in the mechanism. The FEC and VC networks can be seen in **Figure B-1** and **Figure B-2**, respectively.

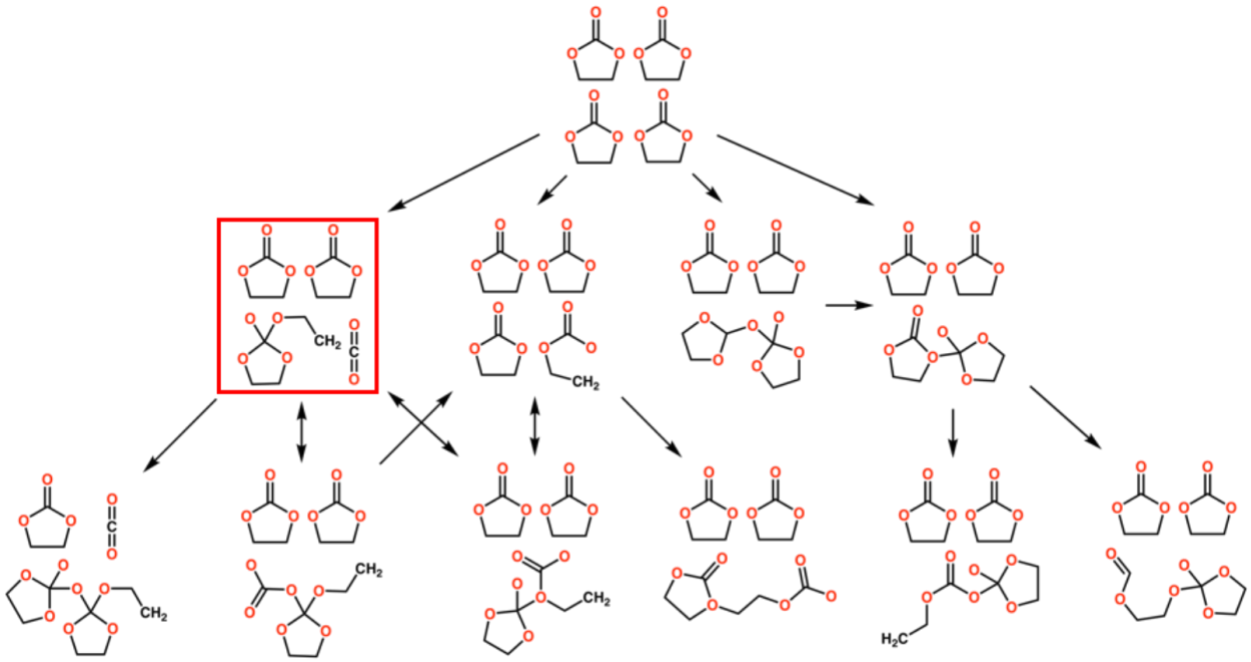

Figure 2.2: Reaction network of 4 EC molecules and 1 Li^+ with an extra electron. The boxed molecules indicate the node in the reaction network that contains the open-shell S_N1 adduct, as well as two intact EC molecules and CO_2. Constructed from ~50 separate reactive MD trajectories using *mdstates*. Although Li^+ was included in the simulations, it is not pictured in the reaction network.

In the following sections, we further analyze the S_N1 and S_N2 reaction mechanisms (the commonly studied oligomerization pathways) using DFT calculations to gain a more quantitative picture for these pathways with two types of nucleophiles: o-EC radical anion and ethoxide anion (the former being a novel aspect of this study and the latter being the typical nucleophile for SEI oligomerization). To further explore the use of ethoxide as a nucleophile for the studied reactions, we propose a short mechanism for its generation from two, intact EC molecules. Following this, for each nucleophilic substitution pathway, we examine how the presence of electrolyte additives (FEC and VC) impact the energetics of each reaction as compared to EC. And lastly, we connect some predicted additive oligomerization products in this study to cross-linking groups that have been experimentally linked to improved battery performance.[39,49]

2.4.1 Proposed Alkoxide Formation Mechanism

Although the observed reaction in the reaction network involved an o-EC radical, we also consider the analogous mechanisms with an ethoxide anion for comparison, which has previously been studied in the case of ethoxide-EC oligomerization.[50]

As mentioned previously, there are many potential mechanisms through which alkoxides can form as a result of electrolyte decomposition, although they are seldom discussed in literature. Herein, we propose a simple mechanism in which two o-EC radical anions react via hydrogen transfer to ultimately form ethoxide + CO_2 or ethenolate + CO_2, shown in **Figure 2.3**. The adduct formed after the hydrogen transfer is significantly more stable than the two o-EC radical anions, which is not surprising due to the reconciliation of the two radicals to form closed-shell structures. Computing the energy barrier separating these two states, however, is non-trivial and would require non-adiabatic calculations of the coupling between the singlet and triplet states along the reaction coordinate. This is beyond the scope of this study, but it provides an interesting point for further investigation. The formation of the two alkoxides are uphill in enthalpy, but the formation of the ethenolate exhibits a net decrease in free energy. The ethenolate species differs from ethoxide in two ways: 1) the formation of ethenolate passes through a transition state (denoted by the double dagger, ‡, in **Figure 2.3**), and 2) the molecular structure is resonance stabilized, allowing the negative charge to delocalize across the molecule. This resonance stabilization, however, discourages the ethenolate species from reacting any further via the nucleophilic substitution mechanisms discussed herein. The ethoxide formation process, on the other hand, does not pass through a transition state on the potential energy surface (i.e., no saddle point with a single imaginary frequency) and maintains the charge localization on the oxygen.

This hypothesized hydrogen transfer reaction is only one of many possible reactions that can occur between two o-EC radicals. Commonly seen structures that can stem from the reaction of two o-EC radicals are lithium ethylene dicarbonate (Li_2EDC) and lithium butylene dicarbonate (Li_2BDC).[8,86,88,89] For comparison, using the same reference and level of theory as in **Figure 2.3**, the free energies of reaction to form Li_2EDC + C_2H_4 or Li_2BDC from two o-EC radicals are -60.6 and -71.4 kcal/mol, respectively. This result demonstrates that the proposed H-transfer reaction step shares a similar free energy of reaction; however, we note that it is important to understand both the kinetic and thermodynamic aspects of a reaction to provide quantitative comparisons. Our

result simply demonstrates that the driving force for the H-transfer reaction step is comparable to that of Li_2EDC or Li_2BDC formation and will be further investigated in a future study.

This proposed mechanism for ethoxide formation is not necessarily expected to have a high rate of reaction in a battery due to the dependence on two o-EC radicals finding each other. However, this reaction can be thought of as an initiation reaction prior to oligomerization via the S_N1 and S_N2 mechanisms and thus does not require a high rate of reaction.

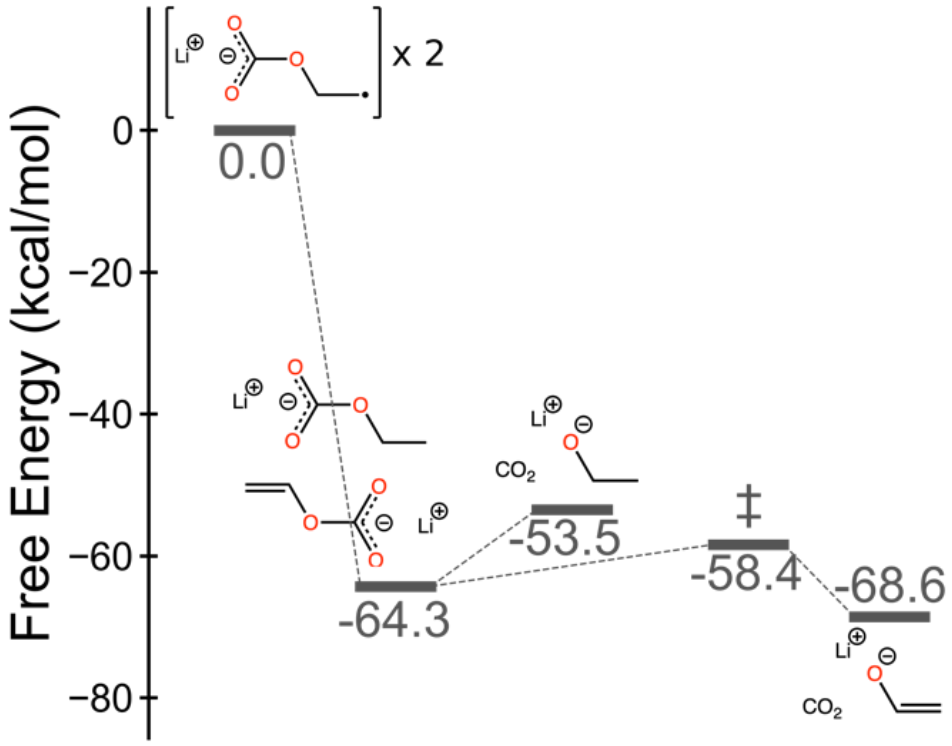

Figure 2.3: Free energy diagram of ethoxide and ethenolate generation via hydrogen abstraction between two o-EC radicals. Reaction progress is shown along the x-axis. A single transition state is denoted by the double dagger (‡).

2.4.2 S_N1 Oligomerization Mechanism

Free energy diagrams for the S_N1 oligomerization mechanism can be seen in **Figure 2.4**. Two mechanisms are considered in which either an ethoxide (**Figure 2.4a**) or o-EC radical (**Figure 2.4b**) act as the nucleophile. In both cases, EC, FEC, and VC are considered as electrophiles. Each state in **Figure 2.4** (and **Figure 2.5**) is arbitrarily labeled according to the electrophile of the pathway and the order of appearance (e.g., EC-1 is the first structure in the mechanism with EC as

the electrophile). Below each free energy diagram, the corresponding mechanism for FEC is shown. The EC and VC mechanisms are analogous and can be found in **Figure B-3**.

The ethoxide mechanism in **Figure 2.4a** is comprised of two reactions. The first step involves a change in configuration (not depicted) and attack of the ethoxide on the C_C of the electrophile. The reactive step of the ethoxide attacking the electrophile for each of the three pathways was a barrierless reaction and did not exhibit a transition state. Similarly, a transition state could not be located for the ring-opening reaction (second step) in the mechanism.

The EC pathway in the ethoxide mechanism (**Figure 2.4a**) exhibits relatively small changes in free energy (±1 kcal/mol). From the FEC and VC pathways, it is clear that the presence of a fluorine atom or double bond impacts the energy landscape for both the ethoxide and radical S_N1 mechanisms. We see for all reaction steps FEC and VC exhibit drops in energy, with FEC consistently ~3 kcal/mol lower in free energy than VC throughout the mechanisms. It is not expected that VC will continue to react via the same S_N1 mechanism with another EC because the final structure, VC-3, will sacrifice resonance stability of the oxide anion, as seen previously with the ethenolate species in **Figure 2.3**. The energetics behind further oligomerization from the VC-3 structure can be seen in **Figure B-4**, in which both S_N1 and S_N2 oligomerization mechanisms yield positive free energies of reaction (relative to VC-3 as reference) when reacting with EC. This result implies that VC may act as a terminator for oligomerization if further reactions are unfavorable. In contrast to VC-3, FEC-3 is only metastable and the fluorine atom can be easily abstracted by a lithium ion to form an aldehyde. This aldehyde is susceptible to further reactions with nucleophiles and is discussed later in the chapter.

While the ethoxide S_N1 mechanisms consistently exhibit negative free energies, the radical S_N1 mechanisms (**Figure 2.4b**) are higher in energy. The reaction mechanism is analogous to the one in **Figure 2.4a**, but with a concerted loss of CO_2 as the nucleophilic oxygen attacks the C_C, which does exhibit a transition state. The first reaction has a large free energy barrier of approximately 30 kcal/mol. In this step, the linker O_E oxygen in the radical attacks the C_C in the neutral molecule, thereby shedding a CO_2 molecule from the o-EC radical. The FEC and VC radical pathways slightly diminish the reaction free energy barrier (FEC-5 and VC-5) and have lower free energies for the adducts FEC-6 and VC-6 when compared to EC-6. The last step in the mechanism, a ring-opening reaction, yields products that are overall net decreases in free energy

for the FEC and VC pathways, whereas the EC pathway ends with a net increase in free energy. However, as before, the VC species are not expected to react any further.

The energetic landscape seen in **Figure 2.4** suggests that nucleophilic alkoxides and radicals will preferentially attack FEC and VC over another EC. Particularly in the case of the radical S_N1 mechanism, the presence of an FEC or VC will shift the chemical equilibrium towards products (VC-7 and FEC-7) due to their negative free energies of reaction, as opposed to the unfavorable radical EC S_N1 pathway. These additive products are even further favored due to faster kinetics that result from a diminished energy barrier when compared to EC. Further, the reverse reactions for the FEC and VC pathways have increased free energy barriers relative to EC pathways, which reinforces the claim that FEC and VC preferentially react in the kinetically controlled SEI growth process.

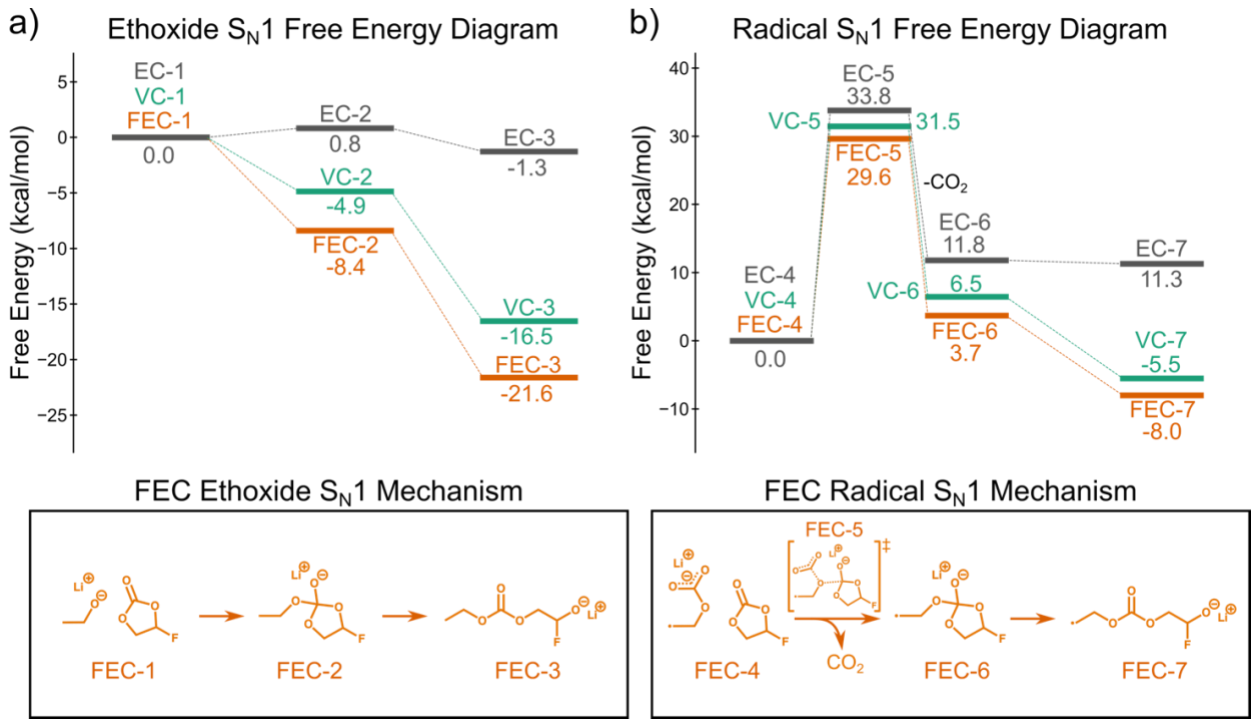

Figure 2.4: Free energy diagrams and mechanisms for a single step of S_N1 oligomerization in which an ethoxide (a) or radical o-EC (b) acts as the nucleophile. The gray pathway denotes that EC is being attacked, green is VC, and orange is FEC. Mechanisms shown below each diagram only depict the FEC case. Analogous mechanisms are seen for EC and VC systems and can be found in **Figure B-3**. Radical locations are denoted with a dot (•) in the radical mechanism in (b). EC-5, FEC-5, and VC-5 correspond to the transition states in the first reactive step.

2.4.3 S_N2 Oligomerization Mechanism

The S_N2 oligomerization mechanism was also investigated because it produces PEO chains, which have been detected in the SEI,[39,49] and can occur with the same reactants. In this mechanism, following a reconfiguration of the fully relaxed structure (not depicted), the nucleophilic oxygen attacks a C_E atom and breaks the opposite C_E-O_E bond in a concerted motion, as shown in **Figure 2.1b**. The second and final step regenerates the nucleophilic oxygen through a decarboxylation reaction with no transition state. This mechanism was only studied for EC and FEC (**Figure 2.5**) and not VC because there are no aliphatic C_E carbons available for nucleophilic attack in VC. The free energy diagram and mechanisms are shown in **Figure 2.5**. As before, the EC mechanisms can be found in **Figure B-5**.

The initial free energy barrier for ethoxide attacking a C_E carbon on EC was calculated to be 16.8 kcal/mol followed by a large, net drop in free energy to -24.9 kcal/mol. The large drop in energy is consistent with what was seen in Ref. 50, but the initial energy barrier is approximately half of what was previously reported. This discrepancy is due to the different solvent models used (CPCM in this study, SMD in Ref. 50). The SMD implicit solvent model consistently reports lower energies for the initial structures of each mechanism and thus increases all other energies relative to the starting point. The last step of the mechanism in which the nucleophilic oxygen is regenerated via decarboxylation was calculated to be entirely uphill in free energy, but still exhibits an overall drop in free energy to -15.6 kcal/mol relative to EC-8.

Compared to the EC pathway, the initial free energy barrier (FEC-9) and first adduct (FEC-10) for FEC were calculated to be lower by approximately 4 kcal/mol. However, instead of the decarboxylation step imparting an increase in free energy, FEC-11 exhibited an even further drop in free energy to -35.3 kcal/mol. This final structure is approximately 20 kcal/mol more stable than EC-11 and the barrier and adduct are also lower in free energy, implying a greater propensity for an ethoxide to attack an FEC molecule over another EC. As before with FEC, the bonded fluorine is only metastable and is readily abstracted by neighboring Li^+ or H^+ forming a reactive aldehyde. Due to the chiral center of FEC, there are multiple pathways to produce isomers for the species in **Figure 2.4** and **Figure 2.5**, but we have only reported the lowest energy pathway.

The radical S_N2 free energy diagram in **Figure 2.5b** exhibits a similar pattern as with **Figure 2.5a**, but with a different energy scale on the y-axis. The final free energy for the ethoxide (EC-11, -15.6 kcal/mol) and radical (EC-15, -4.6 kcal/mol) mechanisms are net negative, which

imply that both mechanisms are favored with chemical equilibria shifted towards these oligomer products. In the case of EC-11, this matches the finding that PEO-like oligomers are detected in SEI. Interestingly, after the first radical oligomerization step, the EC-15 carries a terminal oxide that can now act as the nucleophile in the mechanism and can proceed through lower energy barrier propagation reactions, similar to the barrier shown in **Figure 2.5a**. This suggests that the radical S_N2 reaction with an intact EC is possible and may also contribute to the concentration of PEO-like oligomers detected experimentally in the SEI.

Both FEC-11 and FEC-15 become more stable after decarboxylation, implying that the equilibrium is shifted towards the products of nucleophilic attack of FEC molecules. The S_N2 FEC pathways are also kinetically favored due to their diminished energy barriers for the forward reactions and increased energy barrier for the reverse reactions.

As with the S_N1 oligomerization mechanisms, the final products from the FEC pathways in **Figure 2.5** can easily have their fluorine atoms abstracted, leading to the formation of an aldehyde. This aldehyde formation from FEC species can further lead to acetal carbon formation, an interesting aspect that is discussed next.

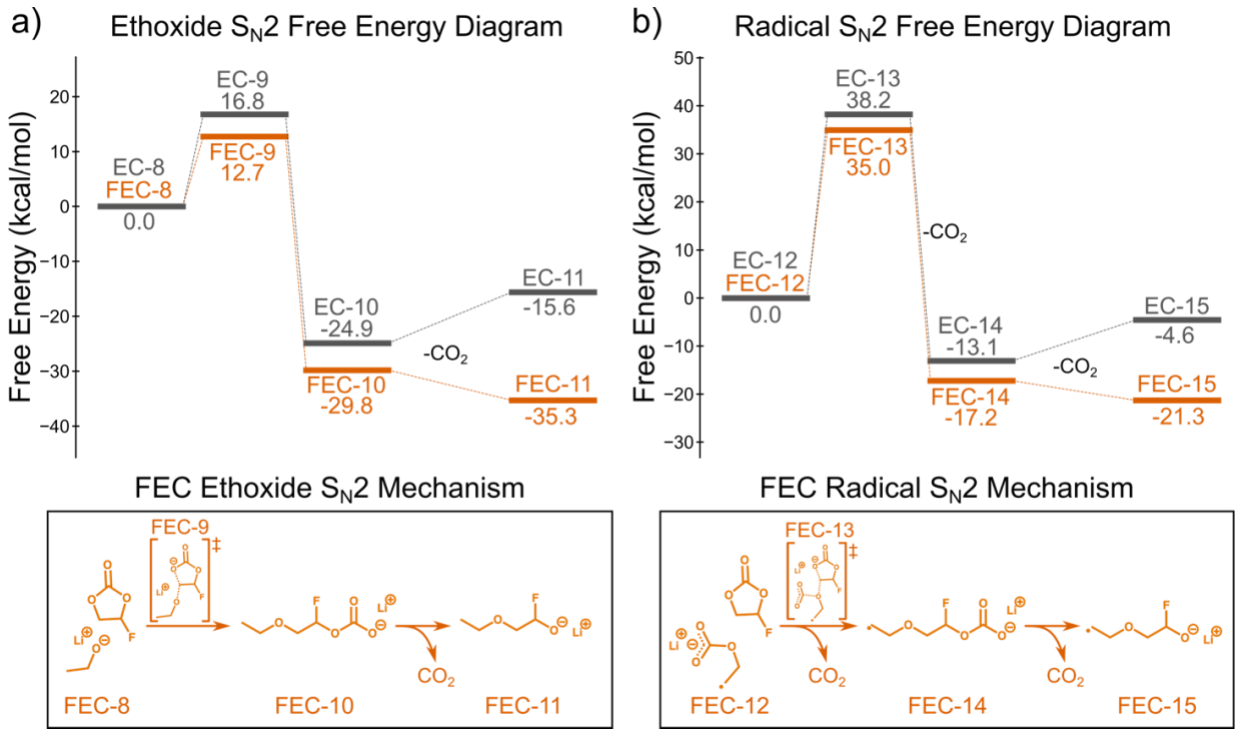

Figure 2.5: Free energy diagrams and mechanisms for a single step of S_N2 oligomerization in which an ethoxide (a) or radical o-EC (b) acts as the nucleophile. The gray pathway denotes that EC is the electrophile in the mechanism and orange is FEC. Mechanisms shown below each diagram only depict the FEC case. Analogous mechanisms are seen for the EC system and can be found in **Figure B-5**. Radical locations are denoted with a dot (•) in the radical mechanism in (b). EC-9, FEC-9, EC-13, and FEC-13 correspond to the transition states in the first reactive step.

2.4.4 Acetal Carbon Formation

Acetal carbons act as crosslinkers in the oligomeric SEI and can potentially account for the marked improvement in performance for batteries containing FEC in the electrolyte, especially in battery chemistries that suffer from large volume changes during cycling.[17,39,45,48,49]

As mentioned previously, the final products in each FEC mechanism can have the fluorine atom abstracted by a lithium ion to form an aldehyde in a barrierless, single step process, shown in **Figure 2.6**. This reaction produces LiF and a neutral aldehyde, denoted by an asterisk (*) following the name of the parent molecule from which it reacted.

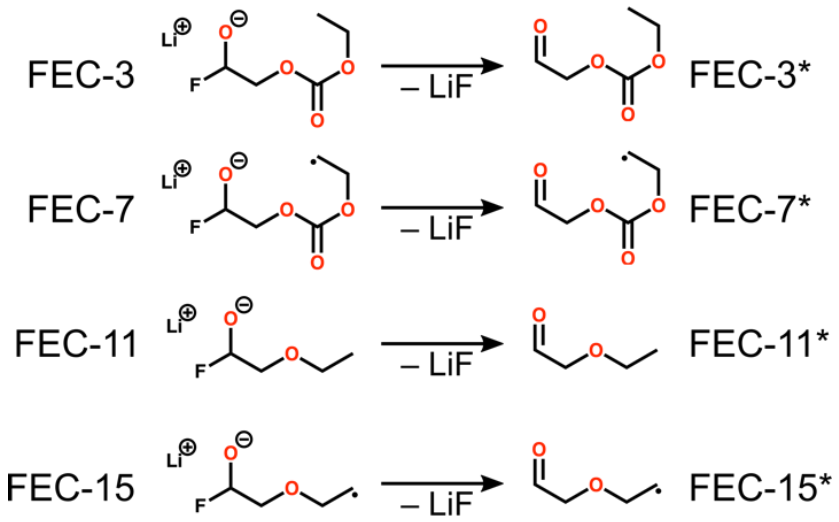

Figure 2.6: Mechanism for aldehyde formation for each of the terminal species in the FEC pathways. The species names along the right are simply the original molecule's name followed by an asterisk (*) to denote the aldehyde form.

This aldehyde group is highly reactive with nucleophiles. With the aldehydes as the starting points (FEC-3*, FEC-7*, FEC-11*, FEC-15*), we have calculated the free energy and enthalpy of reaction for acetal carbon formation via nucleophilic attack with an ethoxide, which can be seen in **Figure 2.7**. The general reaction scheme is seen in the upper right corner of **Figure 2.7**, with the green X representing the different moieties from each of the four mechanisms. Each reaction was found to be barrierless and thus no transition state is reported. Each moiety is labeled with the corresponding reaction energies on the bar plot.

While the enthalpy of reaction for each of the reactions was negative, all free energies of reaction were positive. The free energies of reaction were approximately +17 kcal/mol more than the enthalpy of reaction across the board, implying that the entropic losses for this type of reaction are large at 300 K.

As a result, the S_N1-derived species are not expected to undergo this acetal formation reaction due to the largely positive free energies of reaction, whereas the S_N2-derived species are far more likely with free energies of reaction very close to zero. Further, the S_N2-derived species have negative enthalpies of reaction, which implies that a stable product will be formed if the reaction does occur.

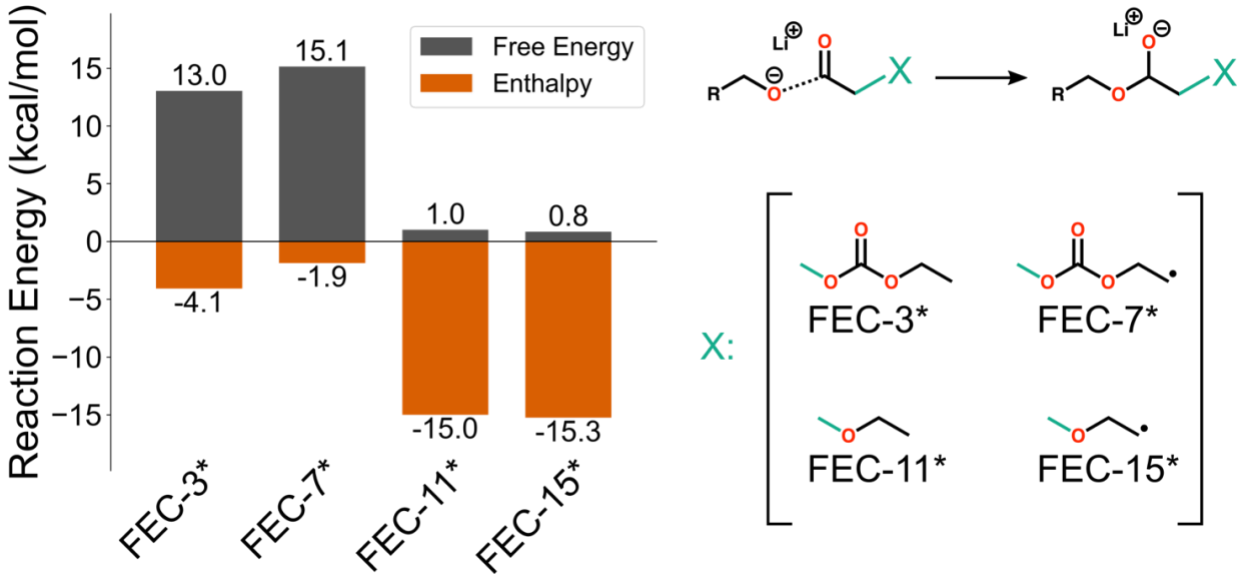

Figure 2.7: Reaction energies (enthalpy and free energy) for the nucleophilic attack of an aldehyde by an alkoxide, shown in the upper-right, where X corresponds to each of the four labeled groups. The green bond in each of the groups can be considered the same bond in the shown reaction. The labels on the groups correspond to the reaction energies in the left plot. Radical locations are denoted with a dot (•) in FEC-7* and FEC-15*.

2.5 Conclusions

In this study, we have examined how electrolyte additives FEC and VC impact the energetics of oligomerization reactions and compared to the case of EC oligomerization. We analyzed S_N1 and S_N2 oligomerization mechanisms in which two possible nucleophiles attack either an EC, FEC, or VC. The two nucleophiles studied were an ethoxide anion (for which we proposed a formation mechanism) and the o-EC radical anion. We find in all cases that FEC and VC mechanisms exhibit lower energy barriers and more stable adducts as compared to the analogous EC mechanisms. Moreover, we have shown the feasibility of these mechanisms with the o-EC radical anion acting as the nucleophile, in which CO_2 formation is seen in the first step of each mechanism, a product that is seen in experiment. Despite the large body of work that has studied these electrolyte additives, the mechanisms by which they improve battery performance are still not well understood. This study elucidates some of the potential roles of FEC and VC as electrolyte additives.

Matching previous studies,[15,39,49,50] we predict EC oligomerization via both the S_N1 and S_N2 mechanisms with the former being kinetically favorable and the latter being

thermodynamically favorable. Given our results, we conclude that the presence of electrolyte additives works to modulate this oligomerization process by either introducing branching points (FEC) or termination points (VC). The branching points generated by FEC are formed via S_N2 reaction of an FEC additive with a nucleophile to ultimately form an aldehyde terminal group and LiF salt. This aldehyde group can behave as an electrophile that is susceptible to reaction with another nucleophile (e.g., another oligomer). In this process, an acetal carbon is formed, which allows for further oligomerization via the newly formed oxide group. These branching points generated from FEC provide sites for cross-linking in the oligomeric SEI, which would reduce oligomer solubility in the liquid electrolyte. VC, on the other hand, can only undergo S_N1 reactions, which form a resonance stabilized oxide group that slows further oligomerization, thereby rendering reactions with VC an effective termination step.

Furthermore, the proposed roles of these additives during oligomerization do not necessitate high concentrations of either FEC or VC and may explain why small quantities of either additive provide improved SEI characteristics. Lastly, the proposed radical pathways also only require 1*e* reduction and, depending on the availability of reducing electrons and distance from the anode, a second reduction reaction may be significantly slower and thus would favor the proposed mechanisms.

3 Probing the Thermodynamics and Kinetics of Ethylene Carbonate Reduction at the Electrode-Electrolyte Interface with Molecular Simulations[2]

3.1 Abstract

Understanding the formation of the solid-electrolyte interphase (SEI) in lithium-ion batteries (LIBs) is an ongoing area of research due to its high degree of complexity and the difficulties encountered by experimental studies. Herein, we investigate the initial stage of SEI growth, the reduction reaction of ethylene carbonate (EC), from both a thermodynamic and kinetic approach with theory and molecular simulation. We employed both the potential distribution theorem (PDT) and the SMD implicit solvent model to EC solvation for the estimation of reduction potentials of Li^+, EC, and Li^+-solvating EC (s-EC), as well as reduction rate constants of EC and s-EC. We find that solvation effects greatly influence these quantities of interest, particularly the Li^+/Li reference electrode potential in EC solvent. Further, we also compute the inner- and outer-sphere reorganization energies for both EC and s-EC at the interface of liquid EC and a hydroxyl-terminated graphite surface, where total reorganization energies are predicted to be 76.6 and 88.9 kcal/mol, respectively. With the computed reorganization energies, we estimate reduction rate constants across a range of overpotentials and show that EC has a larger electron transfer rate constant than s-EC at equilibrium, despite s-EC being more thermodynamically favorable. Overall, this chapter demonstrates how ion solvation effects largely govern the prediction of reduction potentials and electron transfer rate constants at the electrode-electrolyte interface.

3.2 Introduction

Lithium-ion batteries (LIBs) play an integral role in today's technologies due to its high energy and power densities, making it an optimal choice for a large variety of applications, ranging from small, handheld device up to electric vehicles and even grid-scale storage. However, despite the wide array of use-cases for LIBs, they are not without their drawbacks. Among other downsides, LIBs suffer from capacity fade, or gradual loss of total storage capacity over time, due to many factors: pulverization of electrodes, separation from current collectors, dissolution of

[2] Reproduced from L.D. Gibson, J. Pfaendtner, and C.J. Mundy. Probing the thermodynamics and kinetics of ethylene carbonate reduction at the electrode-electrolyte interface with molecular simulations. The Journal of Chemical Physics, 155, 204703 (2021),[153] with the permission of AIP Publishing.

active material, formation of the solid-electrolyte interphase, etc. Among these many modes of capacity fade, it is seen that the formation of this solid-electrolyte interphase (SEI) layer is a leading contributor.[38] Thus, it is important to understand the mechanisms by which this degradation process occurs such that it can be controlled.

While the formation of this SEI layer can result in capacity fade, it is also important to understand that the SEI protects the anode from solvent intercalation. Without it, the graphitic anode would delaminate, giving way to rapid failure of the battery.[58] Further, the SEI can form a passivating layer, thereby preventing its continual growth. However, controlling the chemistry behind this growth process is difficult because the governing chemistry is not well understood. Thus far, it is known that the SEI growth process is driven by the reductive decomposition of the battery's electrolyte. There are many studies in literature that explore the possible reaction mechanisms that follow from electrolyte reduction,[10,17,46,90–94] but there are limited studies of formulating this process from the vantage point of electron transfer rate theory in the condensed phase.[95–97] Notably, Kim, et al. approached a similar problem, but focused on Li^+ reduction at a platinum electrode interface with a solid polymer electrolyte.[97] The method they employed allowed for the evaluation of reorganization energies as a function of applied electrode potential and found that there was a negligible change in reorganization energy as potential was increased.

The complexities of electron transfer in the vicinity of interfaces (charged or uncharged) in which the interface can act as either a donor or acceptor is an active area of research.[46,95,98–101] Viewing interfacial processes through the lens of Marcus theory provides a potentially powerful theoretical framework to isolate the important role of local solvent fluctuations as a descriptor for a quantitative understanding of the solvent reduction. One aspect of this work is focused on generating a methodology for computing the rate of electron transfer (ET) for electrolyte reduction at a graphitic anode interface (shown in **Figure 3.1a**) within the formalism of Marcus.[102–105] We focus our attention on two electron acceptors: EC (in pure EC solution) and s-EC (EC in the solvation shell of a Li^+, **Figure 3.1b**).

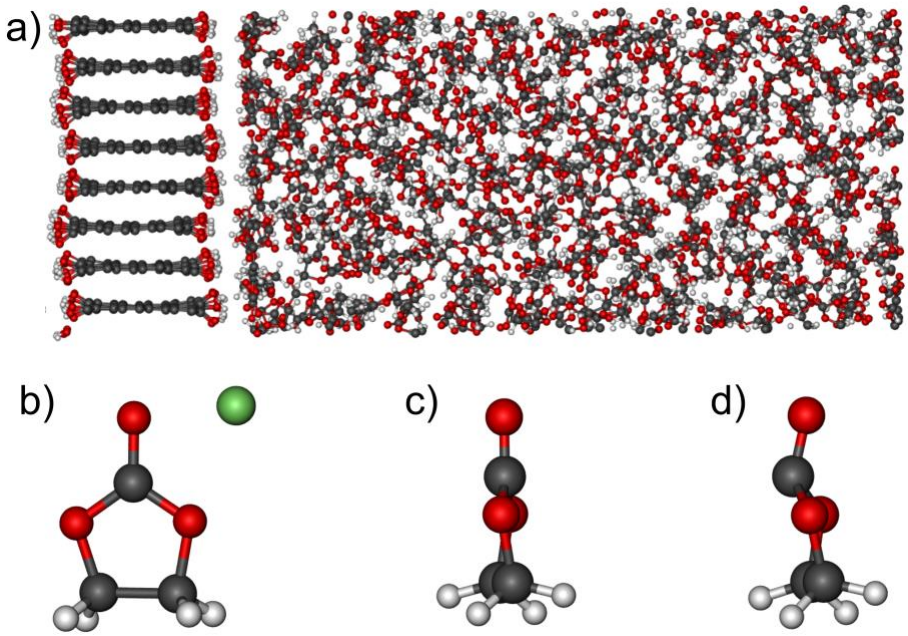

Figure 3.1: a) Snapshot of the hydroxyl-terminated graphite surface in contact with liquid EC. b) Molecular structure of EC and Li^+. Side views of the relaxed geometries of c) EC and d) EC^-, highlighting inner-sphere reorganization. Carbon, oxygen, hydrogen, and lithium are denoted by gray, red, white, and green atoms, respectively.

Briefly, Marcus theory describes rate of ET through interactions with solvent degrees of freedom in Marcus's equation,

$$k_{et} = \frac{2\pi}{\hbar}\frac{|V_{AB}|^2}{\sqrt{4\pi\lambda/\beta}}\exp(-\beta\Delta A^{\ddagger}) \qquad 3.1$$

where V_{AB} is the electronic coupling strength, λ is the reorganization energy, $\beta = 1/k_{\mathrm{B}}T$, and $\Delta A^{\ddagger}$ is defined as

$$\Delta A^{\ddagger} = \frac{(\Delta A_{rxn} + \lambda)^2}{4\lambda} \qquad 3.2$$

where ΔA_{rxn} is the free energy of reaction. Given that most interfacial reduction reactions at an electrode surface likely occur within the adiabatic regime of ET,[106] we do not compute electronic coupling values.

The free energy of reaction is directly related to the reduction potential, which is a key quantity that describes electrochemical stability of electrolytes.

$$\Delta A^{\circ}_{\mathrm{rxn}} = -nF\Phi^{\circ}_{\mathrm{abs}} \qquad 3.3$$

where $\Delta A^{\circ}_{\mathrm{rxn}}$ is the standard free energy of reaction, n is the number of electrons being transferred, F is Faraday's constant, and $\Phi^{\circ}_{\mathrm{abs}}$ is the standard reduction potential in the absolute scale (note: in this chapter the subscript of reduction potentials denotes the reference and subsequent parentheses contain the redox couple of interest). The inverse relationship in Eq. (3.3) implies that higher Φ° values correspond to a greater propensity for reduction. It is often valuable to report reduction potentials relative to a standard reference (Li^+/Li in our case) rather than the absolute scale given the difficulty of measuring absolute free energies experimentally. This is often achieved by using the standard hydrogen electrode (SHE) potential of 4.42 V in the absolute scale along with the Li^+/Li reference potential of −3.05 V vs. SHE,[10,61,107,108]

$$\begin{aligned}\Phi^{\circ}_{\mathrm{Li^+/Li}} &= \Phi^{\circ}_{\mathrm{abs}} - \Phi^{\circ}_{\mathrm{abs}}(\mathrm{SHE}) - \Phi^{\circ}_{\mathrm{SHE}}(\mathrm{Li^+/Li}) \\ &= \Phi^{\circ}_{\mathrm{abs}} - 4.42 + 3.05 \\ &= \Phi^{\circ}_{\mathrm{abs}} - 1.37 \approx \Phi^{\circ}_{\mathrm{abs}} - 1.4\end{aligned} \qquad 3.4$$

This conversion by subtracting 1.4 V is commonly used when computing reduction potentials for LIB electrolyte species such as EC, dimethyl carbonate (DMC), vinylene carbonate (VC), and fluoroethylene carbonate (FEC).[61,107,108] However, we discuss later in the chapter the limitations of the conversions used in Eq. (3.4) for the estimation of reduction potentials.

In both thermodynamic and kinetic descriptions of EC reduction, the solvation free energy plays an important role that must be carefully addressed for the accurate prediction of reduction potentials and ET rate constants. The chemical potential of a species X in a solvent is represented by,

$$\mu_X = \mu_X^* + \frac{1}{\beta}\ln(\gamma_X \rho_X \Lambda_X^3) \qquad 3.5$$

where μ_X^* is the single-ion solvation free energy at a fixed point, Λ_X is the deBroglie wavelength, γ_X is the activity coefficient, and ρ_X is the concentration of X. The first term in Eq. (3.5) describes the local interactions of solute X with a solvent, whereas the second term provides a statistical definition of the standard states used in this study.[109]

The single-ion solvation free energy is computed in a classical potential by

$$\mu_X^* = \frac{1}{\beta}\ln\langle\exp(-\beta U_{\mathrm{XS}})\rangle_0 - E_X^{\mathrm{Vac}} \qquad 3.6$$

where U_{XS} is the solute-solvent interaction energy and is defined as $U_{\mathrm{XS}} = U_{\mathrm{XS,Ns}} - U_{\mathrm{Ns}}$, which is the energy difference for a given solvent structure with and without the ion. E_X^{Vac} is the energy of X in vacuum and $\langle \cdots \rangle_0$ denotes that averaging is done in the ensemble with no solute-solvent interactions. Eq. (3.6) can be simplified into the following form using the potential distribution theorem (PDT),[110–112]

$$\mu_X^* = \mu_{\mathrm{Cav}}^* + \mu_{\mathrm{PC}}^* - E_X^{\mathrm{Vac}} \tag{3.7}$$

where μ_{Cav}^* is the free energy required to form a cavity with a radius matching species X and μ_{PC}^* is the charging free energy that describes the solvent's response to the creation of a solute's charge. Eq. (3.7) would also include contributions from the surface potential, but in this work those contributions were computed to be negligible. A more in-depth derivation of μ_X^* can be found in Refs. [111] and [112]. In implicit solvent (SMD[113]), the solvation free energy can be approximated directly by taking the difference in energy between each state with and without a solvent model,

$$\mu_X^* \approx E_X^{\mathrm{SMD}} - E_X^{\mathrm{Vac}} \tag{3.8}$$

The charging free energy can be computed by incrementally adding small amounts of charge to the ion,[111,112]

$$\mu_{\mathrm{PC}}^* = \sum_{i=0}^{M-1} -\frac{1}{\beta} \ln \left\langle \exp\left[-\beta\left(U_{(i+1)\delta q} - U_{i\delta q}\right)\right] \right\rangle_{U_{i\delta q}} \tag{3.9}$$

where M is the total number of windows for charging, $U_{i\delta q}$ and $U_{(i+1)\delta q}$ are the average potential energies of the system in windows i and $i + 1$, respectively, and δq is the incremental charge step size ($\delta q = q/M$). To ensure that the step size is small enough, μ_{PC}^* μ_{PC^*} can be computed in reverse via

$$\mu_{\mathrm{PC}}^* = \sum_{i=1}^{M} \frac{1}{\beta} \ln \left\langle \exp\left[\beta\left(U_{(i+1)\delta q} - U_{i\delta q}\right)\right] \right\rangle_{U_{i\delta q}} \tag{3.10}$$

and should match the profile generated by Eq. (3.9).

The focus of our work is on identifying the impact of solvation on the thermodynamics and kinetics of ethylene carbonate reduction in the condensed phase by computing reduction potentials for Li^+, EC, and s-EC and ET rate constants for EC and s-EC. Multiple early works have studied

ET at an interface[106,114–116] and provide a good foundation for our study. We closely followed the work of Rose and Benjamin,[114] but with an increased complexity of the systems studied. In this chapter, we use the potential distribution theorem (PDT) to evaluate solvation for condensed phase calculations of reduction potentials and compared to both an implicit solvent model (SMD) and literature values. We also compute reorganization energies for EC and s-EC reduction at a simple electrode interface for the prediction of ET rate constants across a range of overpotentials.

3.3 Methods

Two main quantities are computed in this work for Li^+, EC, and s-EC: reduction potentials and electron transfer (ET) rate constants. For the calculation of reduction potentials, several steps are involved (shown in **Figure 3.2**), including the calculation of solvation free energies and free energies of reaction. The free energies of reaction are extracted from thermodynamic cycles (**Figure 3.3**) which are converted to reduction potentials via Eq. (3.3). The key quantity of focus in this work is the solvation free energy which largely affects the free energy of reaction and consequently the reduction potential. The ET rate constant calculations are governed by reorganization energies, which are discussed in Section 3.3.4.

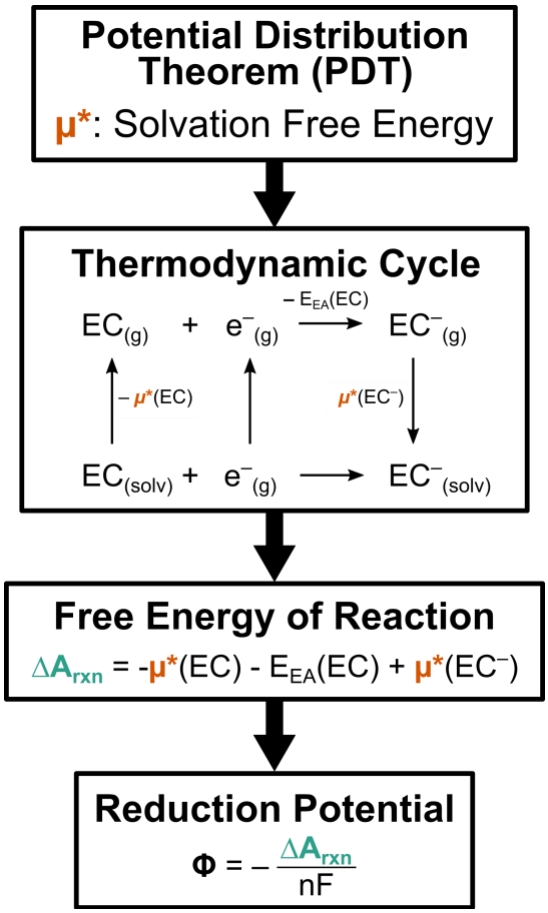

Figure 3.2: Workflow for computing EC reduction potentials from solvation free energies. The same general workflow is also applied when computing Li^+ and s-EC reduction potentials. This highlights the connection between solvation free energies and predicted reduction potentials.

3.3.1 Classical Molecular Dynamics (MD)

All classical simulations were run using GROMACS[117] in the NVT ensemble at 300 K and a step size of 0.5 fs. The Nosé-Hoover thermostat[66,67] was used to maintain the system's temperature and the all-atom optimized potentials for liquid simulations (OPLS-AA) forcefield[118–120] was used to describe all interatomic interactions. The OPLS-AA forcefield has been used previously to accurately compute transfer free energies for similar systems.[121] All restraints (unless otherwise specified) were applied via the PLUMED library.[75]

3.3.2 Potential Distribution Theorem (PDT)

Solvation free energies are computed from condensed phase classical MD simulations using the potential distribution theorem (PDT),[110–112] which breaks the solvation free energy into

multiple contributions that can be computed separately, shown in Eq. (3.7). Charging free energy simulations were done in a 3 nm cubic box for the Li and EC systems solvated in bulk EC with no interface following Eq. (3.9) in increments of 0.1 |*e*|. Simulations of cavity formation were performed in the same conditions as charging, but instead of adjusting charge, the σ Lennard-Jones parameter of a neutral Li atom was incremented from 0 to 2.2 Å in 50 steps of 0.044 Å.

3.3.3 Reduction Potentials

DFT calculations for reduction potentials were performed with Gaussian 16 rev. a03.[82] The B3PW91 hybrid funcitonal[29] was used with the 6-311++G(d,p) basis set[122,123] for the calculation of reduction potentials, electron affinities, and ionization potentials. When an implicit solvent was utilized, the SMD method[113] was employed with ϵ = 89.78 to match that of liquid EC.[86] Free energies computed with DFT were obtained via frequency calculations, which compute entropic contributions and zero-point energy corrections to enthalpy at a reference state (1 atm and 298.15 K) using the rigid rotor harmonic oscillator (RRHO) approximation.

Binding energies were computed via umbrella sampling[33] in the same simulation environment as charging using classical MD. The binding energies in **Figure 3.3c** are derived from the following equation,

$$\Delta A_{\mathrm{b}}^{\circ} = -k_{\mathrm{B}}T \ln(K_{\mathrm{b}}) \tag{3.11}$$

where K_{b} is the equilibrium binding constant. K_{b} is computed from a potential of mean force (PMF), $w(r)$, via r^2-weighted integration

$$\mathrm{K_b} = \int_{\mathrm{site}} 4\pi C^{\circ} r^2 \mathrm{d}r \exp\{-\beta[w(r) - w(r^*)]\} \tag{3.12}$$

where r^* denotes a radial distance within the bulk region and C° is the standard concentration (1 mol/L). We have defined the binding site region to begin at r = 0 and end at the first peak in the PMF.[124]

3.3.4 Reorganization Energies

Reorganization energies for EC and s-EC are computed with respect to their reduced, cyclic structure (i.e., not the ring-opened structure). Although this ring-opened structure of EC^- is lower in energy than the cyclic structure, there still exists an energy barrier separating these two states.[12] Therefore, we have chosen to compute reorganization energies with respect to the cyclic structure of EC^-.

Inner-sphere reorganization energies were calculated by first optimizing EC and EC^- structures with $q = 0$ and -1 $|e|$ net charges, respectively, with static DFT in CP2K.[70] The Perdew-Burke-Ernzerhof exchange-correlation functional[27] was employed with double zeta basis sets and GTH pseudopotentials[125–128] along with a 400 Ry cutoff. Singlet and doublet multiplicities were used for the neutral and reduced states, respectively. Optimized structures for EC and EC^- were then used to evaluate their energies with swapped charges ($q = -1$ and 0 $|e|$, respectively). The energy difference between the bent and flat configurations for each charge state was calculated and averaged to yield the inner-sphere reorganization energy in **Table 3.3**. Alternatively, we evaluated the inner-sphere reorganization energy using ab initio molecular dynamics (AIMD) simulations of liquid EC in CP2K. AIMD simulations were run with a 0.5 fs time step and at the same level of theory as the inner-sphere reorganization energy calculations. EC^- structures were sampled in liquid EC and then substituted into a separate AIMD simulation of pure liquid EC (no net charge) by choosing a single EC molecule and aligning their structures by minimizing the root-mean-square deviation (RMSD). The trajectory with the substituted structure was resampled (still with 0 net charge) and the resulting energy difference was averaged to give the AIMD value in **Table 3.3**. Marcus parabolas were constructed with a hydroxyl-terminated graphite surface contacting liquid EC and box size of 7.10 x 2.93 x 2.60 nm in GROMACS. EC and s-EC were held at the EEI using a harmonic restraint. Regions beyond the free energy minima were sampled by directly adjusting the oxidant's charge which was then reweighted back to the two charge states (oxidized and reduced) in a manner similar to umbrella sampling (also discussed in Ref. 114), allowing us to reconstruct the full parabolas for high energy regions. Partial charges for the reduced state of EC were estimated via a restrained electrostatic potential (RESP) calculation in CP2K with the same level of theory used for inner-sphere reorganization energy calculations.

The reaction coordinate used in the Marcus parabolas was the electrostatic potential on the geometric center of the ion,[114,129,130]

$$U(\vec{\boldsymbol{R}}) = \sum_i \frac{k_e q_i}{|\vec{\boldsymbol{R}}_i|} \qquad 3.13$$

Where $\vec{\boldsymbol{R}}$ denotes the configuration of all atoms in the system, k_e is Coulomb's constant, q_i is the charge on solvent atom *i*, and $|\vec{\boldsymbol{R}}_i|$ is the distance between atom *i* and the geometric center of the EC.

The order parameter in Eq. (3.13) is not easily restrained for umbrella sampling windows. Instead, we used the molecular net charge as an effective restraint along the order parameter. In this way, we can simply take the static bias potential as

$$V_{\text{bias}}^{(m)}\left(U(\vec{\boldsymbol{R}},t)\right) = U_{\delta q}^{(m)}(\vec{\boldsymbol{R}},t) - U_{q=0,-1}(\vec{\boldsymbol{R}},t), \qquad 3.14$$

where δq is the change in net charge of EC, $U_{\delta q}$ is the potential energy for the *m*th window with net charge δq, and $U_{q=0,-1}$ is the potential energy for the same molecular configurations but with $q = 0$ or -1 $|e|$. This allows us to reconstruct both Marcus parabolas for the reactant and product diabatic states from the same series of simulations, in which the net charge of an EC molecule is changed from 0 to −1 in 0.2 $|e|$ charge increments. The free energy, *A*, along the solvent coordinate for window *m* is then computed by

$$A^{(m)}(u) = -k_B T \ln \langle \delta\left[u - U(\vec{\boldsymbol{R}})\right] \beta V_{\text{bias}}^{(m)}\left(U(\vec{\boldsymbol{R}})\right)\rangle_{\delta q} \qquad 3.15$$

where $\delta[\cdots]$ is the Dirac delta function, u is the reaction coordinate along which the free energy profile is established, and $\langle\cdots\rangle_{\delta q}$ denotes averaging is done in the ensemble with δq partial charges on EC. This process produces a PMF for each window along the order parameter following the procedure of umbrella sampling.[33] Each PMF segment is manually aligned so they create a single, smooth PMF. This manual alignment was allowable because the shape of the full PMF was largely expected to follow a parabolic trend, which was ultimately observed. The PMFs are then fitted to symmetrical parabolas for the reactant and product states.

3.4 Results & Discussion

3.4.1 Solvation Free Energy

The free energy of reaction describes the driving force behind ET and can be approximated from the thermodynamic cycles depicted in **Figure 3.3**. The free energy of ET reactions can also be represented as the reduction potential, which describes the likelihood of a species to be reduced. In **Figure 3.3a** and **Figure 3.3b**, the oxidant is desolvated into the vacuum phase where the electron is added. Following reduction, the species is then deposited to the solid phase (**Figure 3.3a**) or solvated again (**Figure 3.3b**). However, in **Figure 3.3c**, the Li^+ and EC are coordinated and must be separated in the solvent phase first, after which the EC can follow the same cycle as **Figure 3.3b** before finally re-coordinating with a Li^+.

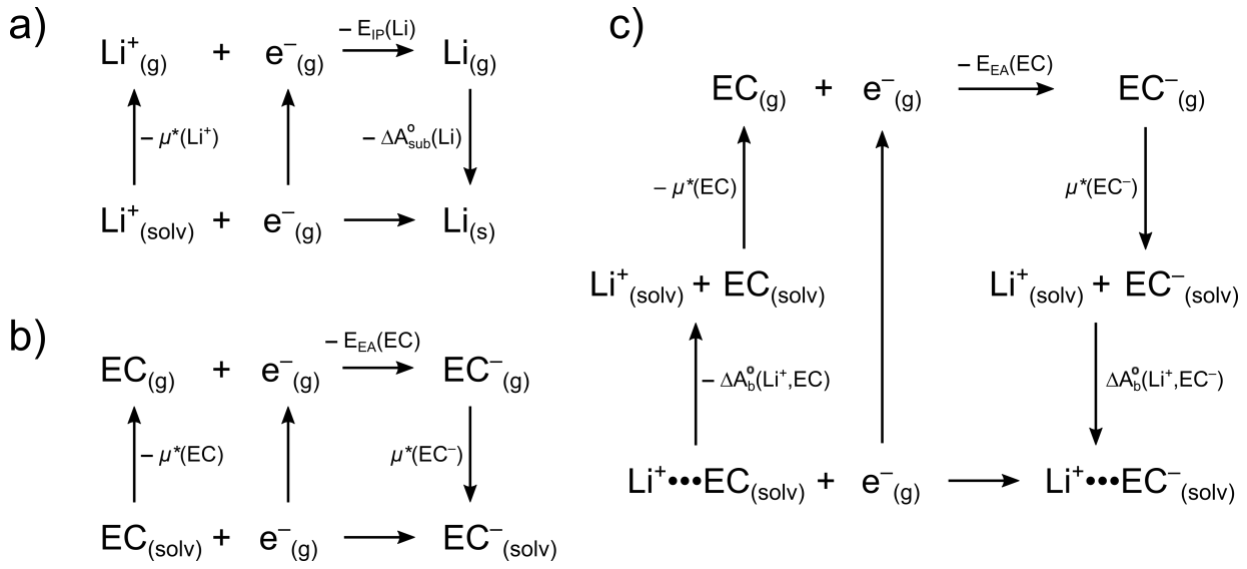

Figure 3.3: Thermodynamic cycles for a) $Li^+ + e^- \rightarrow Li$, b) $EC + e^- \rightarrow EC^-$, and c) $Li^+\cdots EC + e^- \rightarrow Li^+\cdots EC^-$ redox reactions. $\mu^*(X)$ denotes the single ion solvation free energy in EC and $\Delta A^\circ_{\mathrm{sub}}$ denotes the standard free energy of sublimation. E_{IP} and E_{EA} denote the ionization potential and electron affinity in vacuum, respectively. $X_{(\mathrm{solv})}$, $X_{(\mathrm{g})}$, $X_{(\mathrm{s})}$ denote solvated, gaseous, and solid phases, respectively, for species X. $\Delta A^\circ_{\mathrm{b}}(X,Y)$ denotes the standard binding energy between X and Y. The signs of thermodynamic quantities in the cycles arise from the transitions depicted by the arrows.

The key quantities in each of the thermodynamic cycles are the solvation free energies, which are represented as single-ion solvation free energies, μ^*_X. We posit that isolating this local[109] contribution to the chemical potential will provide a useful descriptor for important collective effects.

In the case of EC, the full single-ion solvation free energy was not required given that the difference in solvation energies between its reduced and neutral states was sufficient. The E_X^{Vac} term in Eq. (3.7) cannot be ignored for EC because it is a polyatomic ion with a non-zero vacuum energy, whereas it can be neglected in the case of lithium. The difference in solvation free energy is then

$$\begin{aligned}\Delta\mu^*_{\mathrm{EC}} &= \mu^*_{\mathrm{EC}^-} - \mu^*_{\mathrm{EC}} \\ &= \Delta\mu^*_{\mathrm{PC,EC}} - \Delta E^{\mathrm{Vac}}_{\mathrm{EC}}\end{aligned} \qquad 3.16$$

Since the thermodynamic pathway for EC^- solvation contains the EC solvation pathway, the cavity formation free energies are the same and cancel. $\mu^*_{PC,EC}$ denotes the charging from EC with partial charges in its neutral state to partial charges of EC^-.

We have computed the charging free energy profiles, μ^*_{PC}, for lithium and EC using Eq. (3.9), which are shown in **Figure 3.4a**. Lithium yields a large charging free energy at −106.7 kcal/mol whereas EC yields a much smaller charging free energy of −21.7 kcal/mol. In **Figure 3.4b** we compare the μ^* and $\Delta\mu^*$ values for Li^+ and EC, respectively, when computed with SMD (lighter shade) and PDT (darker shade). For Li^+, the single-ion solvation free energy was computed to be −89.3 and −104.8 kcal/mol for SMD and PDT, respectively. The PDT value was computed using Eq. (3.7) where μ^*_{Cav} was taken from **Figure 3.5** to be 1.9 kcal/mol. This free energy profile of cavity formation in liquid EC increases at a rate approximately twice as fast as that in water,[131] which is supported by the difference in their densities (1.32 g/cm^3 vs. 0.997 g/cm^3, respectively). The SMD value for μ^*_{Li+} was computed using Eq. (3.8) and reports a significantly lower value than PDT, which can be attributed to the limited applicability of the SMD model for ionic species with such small cavities.[107]

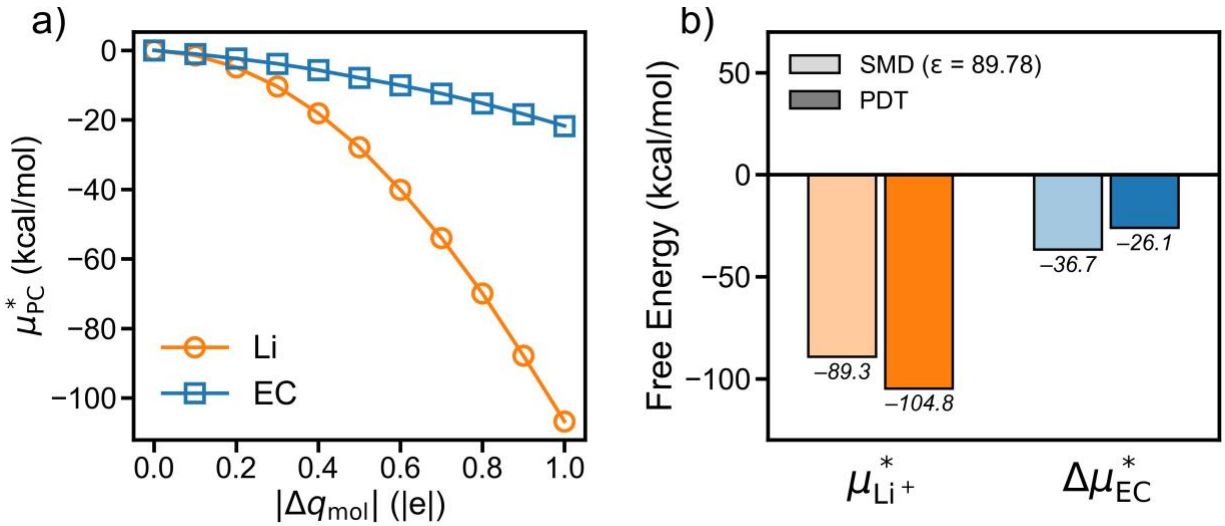

Figure 3.4: a) Charging free energy profiles of EC and Li. From left to right, the charge of EC transitions from 0 to -1, whereas Li transitions from 0 to +1. b) Comparison of charging free energies computed with SMD (lighter shades) and PDT (darker shades).

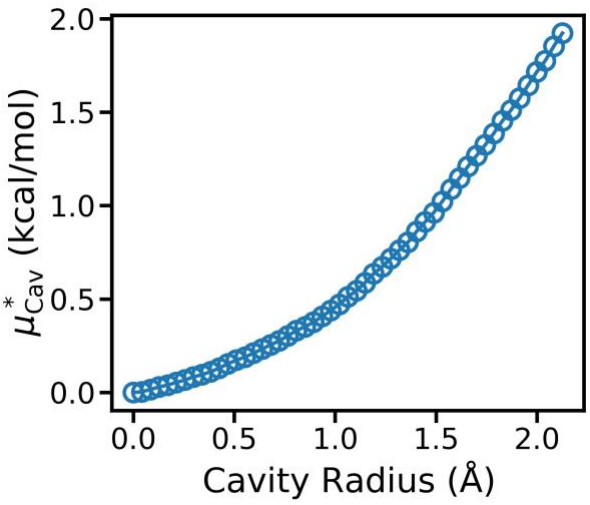

Figure 3.5: Free energy of cavity formation for a hard sphere in ethylene carbonate up to the radius of Li^+.

There is a 15.5 kcal/mol difference between the two solvation methods, but our computed value for the single-ion solvation free energy of lithium in EC is supported by quasi-chemical theory (QCT) calculations that also predict a +15 kcal/mol transfer free energy for Li^+ between EC and water, with water being the favored solvent.[121] Comparing our value to the free energy of solvation for Li^+ in water (−120 kcal/mol),[112] we see very close agreement in the transfer free energy from Ref. 121. Again, we note that these comparisons only apply to the single-ion solvation free energy and do not account for chemical activities in Eq. (3.5).

For EC, SMD predicts that $\Delta\mu^*_{EC}$ = −36.7 kcal/mol from Eq. (3.8), whereas PDT predicts a value of −26.1 kcal/mol. The ΔE^{Vac}_{EC} term of Eq. (3.16) was computed to be −4.4 kcal/mol. SMD predicts a more favorable solvation free energy for EC over PDT by approximately 10 kcal/mol.

It is important to note that these reduction reactions occur near the electrode interface, but the single-ion solvation free energies computed in this work are for the bulk phase. An attempt to adjust the free energy from the bulk phase to the interfacial region did not yield noticeable changes, which was due largely to non-polarizability of the surface used. An improved description of the interface with a polarizable surface would yield a better estimate of the interfacial solvation region. The charging of species directly at the interface would not be required since bulk phase solvation energies can be adjusted by the difference in interfacial binding energies. Recently, Angarita-Gomez and Balbuena have demonstrated the destabilization of the solvation shell of a Li^+ as it

approaches an anode interface, with changes in the solvation free energy of approximately 1 eV for a Li^+ in EC.[132] Their work further highlights the impact of interfacial effects on solvation energies.

3.4.2 Reduction Potentials

In **Table 3.1** and **Table 3.2**, we have used the single-ion solvation free energies in **Figure 3.4b** to compute reduction potentials for Li^+, EC, and s-EC. The values for $-E_{\mathrm{IP}}(\mathrm{Li})$ and $-E_{\mathrm{EA}}(\mathrm{EC})$ in **Figure 3.3** were computed to be −128.6 and 7.1 kcal/mol, respectively. The two binding energies in **Figure 3.3c**, $-\Delta A_{\mathrm{b}}^{\circ}(\mathrm{Li}^+,\mathrm{EC})$ and $-\Delta A_{\mathrm{b}}^{\circ}(\mathrm{Li}^+,\mathrm{EC}^-)$, were computed to be −0.5 and −5.7 kcal/mol, respectively. The handbook[133] value for Li sublimation, $\Delta A_{\mathrm{sub}}^{\circ}(\mathrm{Li})$, is 38.1 kcal/mol.

For comparison, we used both implicit (SMD) and explicit (PDT) solvent models to compute the charging free energy. For each respective calculation method, we first computed the Li^+/Li reduction potential in the absolute scale, $\Phi_{\mathrm{abs}}^{\circ}(\mathrm{Li}^+/\mathrm{Li})$, (reported in **Table 3.1** and **Table 3.2**), which were then used to convert the reduction potentials of EC and s-EC from the absolute scale to the Li^+/Li scale via

$$\Phi_{\mathrm{Li}^+/\mathrm{Li}}^{\circ} = -\frac{\Delta A_{\mathrm{rxn}}^{\circ}}{nF} - \Phi_{\mathrm{abs}}^{\circ}(\mathrm{Li}^+/\mathrm{Li}) \qquad 3.17$$

where $\Delta A_{\mathrm{rxn}}^{\circ}$ is the standard free energy of reaction, *n* is the number of electrons transferred, *F* is Faraday's constant.

Table 3.1: Reduction potentials for Li^+, EC, and s-EC with solvation free energies computed via PDT. Values in the first column are reported in Volts in the absolute scale, whereas all other columns are reported in Volts vs. Li^+/Li. The $\Phi_{\mathrm{Li}^+/\mathrm{Li}}^{\circ}$ column corresponds to the Li^+/Li scale as computed in this work, whereas the $\Phi_{\mathrm{Li}^+/\mathrm{Li}}^{\circ,(1.4\ \mathrm{V})}$ column represents reduction potentials in the Li^+/Li scale using the commonly applied relationship $\Phi_{\mathrm{Li}^+/\mathrm{Li}}^{\circ,(1.4\ \mathrm{V})} = \Phi_{\mathrm{abs}}^{\circ} - 1.4\ \mathrm{V}$. Columns with an additional 1.3 V represent the inclusion of the ring-opening reaction as discussed in the text. Although the last column closely matches the experimental value (0.8 V vs. Li^+/Li)[134], the origin of this lacks the self-consistency of using the Li^+/Li scale as computed in this work as discussed in the main text.

Species	$\Phi_{\mathrm{abs}}^{\circ}$	$\Phi_{\mathrm{Li}^+/\mathrm{Li}}^{\circ}$	$\Phi_{\mathrm{Li}^+/\mathrm{Li}}^{\circ} + 1.3\ \mathrm{V}$	$\Phi_{\mathrm{Li}^+/\mathrm{Li}}^{\circ,(1.4\ \mathrm{V})}$	$\Phi_{\mathrm{Li}^+/\mathrm{Li}}^{\circ,(1.4\ \mathrm{V})} + 1.3\ \mathrm{V}$
Li^+	2.60	0.00	–	–	–
EC	0.82	-1.78	-0.48	-0.58	0.72
s-EC	1.10	-1.50	-0.20	-0.30	1.00

Table 3.2: Reduction potentials for Li^+, EC, and s-EC with solvation free energies computed via SMD implicit solvent model. Values in the first column are reported in Volts in the absolute scale, whereas all other columns are reported in Volts vs. Li^+/Li. The $\Phi^\circ_{Li^+/Li}$ column corresponds to the Li^+/Li scale as computed in this work, whereas the $\Phi^{\circ,(1.4\ V)}_{Li^+/Li}$ column represents reduction potentials in the Li^+/Li scale using the commonly applied relationship $\Phi^{\circ,(1.4\ V)}_{Li^+/Li} = \Phi^\circ_{abs} - 1.4$ V. Columns with an additional 1.3 V represent the inclusion of the ring-opening reaction as discussed in the text.

Species	Φ°_{abs}	$\Phi^\circ_{Li^+/Li}$	$\Phi^\circ_{Li^+/Li} + 1.3$ V	$\Phi^{\circ,(1.4\ V)}_{Li^+/Li}$	$\Phi^{\circ,(1.4\ V)}_{Li^+/Li} + 1.3$ V
Li^+	3.35	0.00	–	–	–
EC	1.28	-2.07	-0.77	-0.12	1.18
s-EC	1.56	-1.79	-0.49	0.16	1.46

The reported value for $\Phi^\circ_{abs}(Li^+/Li)$ ranges from 1.3 to 1.79 V; with 1.4 V being commonly used as it aligns with the conversion described in Eq. (3.4).[108] However, this range of reported values do not correspond to Li^+ solvation in EC, but rather with water, DMSO, or acetonitrile. While the solvent is expected to only shift the reduction potential by a couple tenths of a Volt,[108] we computed $\Phi^\circ_{abs}(Li^+/Li)$ to be 3.35 and 2.60 V with SMD and PDT, respectively. In **Table 3.1** and **Table 3.2**, we have included additional columns that correspond to the commonly used 1.4 V value ($\Phi^{\circ,(1.4\ V)}_{Li^+/Li} = \Phi^\circ_{abs} - 1.4$ V) and/or the addition of 1.3 V, which corresponds to the inclusion of the ring-opening reaction of EC (discussed later in this section). The additional columns do not include values for Li^+ because the new conversions/modifications do not apply to Li^+ reduction. These columns are included to demonstrate how we can align with literature values when using similar conversion methods from the absolute scale. However, a major focus of this study is to compute reduction potentials self-consistently [i.e., using $\Phi^\circ_{abs}(Li^+/Li)$ computed in this work, along with Eq. (3.17)]. Importantly, the solvation free energy of Li^+ is seemingly the only quantity that affects $\Phi^\circ_{abs}(Li^+/Li)$ in **Figure 3.3a** when changing solvents. The value of 1.4 V that is often used[10,61,107,108] corresponds to a solvation free energy of approximately −130 kcal/mol for Li^+, which is even greater than the solvation free energy for water by 10 kcal/mol. However, Li^+ is expected to have a *less* favorable solvation free energy in EC vs. water by approximately 15 kcal/mol (−105 vs −120 kcal/mol, respectively).[121] The resulting 25 kcal/mol

difference in $\mu^{\circ}_{\mathrm{Li+}}$ between our computed value (−105 kcal/mol) and the purported −130 kcal/mol leads to a 1.08 V difference in $\Phi^{\circ}_{\mathrm{abs}}(\mathrm{Li}^{+}/\mathrm{Li})$ values.

Additionally, the common 1.4 V corresponds to aqueous systems and thus is expected to differ for non-aqueous systems such as EC. Busch, et al. presents an approach for computing the standard hydrogen electrode potential for aqueous and non-aqueous and reports a $\Phi^{\circ}_{\mathrm{abs}}(\mathrm{SHE})$ value of approximately 4.1 V in water and 4.9 V in polar, non-aqueous solvents (e.g., DMSO, acetonitrile, DMF).[135] This apparent 0.8 V difference demonstrates the disparity between aqueous and non-aqueous electrode potentials.

Comparing the reduction potentials for EC and s-EC when converted via 1.4 V ("$\Phi^{\circ,(1.4\ \mathrm{V})}_{\mathrm{Li}^{+}/\mathrm{Li}}$" columns in **Table 3.1** and **Table 3.2**) to those in literature[10,61], we see a difference of 0.5-0.8 V for the PDT-derived values and 0.1-0.2 V difference for the SMD-derived values. The deviation in with PDT-derived values is largely due to the difference in methods for computing solvation free energies. The close agreement with the SMD-derived values is unsurprising given that approaches in literature often employ implicit solvent models.[10,61] These $\Phi^{\circ,(1.4\ \mathrm{V})}_{\mathrm{Li}^{+}/\mathrm{Li}}$ reduction potentials are included to allow for the direct comparison with literature, but we maintain the importance of computing the reduction potentials self-consistently.

Compared to PDT, SMD reports a lower reduction potential for the Li^{+}/Li reference due to its less favorable solvation free energy, but predicts larger $\Phi^{\circ}_{\mathrm{abs}}$ values for EC and s-EC. The primary difference between EC and s-EC is the difference in binding energies for the s-EC cycle in **Figure 3.3c** and thus ion concentration would likely impact Φ°(s-EC) values through the binding energies computed with Eqs. (3.11) and (3.12).

An important aspect to consider is the overall reaction that is measured experimentally. Zhang, et al. previously measured the reduction potential of EC in THF to be 1.36 V vs. Li^{+}/Li, which matched closely with their computed value of 1.46 V vs. Li^{+}/Li.[136] However, the putative reaction in their thermodynamic cycle also included the ring-opening degradation reaction of EC^{-}, whereas we are only considering the ET reaction. An inclusion of the ring-opening reaction would increase the s-EC and EC reduction potentials by approximately 1.3 V (shown in **Table 3.1** and **Table 3.2**) if the ring-opening free energy of reaction in solvent is −30 kcal/mol.[12] The inclusion of the ring-opening reaction does bring our computed reduction potentials ("$\Phi^{\circ}_{\mathrm{Li}^{+}/\mathrm{Li}} + 1.3\ \mathrm{V}$" columns in **Table 3.1** and **Table 3.2**) for EC and s-EC closer to literature values, but they still

differ by approximately 1 V from the experimental value of 0.8 V vs. Li^+/Li.[134] However, compared to theoretical values computed in literature,[10,61] our PDT-derived values only differ by approximately 0.5 V. This discrepancy is further lessened by using the common 1.4 V value along with the ring-opening reaction ("$\Phi^{\circ,(1.4\text{ V})}_{Li^+/Li} + 1.3$ V" columns). However, the goal of this study is to present a workflow where reduction potentials can be computed self-consistently, i.e., using a computed value for $\Phi^{\circ}_{abs}(Li^+/Li)$ to convert to the Li^+/Li scale. Although the rightmost column in **Table 3.1** closely matches the experimental value for EC reduction (0.8 V vs. Li^+/Li), we argue that this result is confounded by its lack of self-consistency in its approach.

Another possible contribution to this discrepancy is related to the limited knowledge of the (electro)chemical environment at the electrode-electrolyte interface (EEI). Electrolyte reduction is expected to occur at the EEI within the electric double layer,[10] wherein the structuring of dipoles and ions are highly ordered and electric potentials are not fully screened, which can greatly impact the solvation free energy. The thermodynamic cycles in **Figure 3.3** do not discriminate between interfacial and bulk solvation and thus introduces a potential source of error that is not easily resolved. Baskin and Prendergast have developed continuum models to describe the speciation at such interfaces and would prove useful in future studies.[137] Another useful tool would be the constant potential method (CPM),[138] which allows for a constant potential, polarizable electrode that can provide an accurate description of the chemical environment at the EEI.

3.4.3 Reorganization Energy

With the free energies of reaction computed, we shift our focus to another major factor that governs ET rates, the reorganization energy, which describes the entire system's response to a transfer of charge. This reorganization energy, λ, can be decomposed into two components,

$$\lambda = \lambda_i + \lambda_o, \tag{3.18}$$

where λ_i and λ_o are the inner- and outer-sphere reorganization energies, respectively. Inner-sphere refers to internal reconfiguration associated with a change in charge, e.g., extension of a bond or loss of planarity. Outer-sphere reorganization refers to the solvent's response to the change in charge state of the oxidant.

EC exhibits both an inner- and outer-sphere response to charge transfer. Once reduced, the sp^2 carbon in the carbonate group bends out of plane to account for the newly acquired electron. The inner-sphere reorganization energy is the energy difference between the bent and flat

conformations for a given charge state, which we've computed to be 46.6 and 35.8 kcal/mol when EC's charge is 0 and −1, respectively. The average of the two quantities gives us an inner-sphere reorganization value of 41.2 kcal/mol, which closely matches what has been computed in literature previously.[95] The inner-sphere reorganization energy was also computed with AIMD calculations in the condensed phase to produce a similar value of 43 kcal/mol. Given that there is little difference between the two computed λ_i values, we conclude that there is a limited impact on inner-sphere response by the solvent degrees of freedom. All inner-sphere reorganization energy values are shown in **Table 3.3**. The inner-sphere reorganization energy is applied to both EC and s-EC in this work.

Table 3.3: PBE/DZVP energies of bent and flat configurations of EC with net charges of 0 and -1 (relative to flat, neutral EC, i.e., **Figure 3.1c**). Inner-sphere reorganization energies for each charge state are shown on the right. All energies are in kcal/mol.

Charge ($\|e\|$)	Flat	Bent	λ_i
0	0.0	46.6	46.6
-1	39.9	4.1	35.8
		Mean $\lambda_{i,DFT}$	41.2
		Mean $\lambda_{i,AIMD}$	43

Outer-sphere reorganization energies, λ_o, were computed by constructing the full Marcus parabolas along the solvent coordinate, shown in **Figure 3.6**. EC and s-EC were held directly at the interface during the construction of the Marcus parabolas. In the classical potential, no new force-field parameters were created to account for the EC^- bent structure (**Figure 3.1d**) and instead neutral EC parameters were used. Thus, the reorganization energies from **Figure 3.6** represent only outer-sphere response. The hydroxyl-terminated graphite surface (**Figure 3.1a**) that was used in this study is not polarizable; however, we are interested in computing reorganization energies at the interface, which have been shown to remain stable across a range of voltages.[97]

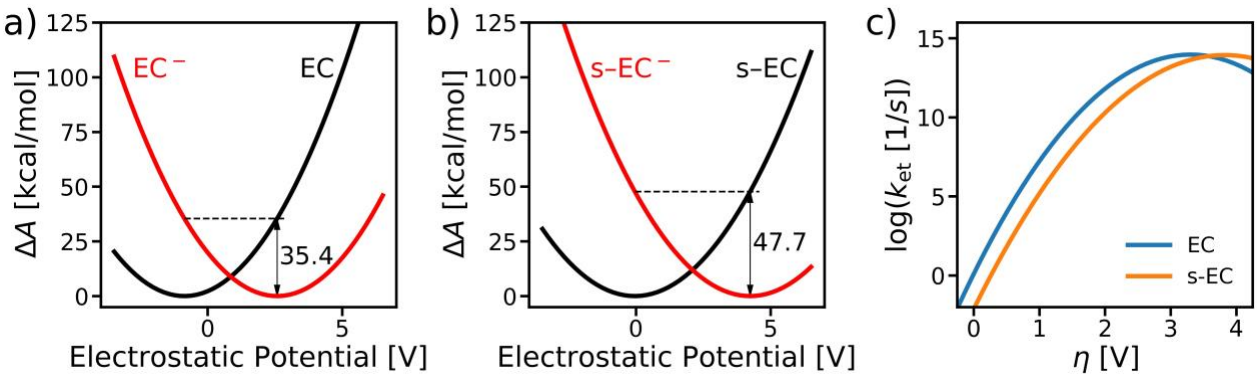

Figure 3.6: Marcus parabolas along solvent coordinate for a) EC and b) s-EC. The black and red curves in (a) and (b) denote the reactant and product states, respectively, with outer-sphere reorganization energies labeled. Parabolas are shown for the case of $\Delta A'_{rxn}$ =0, which also corresponds to η = 0. c) Relationship between predicted rate constant for electron transfer and overpotential, η, for EC and s-EC.

For both EC and s-EC, we see large contributions from the solvent (35.4 and 47.7 kcal/mol, respectively) that go into the full reorganization energy. Leung previously employed an implicit solvent model to estimate the full s-EC reorganization energy at 47.3 kcal/mol, which is nearly the same amount as the value computed in this work for purely the outer-sphere contribution. Overall, the full reorganization energies for EC and s-EC are estimated at 76.6 and 88.9 kcal/mol, respectively. This result demonstrates the strength of the solvent's response to EC reduction and highlights the importance of explicit solvation.

3.4.4 Prediction of Electron Transfer Rate Constants

With both free energies of reaction and full reorganization energies computed for EC and s-EC, the last remaining unknown quantity in Eq. (3.1) is the electronic coupling, V_{AB}. However, it is expected that the reduction of EC during SEI growth occurs in the adiabatic regime of ET, implying that the electronic coupling is high. To approximate this, we assume that $|V_{AB}|$ = 100 meV. We also tested a range of values and found that there was a negligible impact on the trends reported herein. Although we strived for self-consistency to obtain values for the ET rate constant within the molecular framework presented in this chapter, computing the diabatic couplings remains a challenge. Currently we subscribe to the theory of Ref. 139 for the condensed phase. However, further modifications of this theory have been proposed in Ref. 140 and will be the focus of a future study.

With each quantity computed or defined, we can introduce a dependence on an overpotential which adjusts the systems free energy of reaction,[114]

$$\Delta A^{\circ}_{\mathrm{rxn}}(\eta) = \Delta A_{\mathrm{rxn}} + \eta \Delta q, \qquad 3.19$$

where η is the overpotential and Δq is the total change in charge (i.e., -1).[114] We estimated the ET rate constant as a function of overpotential, which is shown in **Figure 3.6c**. An overpotential of 0 is assigned for the case of $\Delta A^{\circ}_{\mathrm{rxn}} = 0$.[114]

For both EC and s-EC there is an apparent peak in the rate constants of ET between 3-4 V in overpotential, wherein the rate constants decrease as driving force increases due to the inverted region. However, systems do not typically operate at such large overpotentials and the inverted region is not expected to be reached. EC seemingly exhibits a larger ET rate constant than s-EC for overpotentials up to the inverted region, but both systems have been scaled to $\eta = 0$ when $\Delta A^{\circ}_{\mathrm{rxn}} = 0$, respectively. Since the overpotential describes the deviation from theoretical reduction potential values, **Figure 3.6c** shows that EC has a slightly larger ET rate constant than s-EC when at equilibrium, but s-EC is still more thermodynamically favorable due to its higher reduction potentials in **Table 3.1** and **Table 3.2**. The primary reason for EC having a higher ET rate constant at equilibrium is due to its lower reorganization energy over s-EC because in the limit of $\Delta A_{\mathrm{rxn}} = 0$, $\Delta A^{\ddagger} = \lambda/4$.

If we assume that η represents the deviation from the theoretical reduction potential,[141] then setting the $\eta = 0$ locations to the respective Φ° for each curve would demonstrate that k_{et} for EC and s-EC are nearly overlapping in the region of their reduction potentials, demonstrating the competition between kinetics and thermodynamics for this system. Kim, et al. also demonstrated that changes in electrode potential had a minimal effect on the reorganization energy using a constant potential method for a model platinum metal electrode.[97] Although this approach would likely impact the absolute value of outer-sphere reorganization energies, the trend between EC and s-EC would not be expected to change.

3.5 Conclusions

In conclusion, we have utilized the potential distribution theorem to describe solvation and compared to the SMD implicit solvent model in DFT in the prediction of reduction potentials for Li^+, EC, and s-EC. Our results highlighted the impact of solvation free energy regarding the disparity between the commonly used 1.4 V for $\Phi^{\circ}_{\mathrm{abs}}(\mathrm{Li}^+/\mathrm{Li})$ and our computed values, which

were lower by 1-2 V. Moreover, we have established a workflow for the prediction of rate constants of electron transfer in heterogeneous reduction reactions that require treatment of both inner- and outer-sphere reorganization. We find that s-EC is more likely to be reduced over pure EC due to their reduction potentials. However, at equilibrium, EC has a faster ET rate constant than s-EC due to its lower reorganization energy. This implies that the kinetics of EC reduction may compete with the favorable thermodynamics of s-EC reduction.

Although we argue the importance of explicit solvation, we acknowledge that the approach in this work is not without limitations. Eq. (3.7) is missing a quantum mechanical contribution term, whereas real solvation free energies should account for quantum mechanical interactions according to Ref. 112. Therefore, the difference in real solvation free energies ($\Delta\mu_X^*$) would also include the difference in quantum mechanical contributions to solvation.

Exciting future works involve an improved description of the chemical environment at the EEI to better mimic an electric double layer with the use of a constant potential, polarizable electrode.[138] In conjunction with more expensive DFT calculations of ion solvation free energies, the constant potential approach would facilitate improved estimations of reduction potentials beyond what are provided in the commonly used thermodynamic cycles in **Figure 3.3**, in addition to better estimates of reorganization energies in the electric double layer. Further, reduced models such as a generalized Langevin equation can also be constructed to estimate electron transfer rates with reactive flux calculations. Experimentally, this work can be supported by measuring Li^+ ion solvation free energy in EC for direct comparison. The measurement of the Li^+/Li reference electrode in EC solvent would also greatly benefit this study.

4 Reaction Coordinate Analysis of Electrolyte Degradation in Bulk vs. Interfacial Environments[3]

4.1 Introduction

A wide array of chemical reactions drive the growth of the solid-electrolyte interphase (SEI) in lithium-ion batteries (LIBs).[2,58,86,92] As a result, there is a large distribution of degradation products throughout the SEI layer, with Li-salt inorganic species near the electrode interface and organic species in the outer-SEI region. In this outer-SEI region, oligomeric species have been detected experimentally[15,16,39,49] and predicted computationally[22,50,90]. In the computational studies of oligomer formation, there is often little discussion about the origins of the initiator species that kick off the cascade of oligomerization reactions. Decomposed electrolyte species with a terminal oxide group are commonly used as an initiator when studying oligomerization reactions.[50,90] These terminal oxide groups can form via a decarboxylation reaction of a carbonate group, in which a CO_2 molecule dissociates away, leaving the anionic oxide.

Given the interfacial nature of the SEI, this work aims to grant insight into the role of an interface on electrolyte degradation reactions, such as the decarboxylation reaction described above. It is known that at interfaces the chemical environment can differ greatly from what is observed in the bulk phase;[142,143] therefore, we plan to examine key electrolyte degradation reactions in the bulk phase and at an interface.

However, to truly understand the underlying mechanism by which a chemical reaction occurs, it is necessary to know the reaction coordinate that governs the chemical transformation. For situations in which the reacting system weakly interacts with its chemical environment, these reaction coordinates can typically be approximated by a couple simple degrees of freedom or less. However, reaction coordinates can become particularly unintuitive in condensed phase systems for even simple reactions, such as the aqueous S_N2 reaction between Cl^- and CH_3Cl.[144,145]

In molecular simulations, it is often necessary to reduce the vast number of degrees of freedom to one or more collective variables to reduce the dimensionality of the system. A collective variable (CV) is simply any quantity that can be calculated from the atomic coordinates in 3D space. However, it is often more useful to use order parameters (OPs), which are CVs that can distinguish between relevant states of interest. Furthermore, the quantity with the most

[3] This chapter features ongoing work and was also supported by Isaiah Lemmon, who developed the transition-sampling Python package for performing aimless shooting simulations and likelihood maximization.

rigorous definition is the reaction coordinate, which can accurately describe the transformation between two states (e.g., reactant and product basins, two conformations of a protein, etc.) and satisfies the committor probability test, which is explained in the methods section below.

Neglecting important degrees of freedom can lead to erroneous descriptions of transition regions. An example of this can be seen in **Figure 4.1**, in which two different 2-dimensional free energy surfaces are projected onto a single CV (s_1). Both surfaces produce the same free energy profile when projected onto s_1. However, the right plots show a case in which the transition from basin A to B can be described sufficiently with a single CV and the true transition state corresponds to the maximum on the s_1 free energy profile. The right panel shows a case in which it is not appropriate to reduce the dimensionality of the system to a single degree of freedom and the free energy maximum along s_1 does not correspond to the transition state for the process.

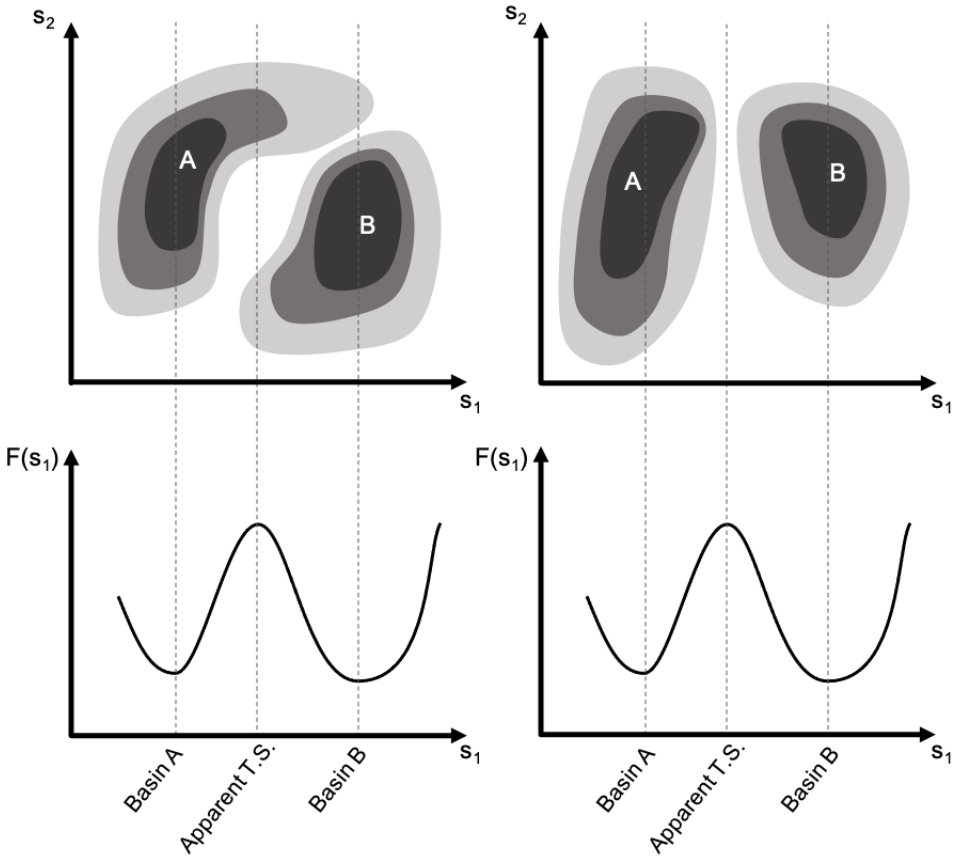

Figure 4.1: Projection of two different 2-dimenstional free energy surfaces (top) onto a 1-dimensional free energy profile (bottom). The labeled peak highlights the location of the apparent transition state (TS) region along the s_1 collective variable. Figure adapted from Ref. 146.

Given the example in **Figure 4.1**, it is clear how a simple CV describing a dynamic process can easily fail. Thus, it is necessary to determine the reaction coordinate of a system if the chemical reaction is to be properly described. However, determining a reaction coordinate can be often be prohibitively time intensive. Peters and Trout have developed a method for effectively estimating reaction coordinates in an automated fashion.[147] The first part of the method is called aimless shooting and involves generating an ensemble of short trajectories originating near the transition region.[147] The statistics of this ensemble and their outcomes can then be used to closely estimate the reaction coordinate of the process through the maximization of a likelihood function.[147]

4.2 Methods

4.2.1 Computational Details

All MD simulations were performed with the CP2K simulation package[70] in the NVT ensemble with a 1 fs time step. The Nosé thermostat[66,67] was used to maintain an average system temperature of 300 K in a 1.5 x 1.5 x 1.5 nm box. The 1-dimensional free energy profile was constructed with ab initio MD (AIMD) and umbrella sampling along the interatomic distance between the CO_2 carbon and oxide oxygen. The Perdew-Burke-Ernzerhof exchange-correlation functional[27] was employed with double zeta basis sets and GTH pseudopotentials[125–128] along with a 300 Ry cutoff for AIMD simulations. Hydrogen masses were set to tritium's to allow the 1 fs time step. The 2-dimensional free energy surface was built using 2-dimensional umbrella sampling with the semi-empirical PM6[68] Hamiltonian to allow for chemical reactions at a relatively low cost. The construction of the free energy profiles were done using weighted histogram analysis method (WHAM).[35,148] All condensed phase systems were constructed using Packmol[149].

4.2.2 The Committor Probability

The committor probability describes the likelihood of a system committing to a particular basin for a given configuration.[150] This quantity is evaluated via a brute force approach in which numerous simulations are launched from a single configuration with random initial conditions. In the typical case of a two-basin system (basins A and B), as depicted in **Figure 4.1**, the probability of committing to basin B, p_B, is given by

$$p_{\mathrm{B}} = \frac{n_{\mathrm{B}}}{n_{\mathrm{A}} + n_{\mathrm{B}}}, \qquad 4.1$$

where n_{A} and n_{B} are the number of simulations that terminated in basin A or B, respectively. Therefore, if a system is at a transition state, then the committor probability for that given configuration will be 50%. Thus, the committor probability would be the ideal reaction coordinate to describe any transition; however, it is extremely computationally expensive to evaluate.

The committor probability can also be used to evaluate the fitness of a reaction coordinate. An ensemble of structures can be taken from the putative transition state region for a given reaction coordinate and their respective committor probabilities can be evaluated. The resulting committor probabilities can be binned into a histogram and the shape of the resulting histogram can indicate the ability of the reaction coordinate to describe the transition region. If the reaction coordinate accurately describes the transition, then there should exist a peak at the 50% marker and the histogram should decay in both directions from 50% (e.g., the ideal curve in **Figure 4.4b**). This indicates that the ensemble of structures was taken near the dividing surface between the two basins. However, if the reaction coordinate poorly describes the process, then the histogram will likely have a different shape (e.g., the estimated curve in **Figure 4.4b**).

4.2.3 Aimless Shooting

In this work, we employ the aimless shooting algorithm[147] to explore the transition state region for the reaction of interest. This process generates an ensemble of structures along the dividing surface that separates two (or more) stable basins. The ensemble of structures that populate the dividing surface can be leveraged to estimate a suitable reaction coordinate by tracking order parameters of each structure, as well as the results of MD trajectories originating from those structures.

The aimless shooting algorithm generates an ensemble of trajectories and structures that are used to estimate the reaction coordinate via likelihood maximization, which will be discussed shortly. Aimless shooting promotes the sampling of structures near the transition state by iteratively generating new structures, or shooting points, from previous trajectories that successfully commit to the two basins of interest.

Initially, a shooting point is pulled from provided guesses at the transition point. Random velocities are then generated (from a Maxwell-Boltzmann distribution with a temperature of 300

K) for the starting structure and the simulation is launched. This simulation is referred to herein as the "forward" trajectory. A second simulation is launched using the negative of the randomly generated velocities and is referred to as the "reverse" trajectory. Depending on where these two trajectories terminate, the shooting point can either be accepted, rejected, or inconclusive. The three possible outcomes are depicted in **Figure 4.2**.

A shooting point that commits to the two separate basins of interests are classified as accepted points (**Figure 4.2a**). When the forward and reverse trajectories of a both commit to the same basin, then the shooting point is rejected (**Figure 4.2b**). Lastly, if one or both trajectories never commit to either of the basins of interest, then the shooting point is classified as inconclusive (**Figure 4.2c**) because it cannot contribute to the statistics during likelihood maximization. A shooting point can be inconclusive when one or both trajectories find a metastable basin that is not near either of the basins of interest, if they find a third basin that is not desired, or if they simply take too long to fall into one of the basins of interest. It should also be noted that the concept of forward and reverse do not necessarily imply a directionality, but rather that the trajectories are launched in opposite directions.

Typically, only accepted and rejected shooting points are considered during likelihood maximization; however, only *accepted* shooting points continue on to generate a new shooting point, shown in **Figure 4.3**. The new shooting point that is generated is randomly chosen from three candidate points, labeled $SP_{-\Delta t}$, SP_0, and $SP_{+\Delta t}$. The shooting point labeled SP_0 is the original accepted shooting point, but the other two points are taken from frames after Δt time steps into the forward ($SP_{+\Delta t}$) and reverse ($SP_{-\Delta t}$) trajectories. Once the new shooting point is chosen, it is randomly assigned one of the labels $SP_{-\Delta t}$, SP_0, and $SP_{+\Delta t}$. If the new shooting point is also accepted, the next three candidate points are then based on relative position to the assigned label.

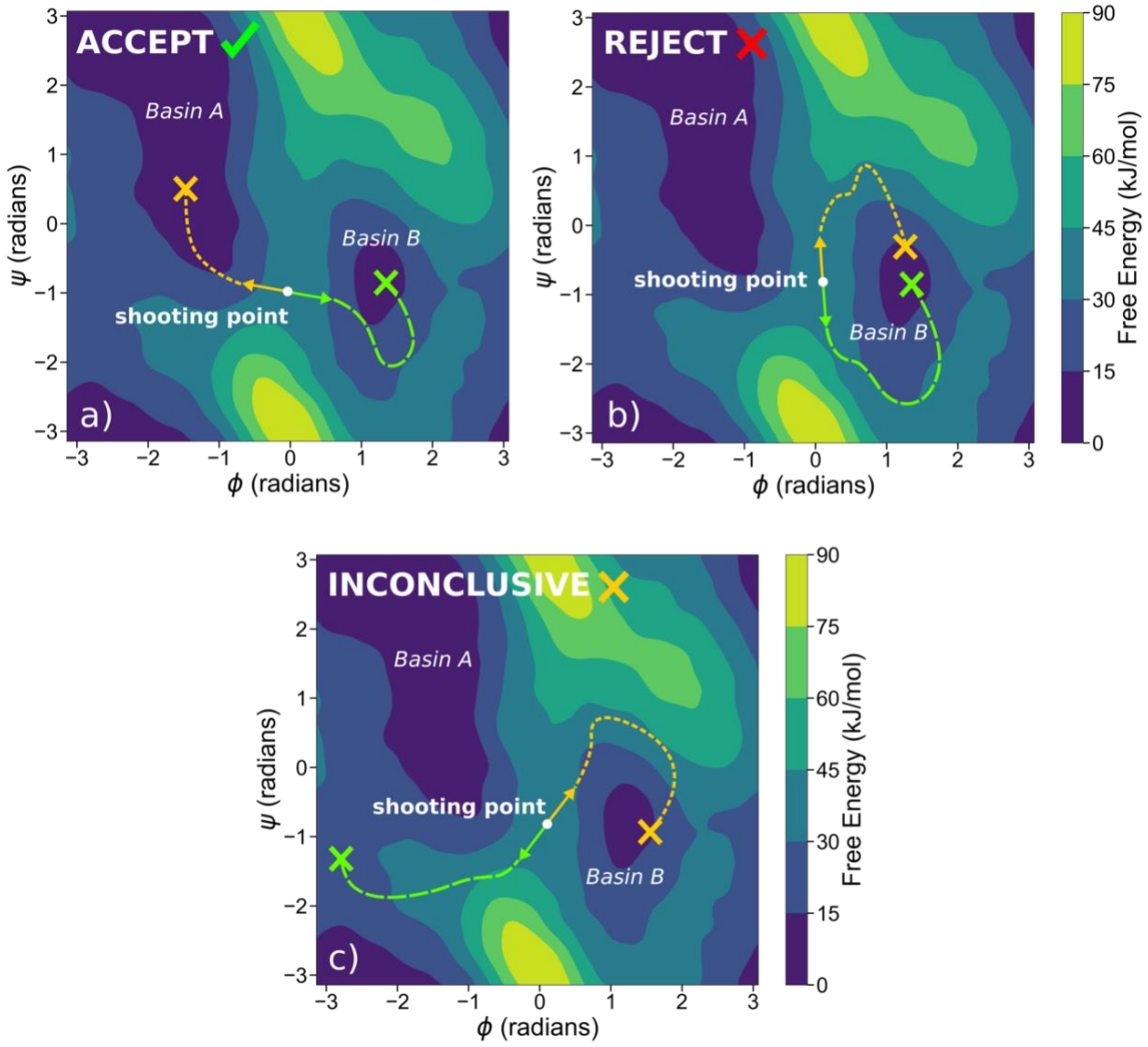

Figure 4.2: Example of the possible outcomes for a given shooting point with forward and reverse trajectories and two basins of interest. a) Accepted shooting point: trajectories commit to separate basins. b) Rejected shooting point: trajectories commit to the same basin. c) Inconclusive shooting point: one or both trajectories never commit to either basin.

After the shooting point has been generated, it is queued to be tested. Once sufficient sampling of the transition region has been achieved, this process never needs to be repeated. The final outputs of aimless shooting are each of the shooting points' structures and to which basins the forward and reverse trajectories committed. The structures are used to generate candidate OPs

and the basin information is used to denote each shooting point as accepted, rejected, or inconclusive for likelihood maximization.

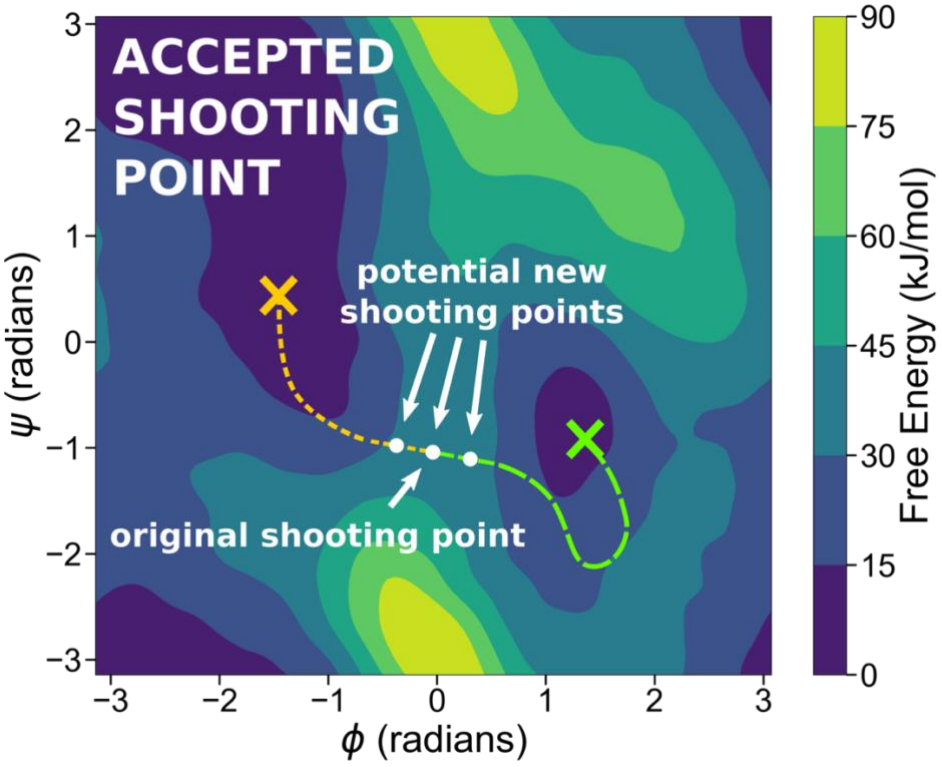

Figure 4.3: Candidate shooting points are generated from accepted shooting points' forward and reverse trajectories. One candidate shooting point is a copy of the original and the other two candidate shooting points are taken Δt time steps into the forward and reverse trajectories.

4.2.4 Likelihood Maximization

When constructing the reaction coordinate, it is beneficial to consider it as a linear combination of OPs:

$$r(\mathbf{q}) = \sum_{k=1}^{m} \alpha_k q_k - \alpha_0, \qquad 4.2$$

where **q** is the vector of OPs that comprise the reaction coordinate, α_k is the linear combination coefficient for each corresponding q_k, α_0 is a constant offset parameter that allows the reaction coordinate to equal 0 at the transition state, and m is the total number of OPs being considered when constructing the reaction coordinate. In this form, the reaction coordinate must have a

maximum probability of being at a transition state when $r(\mathbf{q}) = 0$ and the probability must decay to zero away from the transition state. This can be imposed by approximating the probability of being at a transition state as

$$p(TS|r) = p_0(1 - \tanh^2 r). \tag{4.3}$$

There are two limiting cases for which p_0 can be determined *a priori*. In the case of the system obeying transition state theory, then $p_0 = 1$, but for the case of diffusive barrier crossing dynamics, $p_0 = 0.5$. Otherwise, p_0 can be considered a free parameter along with $\boldsymbol{\alpha}$.[147]

The data being used to determine the most likely reaction coordinate are the accepted and rejected shooting points generated from the aimless shooting step. These data are used to construct the likelihood function,

$$L(\boldsymbol{\alpha}, p_0) = \prod_k^{N_{accepts}} p\left(TS\middle|r\left(\mathbf{q}_{acc}^{(k)}\right)\right) \prod_k^{N_{rejects}} 1 - p\left(TS\middle|r\left(\mathbf{q}_{rej}^{(k)}\right)\right). \tag{4.4}$$

The $\boldsymbol{\alpha}$ and p_0 parameters are then determined by simply maximizing the log of the likelihood, $l = \ln L(\boldsymbol{\alpha}, p_0)$.

$$\boldsymbol{\alpha}, p_0 = \arg\max l(\boldsymbol{\alpha}', p_0'). \tag{4.5}$$

Determining the optimal reaction coordinate starts with using a single OP from which the log likelihood is maximized. The number of OPs that comprise the reaction coordinate is gradually increased until the addition of another OP no longer sufficiently increases the likelihood, i.e., the change in log likelihood is less than $1/2 \ln N_R$, where N_R is the number of realizations of the likelihood function. The algorithm for determining the best estimate of the reaction coordinate is shown below in **Algorithm 4.1**.

Algorithm 4.1 Likelihood maximization procedure after aimless shooting trajectories have been generated. Adapted from Ref. 147.

---

1. Propose *M* candidate OPs and functional forms for $r(\mathbf{q})$ and $p(TS|r)$, such as Equations 6 and 7. Set $m = 1$.
2. For each $C(m, M) = M!/(M - m)!\, m!$ combinations of *m* variables, determine $\boldsymbol{\alpha}$ and p_0 by maximizing the log likelihood as in Equation 9.
3. Let l_m be the maximum log likelihood across all the possible *m* combinations of OPs. If $l_m - l_{m-1} < \frac{1}{2} \ln N_R$ or if $m = M$, then stop. If $l_m - l_{m-1} > \frac{1}{2} \ln N_R$ or if $m = 1$, then let $m = m + 1$.

4.3 Preliminary Results

The key hypothesis of this study is that the important degrees of freedom during a reaction change when the reacting system's environment changes from bulk solvation to an interface. This can be tested by estimating the reaction coordinates of a given reaction in both chemical environments. The model system we will use is the following decarboxylation reaction, in which ethyl carbonate decomposes into ethoxide and CO_2.

$$CH_3CH_2OCO_2^- \rightarrow CH_3CH_2O^- + CO_2 \qquad 4.6$$

However, to first assess the need for robust reaction coordinate estimation, we assume a simple reaction coordinate and test its feasibility in describing the reaction's progress, which is shown in **Figure 4.4**.

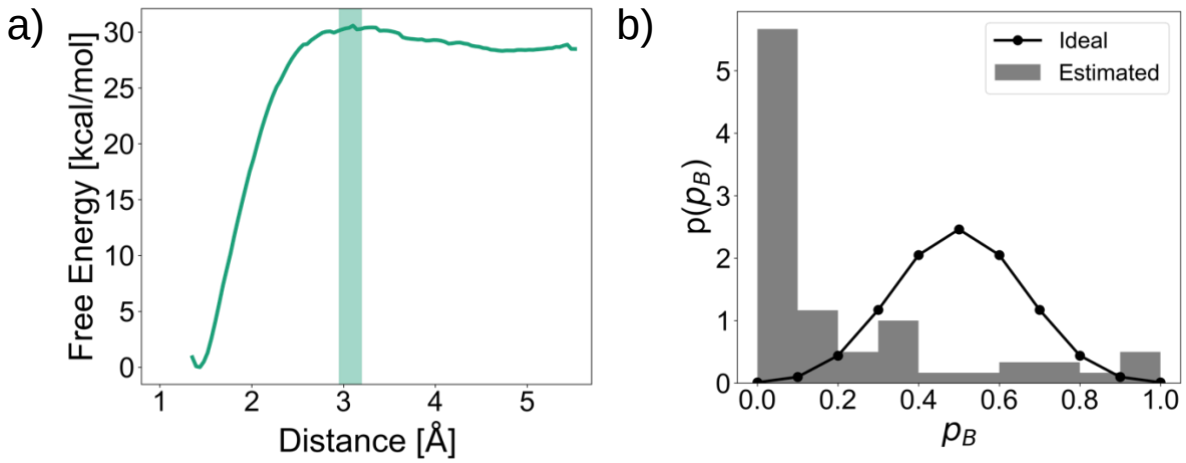

Figure 4.4: a) Free energy profile of the decarboxylation reaction along the distance coordinate between the CO_2 carbon and oxide oxygen without a Li^+ present. b) Committor probability distribution of the ideal (line) and estimated (bar) reaction coordinate at the transition state.

In **Figure 4.4a**, the free energy profile of the decarboxylation reaction in liquid EC solvent was constructed using umbrella sampling with the restrained OP being the interatomic distance between the CO_2 carbon and the oxide oxygen. The highlighted green region denotes the apparent TS along the free energy profile. Sample configurations in the marked TS region were then used to estimate the committor probability distribution, shown in **Figure 4.4b**, where the bar graph denotes the probability densities of estimated committor probabilities, and the line plot denotes the ideal case from the binomial distribution. The key result in **Figure 4.4b** is the complete disagreement between the estimated and ideal distributions, which suggests that the structures used

to build the estimated distribution were not located on the dividing surface between the two basins of interest (i.e., not at the TS). Therefore, we can conclude that the simple interatomic distance OP is insufficient in describing the reaction dynamics and a better coordinate is necessary.

To better understand the impact of a Li^+ counterion on the mechanism of the decarboxylation reaction, we recomputed the free energy profile associated with the reaction, shown in **Figure 4.5**, using 2-dimensional umbrella sampling. The 2D free energy surface (FES) suggests that the decarboxylation reaction is more likely to occur when the Li^+ is directly coordinated with the newly generated oxide group. Additionally, the apparent TS region for the reaction is shifted to farther C–O distances as compared to the apparent TS location in **Figure 4.4a**, which indicates that the inclusion of a Li^+ impacts the reaction thermodynamics.

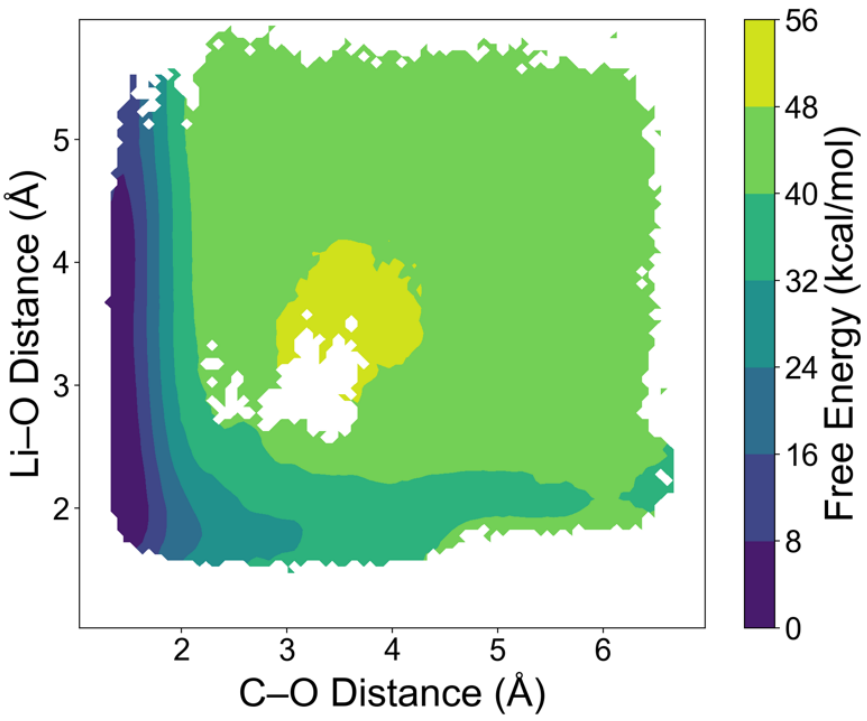

Figure 4.5: 2-dimensional free energy surface of decarboxylation reaction in the presence of a Li^+.

4.4 Future Work

The next steps in this project include the use of the transition-sampling Python package to facilitate aimless shooting simulations to generate ensembles of structures along the dividing surface for the decarboxylation reaction, as well as other key electrolyte degradation reactions,

such as the ring-opening reactions of EC^{-}. For each of these reactions, a set of OPs consisting of both internal and solvent coordinate will be tested to estimate the most likely combination that comprises the optimal reaction coordinate. The resulting reaction coordinates of the likelihood maximization step will be evaluated via a committor analysis as done in **Figure 4.4b**. Once sufficiently accurate reaction coordinates are obtained, the process will be repeated with the reacting systems placed near an air-vapor interface to probe any interfacial effects on the reaction coordinates—and consequently the reaction mechanisms. The estimated reaction coordinates can also be used to assess the ability of metadynamics simulations on constructing 1-dimensional free energy profiles. Kinetic analysis can also be performed using infrequent metadynamics[151] to predict reaction rate constants for each system using estimated reaction coordinates.

5 Summary and Perspective for Future Work

5.1 Summary of Work

While the SEI is a highly complex material, each project has aimed at elucidating various aspects of the SEI growth mechanism in lithium-ion batteries (LIBs). These efforts were made with the goal of engineering battery materials (e.g., electrodes and electrolytes) to have enhanced properties or interactions such that degradative SEI growth is limited or controlled. However, before engineering breakthroughs can occur, there must be a fundamental understanding of the key chemical processes that drive SEI growth.

Chapter 2 discusses later-stage SEI growth and explores the role of common electrolyte additives [fluoroethylene carbonate (FEC) and vinylene carbonate (VC)] on oligomerization reactions. In this project, we used a two-part approach in which we explored the chemical reaction networks of multiple electrolyte molecules, including EC, FEC, and VC. After observing S_N1 oligomerization pathways across each system studied, we used hybrid functional DFT calculations to construct free energy reaction diagrams associated with S_N1 and S_N2 reaction mechanisms. Aside from the impact of FEC and VC additives on the mechanisms, Chapter 2 also examined the feasibility of a ring-opened EC radical (o-EC) to participate in the nucleophilic substitution reactions. While a closed-shell system yielded more favorable energetics, we demonstrated that the o-EC nucleophile can indeed participate in all studied reaction mechanisms. The key result of Chapter 2, however, is the elucidation of the impact that FEC and VC have on oligomerization reactions within the SEI. VC was shown to mitigate oligomerization by behaving as a termination step due to the unfavorable energetics of continued oligomer propagation. FEC, on the other hand, modulates oligomerization by introducing acetal carbons, or branching points, in the oligomeric network, which work to reduce the solubility of oligomeric species. Importantly, these acetal carbons have also been shown experimentally to exist in FEC-containing electrolytes as opposed to electrolytes with no additives.[49] Furthermore, acetal carbons are attributed to the marked improvement in performance for batteries with electrolyte additives. In our work, we demonstrated that acetal carbons are only likely to form via S_N2 mechanism for both studied nucleophiles: ethoxide and o-EC.

Chapter 3 focuses on the earliest stage of SEI growth, which is electrolyte reduction at the electrode-electrolyte interface (EEI). The work discussed in Chapter 3 closely examines the reduction reaction of EC at the EEI, wherein solvation was discussed as a key descriptor of both

the thermodynamics and kinetics of interfacial electron transfer. A statistical mechanical framework was constructed for predicting reduction potentials, wherein solvation effects largely govern the predicted value for a given solvent. We employed the potential distribution theorem (PDT) to compute single-ion solvation free energies directly from molecular simulations, which led to discrepancies in our computed reduction potentials for EC when compared to other works. The major reason for these discrepancies is linked to the conversion from the absolute scale to the Li^+/Li reference electrode scale, which involves the Li^+ reduction potential. Our work predicts a much larger Li^+ reduction potential (2.6 V) than the conventional value of 1.4 V when computed for EC solvent. This demonstrates that there are likely other processes that are unaccounted for when computing reduction potentials following the standard thermodynamic cycles in **Figure 3.3**. Our kinetic analysis focused on the reorganization energy associated with EC reduction. We computed both inner- and outer-sphere contributions to the reorganization energy for EC reduction at the EEI and observed outer-sphere reorganization energies nearly equal to the inner-sphere components, which demonstrates the large magnitude of solvent response. Notably, for the two electron acceptors in the kinetic portion of Chapter 3 [EC and s-EC (EC in the solvation shell of Li^+)], the larger outer-sphere reorganization energy of s-EC vs. EC led to slower electron transfer kinetics despite the more favorable thermodynamics of s-EC reduction over EC. The work in Chapter 3 does not perfectly account for the many complexities of electrochemical interfaces, but it acts as a foundation upon which future works can build toward improved model systems.

Lastly, Chapter 4 describes ongoing work on evaluating the impact of interfacial effects on key electrolyte degradation reactions. The primary focus thus far is on the decarboxylation reaction in which CO_2 dissociates from a terminal carbonate group, leaving an oxide group behind. Attempts to describe the reaction in bulk EC solvation with a single interatomic distance as the putative reaction coordinate highlight the need for an improved descriptor of the reaction. The committor probability distribution for structures at the apparent transition state (TS) greatly deviates from the ideal distribution, indicating that the apparent TS along a 1-dimensional reaction coordinate is insufficient in describing the reactive event.

5.2 Outlook on Future Work

Electrochemical systems are notoriously difficult to study with molecular simulations due to the computationally expensive methods required to accurately describe the molecular

environment, and the inclusion of the SEI only adds to this complexity. The work in this dissertation aims to grant insight into some of the various aspects of SEI growth, but the studied systems were purely focused on Li^+- and EC-based electrolytes. With emerging battery chemistries, small changes—even replacing Li^+ with K^+—can lead to vastly different chemical phenomena than previously observed with standard chemistries.[152] Thus, many techniques that have been previously employed to study LIBs can be adapted to explore and improve promising new technologies, such as sodium-ion, potassium-ion, and lithium-sulfur batteries.

In a direct extension of Chapter 2, the energetic barriers in the reaction diagrams can be applied to study reaction kinetics using kinetic Monte Carlo (KMC), which is a method that uses kinetic data to predict probable product distributions from a discrete set of molecules. In doing so, a concentration dependence could be established for the mitigating effects of FEC and VC in SEI oligomerization reactions (i.e., continual EC oligomerization).

There also exists room for the active development and application of methods for studying electrochemical systems. The constant potential method (CPM) is an empirical approach that allows for the simulation of a polarizable interface[138], thereby enabling new studies of electrode potential on interfacial phenomena, such as reorganization energies and binding affinities of electrolyte species. Recent developments to the projector-operator based diabatization (POD) scheme by Carter-Fenk, et al. have enabled heterogeneous electron transfer studies to provide greater specificity of probable electron acceptor sites, which goes beyond the typical pairwise electronic coupling strengths between donor and acceptor states.[140] This method would facilitate better estimates of electron transfer rate constants with Marcus kinetics.

Appendix A: Commonly Used Notations

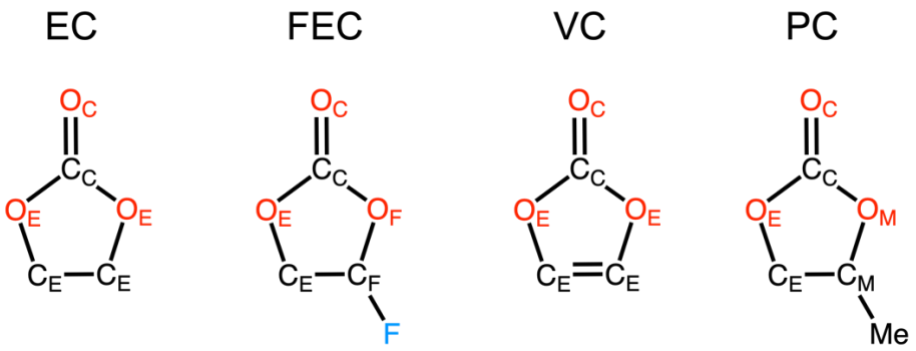

Figure A-1: Atom labels for EC, FEC, VC, and PC molecules.

Table A-1: Glossary of acronym definitions used in main text.

Acronym	Definition
EC	Ethylene carbonate
FEC	Fluoroethylene carbonate
VC	Vinylene carbonate
PC	Propylene carbonate
DMC	Dimethyl carbonate
EMC	Ethyl methyl carbonate
c-EC$^-$	Cyclic, reduced ethylene carbonate
o-EC$^-$	Ring-opened, reduced ethylene carbonate with broken O_E-C_E bond
s-EC	Ethylene carbonate in the solvation shell of a Li^+
AIMD	*Ab initio* molecular dynamics
DFT	Density functional theory
MetaD	Metadynamics
PDT	Potential distribution theorem
CV	Collective variable
OP	Order parameter

Appendix B: Supplementary Information for Chapter 2

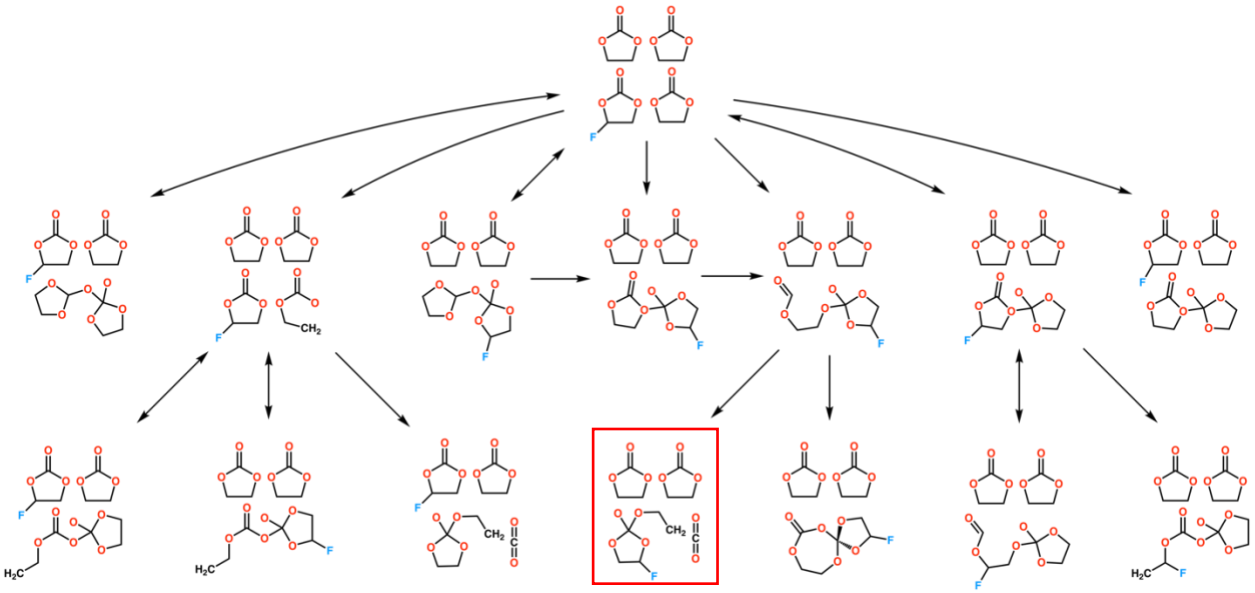

Figure B-1: Reaction network of 1 FEC molecule, 3 EC molecules, and 1 Li+ with an extra electron. The boxed molecules indicate the node in the reaction network that contains the open-shell SN1 adduct with FEC, as well as two intact EC molecules and CO2. Constructed from ~50 separate reactive MD trajectories using mdstates. Although Li+ was included in the simulations, it is not pictured in the reaction network.

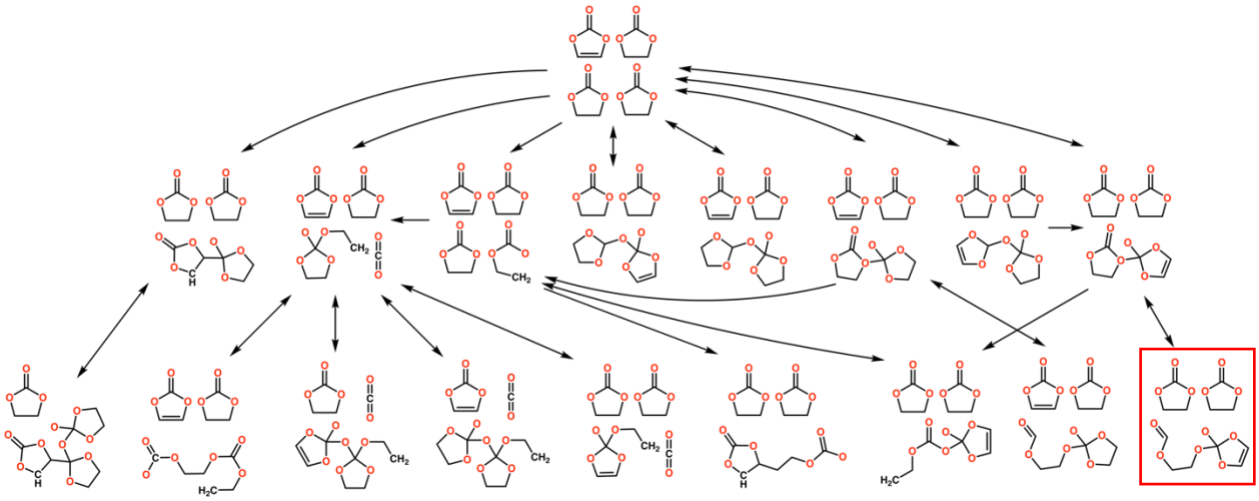

Figure B-2: Reaction network of 1 VC molecule, 3 EC molecules, and 1 Li^+ with an extra electron. The boxed molecules indicate the node in the reaction network that contains the open-shell S_N1 adduct with VC, as well as two intact EC molecules and CO_2. Constructed from ~50 separate reactive MD trajectories using *mdstates*. Although Li^+ was included in the simulations, it is not pictured in the reaction network.

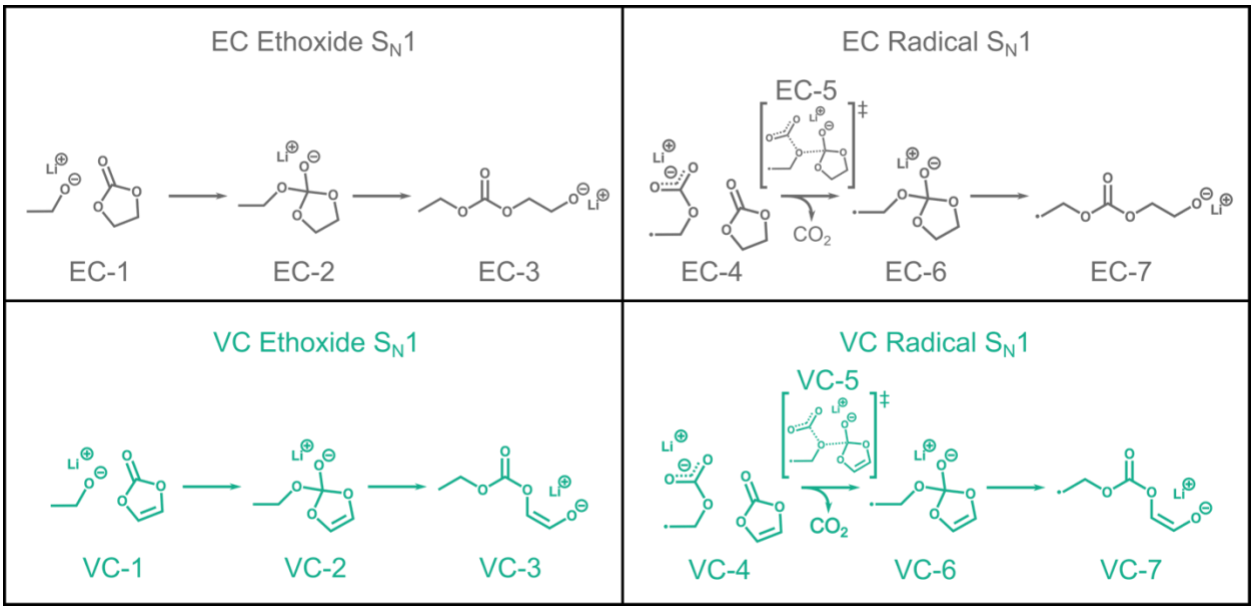

Figure B-3: S_N1 mechanisms for combinations of EC and VC electrophiles and ethoxide and o-EC nucleophiles.

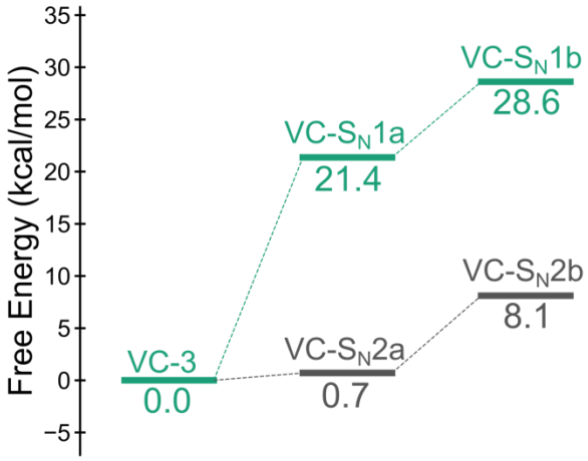

Figure B-4: Reaction diagram of VC-3 structure oligomerizing with an EC via S_N1(green) and S_N2 (gray) mechanisms. The S_N1 and S_N2 states along the reaction path correspond to the stable structures in Figure 1a and 1b in the main text, respectively.

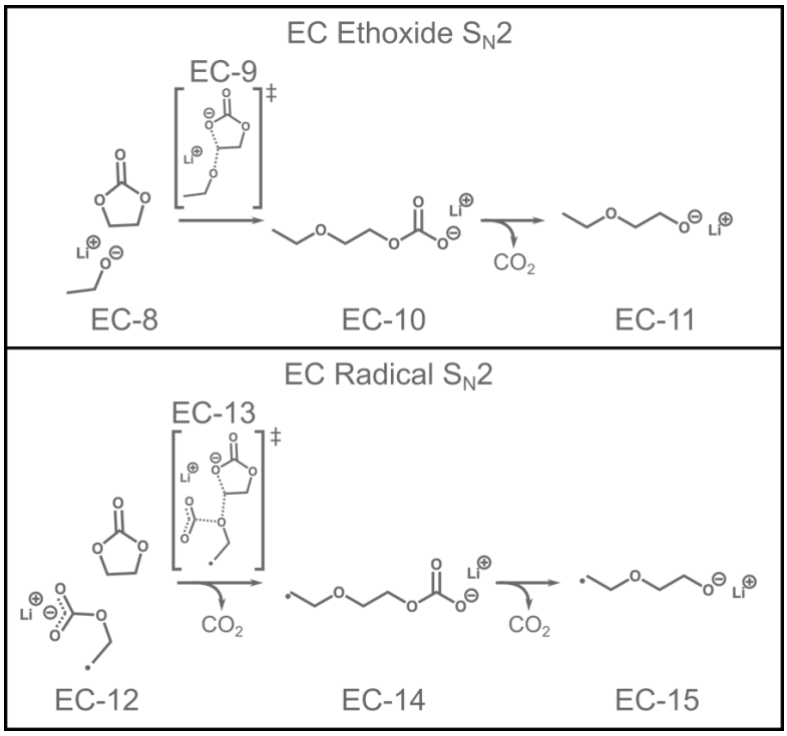

Figure B-5: S_N2 mechanisms for EC with both ethoxide and o-EC nucleophiles.

Table B-1: Transition state (TS) structures with XYZ coordinates in Å.

TS Description	XYZ coordinates
Decarboxylation step during ethenolate formation in **Figure 2.3**	C -2.36093 -2.41900 -3.36309 O -3.62781 -3.29322 -4.80691 O -2.00266 -1.44127 -3.90460 C -3.77018 -2.66120 -5.94483 C -4.51189 -3.04148 -7.01135 O -2.47108 -3.23595 -2.52607 H -4.54152 -2.41746 -7.89772 H -3.21283 -1.71598 -6.01868 H -5.08889 -3.96265 -7.01159 Li -4.31786 -4.91547 -4.16552

EC-5 in **Figure 2.4**

C	0.85021	-0.10891	-0.71284
O	1.23043	-1.17791	0.09969
O	1.80300	0.88689	-0.56160
C	2.13067	-0.70221	1.10582
C	2.32425	0.77991	0.76329
O	0.47491	-0.37396	-1.88540
H	3.05827	-1.27506	1.02863
H	1.69844	-0.84515	2.09857
H	3.37127	1.08391	0.74343
H	1.76548	1.43223	1.43958
C	-1.61675	-0.96110	0.57829
O	-0.42145	0.46408	0.17708
O	-1.65218	-1.01618	1.75135
C	-1.08747	1.55620	-0.45795
C	-2.12697	2.12636	0.42360
O	-1.98224	-1.37444	-0.48735
H	-1.52036	1.24335	-1.41827
H	-0.31762	2.30953	-0.69525
H	-1.96398	2.18962	1.49421
H	-2.96970	2.65254	-0.01158
Li	-1.03653	-1.33089	-2.16835

FEC-5 in **Figure 2.4**

C	0.85644	-0.05395	-0.65468
O	1.28926	-1.10050	0.13843
O	1.72812	1.04181	-0.40737
C	2.00006	-0.53707	1.23980
C	2.56939	0.73457	0.64313
O	0.54648	-0.28179	-1.84100
H	2.77198	-1.23331	1.56431
H	1.32207	-0.30700	2.06554
H	2.68117	1.57582	1.32567
C	-1.59387	-0.99149	0.45605
O	-0.48796	0.42485	0.21561
O	-1.68907	-1.16036	1.62064
C	-1.17436	1.53194	-0.39050
C	-2.27638	2.00145	0.47283
O	-1.92632	-1.36908	-0.64158
H	-1.54354	1.25546	-1.38596
H	-0.42132	2.32174	-0.53546
H	-2.14690	2.04871	1.54872
H	-3.14753	2.46682	0.02554
Li	-0.94586	-1.24403	-2.28209
F	3.85318	0.48973	0.11702

VC-5 in **Figure 2.4**

C	0.85225	-0.07900	-0.65368
O	1.24470	-1.13477	0.19802
O	1.77436	0.95871	-0.43834
C	2.14630	-0.59621	1.09052
C	2.45951	0.63849	0.71459
O	0.52451	-0.34550	-1.82860
C	-1.62242	-0.94264	0.54252
O	-0.46953	0.45882	0.21113
O	-1.71351	-1.03195	1.71375
C	-1.13742	1.54939	-0.43833
C	-2.19383	2.10740	0.42951
O	-1.95377	-1.36669	-0.53567
H	-1.55138	1.23047	-1.40388
H	-0.36684	2.30576	-0.65685
H	-2.02902	2.20574	1.49710
H	-3.06163	2.58081	-0.01610
Li	-0.99608	-1.29235	-2.19787
H	3.13329	1.37384	1.12390
H	2.47889	-1.21244	1.91035

EC-9 in **Figure 2.5**

O	-0.62501	-0.76477	-2.12132
C	0.20318	-0.05759	-2.96403
C	0.49212	-0.79654	-4.27217
H	1.18901	0.16936	-2.49017
H	-0.21469	0.94074	-3.23187
H	1.14989	-0.21145	-4.92677
C	-0.01033	0.51457	2.05209
O	-0.88041	1.02422	1.25884
O	0.70427	-0.49188	1.52998
C	-0.73758	0.21840	-0.27458
C	0.28881	-0.79670	0.16937
O	0.21093	0.86788	3.21208
H	-0.42317	1.08992	-0.82868
H	-1.77306	-0.06640	-0.35560
H	1.18288	-0.76047	-0.44845
H	-0.12175	-1.80409	0.17428
Li	-0.48703	2.32622	4.27160
H	0.97673	-1.75849	-4.07223
H	-0.43897	-0.99479	-4.81446

FEC-9 in **Figure 2.5**

O	-1.00321	1.21907	-0.10000
C	-0.05740	1.84837	-0.90129
C	-0.06886	1.32644	-2.33435
H	0.96673	1.71564	-0.49533
H	-0.22462	2.94327	-0.92919
H	0.68453	1.83705	-2.94410
C	-0.12391	2.26754	4.09570
O	-1.08900	2.74616	3.40598
O	0.57267	1.27475	3.41071
C	-0.99422	2.00583	1.76925
C	-0.07129	0.90825	2.23388
O	0.24831	2.56898	5.21047
H	-0.57587	2.89148	1.31745
H	-2.05515	1.83622	1.71395
H	0.68043	0.63173	1.50074
F	-0.82686	-0.23589	2.50301
Li	-2.05668	-0.27635	-0.37622
H	0.14597	0.25280	-2.35739
H	-1.04831	1.48826	-2.79636

EC-13 in **Figure 2.5**

C	-0.90500	0.12480	-0.98772
O	-1.23626	1.37502	-0.26684
O	0.27955	-0.04662	-1.20371
C	-0.15117	2.18822	0.26325
C	0.28025	1.75726	1.60890
O	-1.93795	-0.50460	-1.24497
H	-0.52026	3.21538	0.25687
H	0.65591	2.11305	-0.47296
H	0.45809	0.70833	1.81474
C	-5.52389	1.75651	0.62353
O	-4.96841	1.89083	-0.64404
O	-4.67331	1.80149	1.56069
C	-3.60112	2.27773	-0.59591
C	-2.88148	1.56943	0.52626
O	-6.74038	1.59896	0.67655
H	-3.52633	3.36191	-0.46660
H	-3.16988	1.99849	-1.55526
H	-2.45704	2.11651	1.35308
H	-3.02745	0.50736	0.64534
Li	-2.21959	-2.08214	-2.31598
H	0.54018	2.49325	2.35950

FEC-13 in **Figure 2.5**

C	-0.64842	0.07917	-0.97464
O	-1.25358	1.30184	-0.35760
O	0.56007	0.11534	-1.08127
C	-0.35941	2.27362	0.25392
C	0.00489	1.92265	1.64216
O	-1.53241	-0.72901	-1.26876
H	-0.87386	3.23547	0.19715
H	0.51468	2.32264	-0.40373
H	0.31433	0.91331	1.88667
C	-5.37106	2.12315	0.92991
O	-4.63287	2.91859	0.00959
O	-4.80400	1.02974	1.19256
C	-3.59171	2.24246	-0.57954
C	-2.95709	1.21868	0.33778
O	-6.41251	2.60922	1.33346
H	-2.87669	2.98244	-0.93541
F	-4.06438	1.57347	-1.71419
H	-2.63041	1.52304	1.32084
H	-3.03099	0.17088	0.10086
Li	-1.77632	-2.30353	-2.34766
H	0.09621	2.69796	2.39262

References

(1) Thompson, A. W. Economic Implications of Lithium Ion Battery Degradation for Vehicle-to-Grid (V2X) Services. *J. Power Sources* **2018**, *396*, 691–709.

(2) Peled, E. The Electrochemical Behavior of Alkali and Alkaline Earth Metals in Nonaqueous Battery Systems—The Solid Electrolyte Interphase Model. *J. Electrochem. Soc.* **1979**, *126* (12), 2047.

(3) Soto, F. A.; Ma, Y.; Martinez De La Hoz, J. M.; Seminario, J. M.; Balbuena, P. B. Formation and Growth Mechanisms of Solid-Electrolyte Interphase Layers in Rechargeable Batteries. *Chem. Mater.* **2015**, *27* (23), 7990–8000.

(4) Verma, P.; Maire, P.; Novák, P. A Review of the Features and Analyses of the Solid Electrolyte Interphase in Li-Ion Batteries. *Electrochim. Acta* **2010**, *55* (22), 6332–6341.

(5) Ushirogata, K.; Sodeyama, K.; Futera, Z.; Tateyama, Y.; Okuno, Y. Near-Shore Aggregation Mechanism of Electrolyte Decomposition Products to Explain Solid Electrolyte Interphase Formation. *J. Electrochem. Soc.* **2015**, *162* (14), A2670–A2678.

(6) Peled, E.; Golodnitsky, D.; Ardel, G. Advanced Model for Solid Electrolyte Interphase Electrodes in Liquid and Polymer Electrolytes. *J. Electrochem. Soc.* **1997**, *144* (8), L208.

(7) Ganesh, P.; Kent, P. R. C.; Jiang, D. E. Solid-Electrolyte Interphase Formation and Electrolyte Reduction at Li-Ion Battery Graphite Anodes: Insights from First-Principles Molecular Dynamics. *J. Phys. Chem. C* **2012**, *116* (46), 24476–24481.

(8) Kim, S. P.; van Duin, A. C. T.; Shenoy, V. B. Effect of Electrolytes on the Structure and Evolution of the Solid Electrolyte Interphase (SEI) in Li-Ion Batteries: A Molecular Dynamics Study. *J. Power Sources* **2011**, *196* (20), 8590–8597.

(9) Benitez, L.; Cristancho, D.; Sminario, J.; Martinez, J.; Balbuena, P. B. Electron Transfer through SEI Layers Formed on Si Anodes of Li-Ion Batteries. *Electrochim. Acta* **2014**, *140*, 250–257.

(10) Leung, K. Two-Electron Reduction of Ethylene Carbonate: A Quantum Chemistry Re-Examination of Mechanisms. *Chem. Phys. Lett.* **2013**, *568–569*, 1–8.

(11) Yu, J.; Balbuena, P. B.; Budzien, J.; Leung, K. Hybrid DFT Functional-Based Static and Molecular Dynamics Studies of Excess Electron in Liquid Ethylene Carbonate. *J. Electrochem. Soc.* **2011**, *158* (4), A400.

(12) Wang, Y.; Nakamura, S.; Ue, M.; Balbuena, P. B. Theoretical Studies to Understand

Surface Chemistry on Carbon Anodes for Lithium-Ion Batteries: Reduction Mechanisms of Ethylene Carbonate. *J. Am. Chem. Soc.* **2001**, *123* (47), 11708–11718.

(13) Li, Y.; Li, Y.; Pei, A.; Yan, K.; Sun, Y.; Wu, C. L.; Joubert, L. M.; Chin, R.; Koh, A. L.; Yu, Y.; et al. Atomic Structure of Sensitive Battery Materials and Interfaces Revealed by Cryo–Electron Microscopy. *Science (80-.).* **2017**, *358* (6362), 506–510.

(14) Shkrob, I. A.; Zhu, Y.; Marin, T. W.; Abraham, D. Reduction of Carbonate Electrolytes and the Formation of Solid-Electrolyte Interface (SEI) in Lithium-Ion Batteries. 1. Spectroscopic Observations of Radical Intermediates Generated in One-Electron Reduction of Carbonates. *J. Phys. Chem. C* **2013**, *117* (38), 19255–19269.

(15) Shkrob, I. A.; Zhu, Y.; Marin, T. W.; Abraham, D. Reduction of Carbonate Electrolytes and the Formation of Solid-Electrolyte Interface (SEI) in Lithium-Ion Batteries. 2. Radiolytically Induced Polymerization of Ethylene Carbonate. *J. Phys. Chem. C* **2013**, *117* (38), 19270–19279.

(16) Wang, Y.; Balbuena, P. B. Theoretical Insights into the Reductive Decompositions of Propylene Carbonate and Vinylene Carbonate: Density Functional Theory Studies. *J. Phys. Chem. B* **2002**, *106* (17), 4486–4495.

(17) Leung, K.; Rempe, S. B.; Foster, M. E.; Ma, Y.; Martinez del la Hoz, J. M.; Sai, N.; Balbuena, P. B. Modeling Electrochemical Decomposition of Fluoroethylene Carbonate on Silicon Anode Surfaces in Lithium Ion Batteries. *J. Electrochem. Soc.* **2014**, *161* (3), A213–A221.

(18) Gomez-Ballesteros, J. L.; Balbuena, P. B. Reduction of Electrolyte Components on a Coated Si Anode of Lithium-Ion Batteries. *J. Phys. Chem. Lett.* **2017**, *8* (14), 3404–3408.

(19) Leung, K. Electronic Structure Modeling of Electrochemical Reactions at Electrode/Electrolyte Interfaces in Lithium Ion Batteries. *J. Phys. Chem. C* **2013**, *117* (4), 1539–1547.

(20) Van Duin, A. C. T.; Dasgupta, S.; Lorant, F.; Goddard, W. A. ReaxFF: A Reactive Force Field for Hydrocarbons. *J. Phys. Chem. A* **2001**, *105* (41), 9396–9409.

(21) Islam, M.; Kolesov, G.; Verstraelen, T.; Kaxiras, E.; Duin, A. C. T. Van. EReaxFF: A Pseudoclassical Treatment of Explicit Electrons within Reactive Force Field Simulations. *J. Chem. Theory Comput.* **2016**, *12* (8), 3463–3472.

(22) Bedrov, D.; Smith, G. D.; Van Duin, A. C. T. Reactions of Singly-Reduced Ethylene

Carbonate in Lithium Battery Electrolytes: A Molecular Dynamics Simulation Study Using the ReaxFF. *J. Phys. Chem. A* **2012**, *116* (11), 2978–2985.

(23) Islam, M. M.; Van Duin, A. C. T. Reductive Decomposition Reactions of Ethylene Carbonate by Explicit Electron Transfer from Lithium: An EReaxFF Molecular Dynamics Study. *J. Phys. Chem. C* **2016**, *120* (48), 27128–27134.

(24) Stewart, J. J. P. Optimization of Parameters for Semiempirical Methods V: Modification of NDDO Approximations and Application to 70 Elements. *J. Mol. Model.* **2007**, *13* (12), 1173–1213.

(25) Elstner, M.; Porezag, D.; Jungnickel, G.; Elsner, J.; Haugk, M.; Frauenheim, T.; Suhai, S.; Seifert, G. Self-Consistent-Charge Density-Functional Tight-Binding Method for Simulations of Complex Materials Properties. *Phys. Rev. B* **1998**, *58* (11), 7260–7268.

(26) Born, M.; Oppenheimer, R. Zur Quantentheorie Der Molekeln. *Ann. Phys.* **1927**, *389* (20), 457–484.

(27) Perdew, J. P.; Burke, K.; Ernzerhof, M. Generalized Gradient Approximation Made Simple - The PBE Functional. *Phys. Rev. Lett.* **1996**, *77* (18), 3865–3868.

(28) Perdew, J. P.; Burke, K.; Ernzerhof, M. Generalized Gradient Approximation Made Simple [Phys. Rev. Lett. 77, 3865 (1996)]. *Phys. Rev. Lett.* **1997**, *78* (7), 1396.

(29) Becke, A. D. Density-Functional Thermochemistry. III. The Role of Exact Exchange. *J. Chem. Phys.* **1993**, *98* (7), 5648–5652.

(30) Lee, C.; Yang, W.; Parr, R. G. Development of the Colle-Salvetti Correlation-Energy Formula into a Functional of the Electron Density. *Phys. Rev. B* **1988**, *37* (2), 785–789.

(31) Vosko, S. H.; Wilk, L.; Nusair, M. Accurate Spin-Dependent Electron Liquid Correlation Energies for Local Spin Density Calculations: A Critical Analysis. *Can. J. Phys.* **1980**, *58* (8), 1200–1211.

(32) Stephens, P. J.; Devlin, F. J.; Chabalowski, C. F.; Frisch, M. J. Ab Initio Calculation of Vibrational Absorption and Circular Dichroism Spectra Using Density Functional Force Fields. *J. Phys. Chem.* **1994**, *98* (45), 11623–11627.

(33) Torrie, G. M.; Valleau, J. P. Nonphysical Sampling Distributions in Monte Carlo Free-Energy Estimation: Umbrella Sampling. *J. Comput. Phys.* **1977**, *23* (2), 187–199.

(34) Valsson, O.; Tiwary, P.; Parrinello, M. Enhancing Important Fluctuations: Rare Events and Metadynamics from a Conceptual Viewpoint. *Annu. Rev. Phys. Chem.* **2016**, *67* (1), 159–

184.

(35) Kumar, S.; Rosenberg, J. M.; Bouzida, D.; Swendsen, R. H.; Kollman, P. A. Multidimensional Free-Energy Calculations Using the Weighted Histogram Analysis Method. *J. Comput. Chem.* **1995**, *16* (11), 1339–1350.

(36) Shirts, M. R.; Chodera, J. D. Statistically Optimal Analysis of Samples from Multiple Equilibrium States. *J. Chem. Phys.* **2008**, *129* (12), 124105.

(37) Barducci, A.; Bussi, G.; Parrinello, M. Well-Tempered Metadynamics: A Smoothly Converging and Tunable Free-Energy Method. *Phys. Rev. Lett.* **2008**, *100* (2), 1–4.

(38) Arora, P.; White, R. E.; Doyle, M. Capacity Fade Mechanisms and Side Reactions in Lithium-Ion Batteries. *J. Electrochem. Soc.* **1998**, *145* (10), 3647–3667.

(39) Jin, Y.; Kneusels, N. J. H.; Magusin, P. C. M. M.; Kim, G.; Castillo-Martínez, E.; Marbella, L. E.; Kerber, R. N.; Howe, D. J.; Paul, S.; Liu, T.; et al. Identifying the Structural Basis for the Increased Stability of the Solid Electrolyte Interphase Formed on Silicon with the Additive Fluoroethylene Carbonate. *J. Am. Chem. Soc.* **2017**, *139* (42), 14992–15004.

(40) Ushirogata, K.; Sodeyama, K.; Okuno, Y.; Tateyama, Y. Additive Effect on Reductive Decomposition and Binding of Carbonate-Based Solvent toward Solid Electrolyte Interphase Formation in Lithium-Ion Battery. *J. Am. Chem. Soc.* **2013**, *135* (32), 11967–11974.

(41) Wang, D. Y.; Sinha, N. N.; Burns, J. C.; Aiken, C. P.; Petibon, R.; Dahn, J. R. A Comparative Study of Vinylene Carbonate and Fluoroethylene Carbonate Additives for LiCoO2/Graphite Pouch Cells. *J. Electrochem. Soc.* **2014**, *161* (4), A467–A472.

(42) Kumar, H.; Detsi, E.; Abraham, D. P.; Shenoy, V. B. Fundamental Mechanisms of Solvent Decomposition Involved in Solid-Electrolyte Interphase Formation in Sodium Ion Batteries. *Chem. Mater.* **2016**, *28* (24), 8930–8941.

(43) Okuno, Y.; Ushirogata, K.; Sodeyama, K.; Tateyama, Y. Decomposition of the Fluoroethylene Carbonate Additive and the Glue Effect of Lithium Fluoride Products for the Solid Electrolyte Interphase: An Ab Initio Study. *Phys. Chem. Chem. Phys.* **2016**, *18* (12), 8643–8653.

(44) Schwenke, K. U.; Solchenbach, S.; Demeaux, J.; Lucht, B. L.; Gasteiger, H. A. The Impact of CO 2 Evolved from VC and FEC during Formation of Graphite Anodes in Lithium-Ion Batteries . *J. Electrochem. Soc.* **2019**, *166* (10), A2035–A2047.

(45) Li, Q.; Liu, X.; Han, X.; Xiang, Y.; Zhong, G.; Wang, J.; Zheng, B.; Zhou, J.; Yang, Y. Identification of the Solid Electrolyte Interface on the Si/C Composite Anode with FEC as the Additive. *ACS Appl. Mater. Interfaces* **2019**, *11* (15), 14066–14075.

(46) Leung, K.; Budzien, J. Ab Initio Molecular Dynamics Simulations of the Initial Stages of Solid-Electrolyte Interphase Formation on Lithium Ion Battery Graphitic Anodes. *Phys. Chem. Chem. Phys.* **2010**, *12*, 6583–6586.

(47) Takenaka, N.; Sakai, H.; Suzuki, Y.; Uppula, P.; Nagaoka, M. A Computational Chemical Insight into Microscopic Additive Effect on Solid Electrolyte Interphase Film Formation in Sodium-Ion Batteries: Suppression of Unstable Film Growth by Intact Fluoroethylene Carbonate. *J. Phys. Chem. C* **2015**, *119* (32), 18046–18055.

(48) Shkrob, I. A.; Wishart, J. F.; Abraham, D. P. What Makes Fluoroethylene Carbonate Different? *J. Phys. Chem. C* **2015**, *119* (27), 14954–14964.

(49) Jin, Y.; Kneusels, N. J. H.; Marbella, L. E.; Castillo-Martínez, E.; Magusin, P. C. M. M.; Weatherup, R. S.; Jónsson, E.; Liu, T.; Paul, S.; Grey, C. P. Understanding Fluoroethylene Carbonate and Vinylene Carbonate Based Electrolytes for Si Anodes in Lithium Ion Batteries with NMR Spectroscopy. *J. Am. Chem. Soc.* **2018**, *140* (31), 9854–9867.

(50) Burkhardt, S. E. Impact of Chemical Follow-up Reactions for Lithium Ion Electrolytes: Generation of Nucleophilic Species, Solid Electrolyte Interphase, and Gas Formation. *J. Electrochem. Soc.* **2017**, *164* (4), A684–A690.

(51) Xu, S.; Luo, G.; Jacobs, R.; Fang, S.; Mahanthappa, M. K.; Hamers, R. J.; Morgan, D. Ab Initio Modeling of Electrolyte Molecule Ethylene Carbonate Decomposition Reaction on Li(Ni,Mn,Co)O2 Cathode Surface. *ACS Appl. Mater. Interfaces* **2017**, *9* (24), 20545–20553.

(52) Needham, S. A.; Wang, G. X.; Liu, H. K.; Drozd, V. A.; Liu, R. S. Synthesis and Electrochemical Performance of Doped LiCoO 2 Materials. *J. Power Sources* **2007**, *174* (2), 828–831.

(53) Tebbe, J. L.; Fuerst, T. F.; Musgrave, C. B. Degradation of Ethylene Carbonate Electrolytes of Lithium Ion Batteries via Ring Opening Activated by LiCoO2 Cathode Surfaces and Electrolyte Species. *ACS Appl. Mater. Interfaces* **2016**, *8* (40), 26664–26674.

(54) Sloop, S. E.; Pugh, J. K.; Wang, S.; Kerr, J. B.; Kinoshita, K. Chemical Reactivity of PF5 and LiPF6 in Ethylene Carbonate/Dimethyl Carbonate Solutions. *Electrochem. Solid-State*

Lett. **2001**, *4* (4), A42.

(55) Tasaki, K.; Kanda, K.; Nakamura, S.; Ue, M. Decomposition of LiPF6 and Stability of PF5 in Li-Ion Battery Electrolytes. *J. Electrochem. Soc.* **2003**, *150* (12), A1628.

(56) Aurbach, D. Review of Selected Electrode-Solution Interactions Which Determine the Performance of Li and Li Ion Batteries. *J. Power Sources* **2000**, *89*, 206–218.

(57) Aurbach, D.; Markovsky, B.; Shechter, A.; Ein-Eli, Y. A Comparative Study of Synthetic Graphite and Li Electrodes in Electrolyte Solutions Based on Ethylene Carbonate-Dimethyl Carbonate Mixtures. *J. Electrochem. Soc.* **1996**, *143* (12), 3809–3820.

(58) Wang, A.; Kadam, S.; Li, H.; Shi, S.; Qi, Y. Review on Modeling of the Anode Solid Electrolyte Interphase (SEI) for Lithium-Ion Batteries. *npj Comput. Mater.* **2018**, *4* (15), 1–26.

(59) Li, Y.; Leung, K.; Qi, Y. Computational Exploration of the Li-Electrode|Electrolyte Interface in the Presence of a Nanometer Thick Solid-Electrolyte Interphase Layer. *Acc. Chem. Res.* **2016**, *49* (10), 2363–2370.

(60) Nie, M.; Chalasani, D.; Abraham, D. P.; Chen, Y.; Bose, A.; Lucht, B. L. Lithium Ion Battery Graphite Solid Electrolyte Interphase Revealed by Microscopy and Spectroscopy. *J. Phys. Chem. C* **2013**, *117* (3), 1257–1267.

(61) Delp, S. A.; Borodin, O.; Olguin, M.; Eisner, C. G.; Allen, J. L.; Jow, T. R. Importance of Reduction and Oxidation Stability of High Voltage Electrolytes and Additives. *Electrochim. Acta* **2016**, *209*, 498–510.

(62) Dahbi, M.; Nakano, T.; Yabuuchi, N.; Fujimura, S.; Chihara, K.; Kubota, K.; Son, J. Y.; Cui, Y. T.; Oji, H.; Komaba, S. Effect of Hexafluorophosphate and Fluoroethylene Carbonate on Electrochemical Performance and the Surface Layer of Hard Carbon for Sodium-Ion Batteries. *ChemElectroChem* **2016**, *3* (11), 1856–1867.

(63) Bouibes, A.; Takenaka, N.; Fujie, T.; Kubota, K.; Komaba, S.; Nagaoka, M. Concentration Effect of Fluoroethylene Carbonate on the Formation of Solid Electrolyte Interphase Layer in Sodium-Ion Batteries. *ACS Appl. Mater. Interfaces* **2018**, *10* (34), 28525–28532.

(64) Henschel, J.; Peschel, C.; Günter, F.; Reinhart, G.; Winter, M.; Nowak, S. Reaction Product Analysis of the Most Active “Inactive” Material in Lithium-Ion Batteries - The Electrolyte. II: Battery Operation and Additive Impact. *Chem. Mater.* **2019**, *31* (24), 9977–9983.

(65) Sahore, R.; Dogan, F.; Bloom, I. D. Identification of Electrolyte-Soluble Organic Cross-

Talk Species in a Lithium-Ion Battery via a Two-Compartment Cell. *Chem. Mater.* **2019**, *31* (8), 2884–2891.

(66) Nosé, S. A Unified Formulation of the Constant Temperature Molecular Dynamics Methods. *J. Chem. Phys.* **1984**, *81* (1), 511–519.

(67) Nosé, S. A Molecular Dynamics Method for Simulations in the Canonical Ensemble. *Mol. Phys.* **2002**, *100* (1), 191–198.

(68) Stewart, J. J. P. Optimization of Parameters for Semiempirical Methods V : Modification of NDDO Approximations and Application to 70 Elements. *J. Mol. Model.* **2007**, *13* (12), 1173–1213.

(69) VandeVondele, J.; Hutter, J. An Efficient Orbital Transformation Method for Electronic Structure Calculations. *J. Chem. Phys.* **2003**, *118* (10), 4365–4369.

(70) Hutter, J.; Iannuzzi, M.; Schiffmann, F.; VandeVondele, J. Cp2k: Atomistic Simulations of Condensed Matter Systems. *Wiley Interdiscip. Rev. Comput. Mol. Sci.* **2014**, *4* (1), 15–25.

(71) Kolafa, J. Time-Reversible Always Stable Predictor-Corrector Method for Molecular Dynamics of Polarizable Molecules. *J. Comput. Chem.* **2004**, *25* (3), 335–342.

(72) Schütt, O.; Messmer, P.; Hutter, J.; VandeVondele, J. GPU-Accelerated Sparse Matrix-Matrix Multiplication for Linear Scaling Density Functional Theory. In *Electronic Structure Calculations on Graphics Processing Units: From Quantum Chemistry to Condensed Matter Physics*; John Wiley & Sons, Ltd: Chichester, UK, 2016; pp 173–190.

(73) Borštnik, U.; Vandevondele, J.; Weber, V.; Hutter, J. Sparse Matrix Multiplication: The Distributed Block-Compressed Sparse Row Library. *Parallel Comput.* **2014**, *40* (5–6), 47–58.

(74) Frigo, M.; Johnson, S. G. The Design and Implementation of FFTW3. In *Proceedings of the IEEE*; 2005; Vol. 93, pp 216–231.

(75) Tribello, G. A.; Bonomi, M.; Branduardi, D.; Camilloni, C.; Bussi, G. PLUMED 2: New Feathers for an Old Bird. *Comput. Phys. Commun.* **2014**, *185* (2), 604–613.

(76) Fu, C. D.; Pfaendtner, J. Lifting the Curse of Dimensionality on Enhanced Sampling of Reaction Networks with Parallel Bias Metadynamics. *J. Chem. Theory Comput.* **2018**, *14* (5), 2516–2525.

(77) Zheng, S.; Pfaendtner, J. Enhanced Sampling of Chemical and Biochemical Reactions with Metadynamics. *Mol. Simul.* **2015**, *41* (1–3), 55–72.

(78) Pfaendtner, J.; Bonomi, M. Efficient Sampling of High-Dimensional Free-Energy Landscapes with Parallel Bias Metadynamics. *J. Chem. Theory Comput.* **2015**, *11* (11), 5062–5067.

(79) Pietrucci, F.; Andreoni, W. Graph Theory Meets Ab Initio Molecular Dynamics: Atomic Structures and Transformations at the Nanoscale. *Phys. Rev. Lett.* **2011**, *107* (8), 1–4.

(80) Zheng, S.; Pfaendtner, J. Car-Parrinello Molecular Dynamics + Metadynamics Study of High-Temperature Methanol Oxidation Reactions Using Generic Collective Variables. *J. Phys. Chem. C* **2014**, *118* (20), 10764–10770.

(81) Wang, L. P.; McGibbon, R. T.; Pande, V. S.; Martinez, T. J. Automated Discovery and Refinement of Reactive Molecular Dynamics Pathways. *J. Chem. Theory Comput.* **2016**, *12* (2), 638–649.

(82) Frisch, M. J.; Trucks, G. W.; Schlegel, H. B.; Scuseria, G. E.; Robb, M. A.; Cheeseman, J. R.; Scalmani, G.; Barone, V.; Petersson, G. A.; Nakatsuji, H.; et al. *Gaussian 16, Revision A.03*; Gaussian, Inc.: Wallingford, CT, 2016.

(83) Han, Y. K.; Lee, S. U. Performance of Density Functional for Calculation of Reductive Ring-Opening Reaction Energies of Li+-EC and Li+-VC. *Theor. Chem. Acc.* **2004**, *112* (2), 106–112.

(84) Barone, V.; Cossi, M. Quantum Calculation of Molecular Energies and Energy Gradients in Solution by a Conductor Solvent Model. *J. Phys. Chem. A* **1998**, *102* (11), 1995–2001.

(85) Cossi, M.; Rega, N.; Scalmani, G.; Barone, V. Energies, Structures, and Electronic Properties of Molecules in Solution with the C-PCM Solvation Model. *J. Comput. Chem.* **2003**, *24* (6), 669–681.

(86) Tasaki, K. Solvent Decompositions and Physical Properties of Decomposition Compounds in Li-Ion Battery Electrolytes Studied by DFT Calculations and Molecular Dynamics Simulations. *J. Phys. Chem. B* **2005**, *109* (7), 2920–2933.

(87) Onuki, M.; Kinoshita, S.; Sakata, Y.; Yanagidate, M.; Otake, Y.; Ue, M.; Deguchi, M. Identification of the Source of Evolved Gas in Li-Ion Batteries Using 13C-Labeled Solvents. *J. Electrochem. Soc.* **2008**, *155* (11), A794–A797.

(88) Boyer, M. J.; Hwang, G. S. Theoretical Evaluation of Ethylene Carbonate Anion Transport and Its Impact on Solid Electrolyte Interphase Formation. *Electrochim. Acta* **2018**, *266*, 326–331.

(89) Borodin, O.; Smith, G. D.; Fan, P. Molecular Dynamics Simulations of Lithium Alkyl Carbonates. *J. Phys. Chem. B* **2006**, *110* (45), 22773–22779.

(90) Gibson, L. D.; Pfaendtner, J. Solvent Oligomerization Pathways Facilitated by Electrolyte Additives during Solid-Electrolyte Interphase Formation. *Phys. Chem. Chem. Phys.* **2020**, *22* (37), 21494–21503.

(91) Omichi, K.; Ramos-Sanchez, G.; Rao, R.; Pierce, N.; Chen, G.; Balbuena, P. B.; Harutyunyan, A. R. Origin of Excess Irreversible Capacity in Lithium-Ion Batteries Based on Carbon Nanostructures. *J. Electrochem. Soc.* **2015**, *162* (10), A2106–A2115.

(92) Ramos Sanchez, G. R. S.; Soto, F. A.; Martinez de la Hoz, J. M.; Liu, Z.; Mukherjee, P.; El-Mellouhi, F.; Seminario, J. M.; Balbuena, P. B. Computational Studies of Interfacial Reactions at Anode Materials: Initial Stages of the Solid-Electrolyte-Interphase Layer Formation. *J. Electrochem. Energy Convers. Storage* **2016**, *13* (August), 1–10.

(93) Vollmer, J. M.; Curtiss, L. A.; Vissers, D. R.; Amine, K. Reduction Mechanisms of Ethylene, Propylene, and Vinylethylene Carbonates. *J. Electrochem. Soc.* **2004**, *151* (1), A178.

(94) Tavassol, H.; Buthker, J. W.; Ferguson, G. A.; Curtiss, L. A.; Gewirth, A. A. Solvent Oligomerization during SEI Formation on Model Systems for Li-Ion Battery Anodes. *J. Electrochem. Soc.* **2012**, *159* (6), A730.

(95) Leung, K.; Qi, Y.; Zavadil, K. R.; Jung, Y. S.; Dillon, A. C.; Cavanagh, A. S.; Lee, S. H.; George, S. M. Using Atomic Layer Deposition to Hinder Solvent Decomposition in Lithium Ion Batteries: First-Principles Modeling and Experimental Studies. *J. Am. Chem. Soc.* **2011**, *133* (37), 14741–14754.

(96) Méndez, E.; Elola, M. D.; Rodriguez, J.; Laria, D. Equilibrium and Dynamical Characteristics of the Solvation Associated with the Li+/Li Redox Couple at the Ethylene Carbonate/Graphene Interface. *J. Phys. Chem. C* **2021**, *125* (12), 6694–6707.

(97) Kim, J.; Savoie, B. M.; Miller, T. F. Interfacial Electron Transfer and Ion Solvation in the Solid Electrolyte Interphase. *J. Phys. Chem. C* **2021**, *125* (8), 4614–4622.

(98) Blumberger, J. Recent Advances in the Theory and Molecular Simulation of Biological Electron Transfer Reactions. *Chem. Rev.* **2015**, *115* (20), 11191–11238.

(99) Fraggedakis, D.; Bazant, M. Z. Tuning the Stability of Electrochemical Interfaces by Electron Transfer Reactions. *J. Chem. Phys.* **2020**, *152* (18), 184703.

(100) Blumberger, J.; Tateyama, Y.; Sprik, M. Ab Initio Molecular Dynamics Simulation of Redox Reactions in Solution. *Comput. Phys. Commun.* **2005**, *169* (1–3), 256–261.

(101) Cheng, J.; Sprik, M. Alignment of Electronic Energy Levels at Electrochemical Interfaces. *Phys. Chem. Chem. Phys.* **2012**, *14* (32), 11245–11267.

(102) Marcus, R. A.; Sutin, N. Electron Transfers in Chemistry and Biology. *Biochim. Biophys. Acta* **1985**, *811* (3), 265–322.

(103) Marcus, R. A. Electron Transfer Reactions in Chemistry. Theory and Experiment. *Rev. Mod. Phys.* **1993**, *65* (3), 599–610.

(104) Marcus, R. A. Chemical and Electrochemical Electron-Transfer Theory. *Annu. Rev. Phys. Chem.* **1964**, *15*, 155–196.

(105) Marcus, R. A. On the Theory of Electron-Transfer Reactions. VI. Unified Treatment for Homogeneous and Electrode Reactions. *J. Chem. Phys.* **1965**, *43* (2), 679–701.

(106) Schmickler, W. A Theory of Adiabatic Electron-Transfer Reactions. *J. Electroanal. Chem.* **1986**, *204* (1–2), 31–43.

(107) Borodin, O.; Behl, W.; Jow, T. R. Oxidative Stability and Initial Decomposition Reactions of Carbonate, Sulfone, and Alkyl Phosphate-Based Electrolytes. *J. Phys. Chem. C* **2013**, *117* (17), 8661–8682.

(108) Borodin, O. Molecular Modeling of Electrolytes. In *Electrolytes for Lithium and Lithium-Ion Batteries*; Jow, T. R., Xu, K., Borodin, O., Ue, M., Eds.; Springer: New York, 2014; pp 371–401.

(109) Ben-Naim, A. Standard Thermodynamics of Transfer. Uses and Misuses. *J. Phys. Chem.* **1978**, *82* (7), 792–803.

(110) Hünenberger, P. H.; Reif, M. *Single-Ion Solvation: Experimental and Theoretical Approaches to Elusive Thermodynamic Quantities*; Royal Society of Chemistry, 2011.

(111) Duignan, T. T.; Baer, M. D.; Schenter, G. K.; Mundy, C. J. Electrostatic Solvation Free Energies of Charged Hard Spheres Using Molecular Dynamics with Density Functional Theory Interactions. *J. Chem. Phys.* **2017**, *147* (16), 161716.

(112) Duignan, T. T.; Baer, M. D.; Schenter, G. K.; Mundy, C. J. Real Single Ion Solvation Free Energies with Quantum Mechanical Simulation. *Chem. Sci.* **2017**, *8* (9), 6131–6140.

(113) Marenich, A. V; Cramer, C. J.; Truhlar, D. G. Universal Solvation Model Based on Solute Electron Density and on a Continuum Model of the Solvent Defined by the Bulk Dielectric

Constant and Atomic Surface Tensions. *J. Phys. Chem. B* **2009**, *113* (18), 6378–6396.

(114) Rose, D. A.; Benjamin, I. Molecular Dynamics of Adiabatic and Nonadiabatic Electron Transfer at the Metal-Water Interface. *J. Chem. Phys*. **1994**, *100* (5), 3545–3555.

(115) Straus, J. B.; Calhoun, A.; Voth, G. A. Calculation of Solvent Free Energies for Heterogeneous Electron Transfer at the Water-Metal Interface: Classical versus Quantum Behavior. *J. Chem. Phys.* **1995**, *102* (1), 529–539.

(116) Kuharski, R. A.; Bader, J. S.; Chandler, D.; Sprik, M.; Klein, M. L.; Impey, R. W. Molecular Model for Aqueous Ferrous-Ferric Electron Transfer. *J. Chem. Phys.* **1988**, *89* (5), 3248–3257.

(117) Abraham, M. J.; Murtola, T.; Schulz, R.; Páll, S.; Smith, J. C.; Hess, B.; Lindahl, E. GROMACS: High Performance Molecular Simulations through Multi-Level Parallelism from Laptops to Supercomputers. *SoftwareX* **2015**, *1–2*, 19–25.

(118) McDonald, N. A.; Jorgensen, W. L. Development of an All-Atom Force Field for Heterocycles. Properties of Liquid Pyrrole, Furan, Diazoles, and Oxazoles. *J. Phys. Chem. B* **1998**, *102* (41), 8049–8059.

(119) Rizzo, R. C.; Jorgensen, W. L. OPLS All-Atom Model for Amines: Resolution of the Amine Hydration Problem. *J. Am. Chem. Soc.* **1999**, *121* (20), 4827–4836.

(120) Price, M. L. P.; Ostrovsky, D.; Jorgensen, W. L. Gas-Phase and Liquid-State Properties of Esters, Nitriles, and Nitro Compounds with the OPLS-AA Force Field. *J. Comput. Chem.* **2001**, *22* (13), 1340–1352.

(121) Chaudhari, M. I.; Muralidharan, A.; Pratt, L. R.; Rempe, S. B. Assessment of Simple Models for Molecular Simulation of Ethylene Carbonate and Propylene Carbonate as Solvents for Electrolyte Solutions. *Top. Curr. Chem.* **2018**, *376* (2), 7.

(122) Krishnan, R.; Binkley, J. S.; Seeger, R.; Pople, J. A. Self-Consistent Molecular Orbital Methods. XX. A Basis Set for Correlated Wave Functions. *J. Chem. Phys.* **1980**, *72* (1), 650–654.

(123) Clark, T.; Chandrasekhar, J.; Spitznagel, G. W.; Schleyer, P. V. R. Efficient Diffuse Function-augmented Basis Sets for Anion Calculations. III. The 3-21+G Basis Set for First-row Elements, Li–F. *J. Comput. Chem.* **1983**, *4* (3), 294–301.

(124) Raiteri, P.; Demichelis, R.; Gale, J. D. Thermodynamically Consistent Force Field for Molecular Dynamics Simulations of Alkaline-Earth Carbonates and Their Aqueous

Speciation. *J. Phys. Chem. C* **2015**, *119* (43), 24447–24458.

(125) Krack, M. Pseudopotentials for H to Kr Optimized for Gradient-Corrected Exchange-Correlation Functionals. *Theor. Chem. Acc.* **2005**, *114* (1–3), 145–152.

(126) Hartwigsen, C.; Goedecker, S.; Hutter, J. Relativistic Separable Dual-Space Gaussian Pseudopotentials from H to Rn. *Phys. Rev. B - Condens. Matter Mater. Phys.* **1998**, *58* (7), 3641–3662.

(127) Lippert, G.; Hutter, J.; Parrinello, M. A Hybrid Gaussian and Plane Wave Density Functional Scheme. *Mol. Phys.* **1997**, *92* (3), 477–488.

(128) Goedecker, S.; Teter, M. Separable Dual-Space Gaussian Pseudopotentials. *Phys. Rev. B - Condens. Matter Mater. Phys.* **1996**, *54* (3), 1703–1710.

(129) Subotnik, J. E.; Cave, R. J.; Steele, R. P.; Shenvi, N. The Initial and Final States of Electron and Energy Transfer Processes: Diabatization as Motivated by System-Solvent Interactions. *J. Chem. Phys.* **2009**, *130* (23), 244101.

(130) Blumberger, J.; Sprik, M. Ab Initio Molecular Dynamics Simulation of the Aqueous Ru 2+/Ru3+ Redox Reaction: The Marcus Perspective. *J. Phys. Chem. B* **2005**, *109* (14), 6793–6804.

(131) Duignan, T. T.; Kathmann, S. M.; Schenter, G. K.; Mundy, C. J. Toward a First-Principles Framework for Predicting Collective Properties of Electrolytes. *Acc. Chem. Res.* **2021**, *54* (13), 2833–2843.

(132) Angarita-Gomez, S.; Balbuena, P. B. Solvation vs. Surface Charge Transfer: An Interfacial Chemistry Game Drives Cation Motion. *Chem. Commun.* **2021**, *57* (50), 6189–6192.

(133) Dean, J. A. *Lange's Handbook of Chemistry*, 15th ed.; McGraw-Hill, 1999.

(134) Novák, P.; Joho, F.; Imhof, R.; Panitz, J. C.; Haas, O. In Situ Investigation of the Interaction between Graphite and Electrolyte Solutions. *J. Power Sources* **1999**, *81–82*, 212–216.

(135) Busch, M.; Ahlberg, E.; Laasonen, K. From Absolute Potentials to a Generalized Computational Standard Hydrogen Electrode for Aqueous and Non-Aqueous Solvents. *Phys. Chem. Chem. Phys.* **2021**, *23* (20), 11727–11737.

(136) Zhang, X.; Kostecki, R.; Richardson, T. J.; Pugh, J. K.; Ross, P. N. Electrochemical and Infrared Studies of the Reduction of Organic Carbonates. *J. Electrochem. Soc.* **2001**, *148* (12), A1341.

(137) Baskin, A.; Prendergast, D. Exploring Chemical Speciation at Electrified Interfaces Using

Detailed Continuum Models. *J. Chem. Phys.* **2019**, *150* (4), 41725.

(138) Wang, Z.; Yang, Y.; Olmsted, D. L.; Asta, M.; Laird, B. B. Evaluation of the Constant Potential Method in Simulating Electric Double-Layer Capacitors. *J. Chem. Phys.* **2014**, *141* (18), 184102.

(139) Futera, Z.; Blumberger, J. Electronic Couplings for Charge Transfer across Molecule/Metal and Molecule/Semiconductor Interfaces: Performance of the Projector Operator-Based Diabatization Approach. *J. Phys. Chem. C* **2017**, *121* (36), 19677–19689.

(140) Carter-Fenk, K.; Mundy, C. J.; Herbert, J. M. Natural Charge-Transfer Analysis: Eliminating Spurious Charge-Transfer States in Time-Dependent Density Functional Theory via Diabatization, with Application to Projection-Based Embedding. *J. Chem. Theory Comput.* **2021**, *17* (7), 4195–4210.

(141) Bazant, M. Z. Theory of Chemical Kinetics and Charge Transfer Based on Nonequilibrium Thermodynamics. *Acc. Chem. Res.* **2013**, *46* (5), 1144–1160.

(142) Rustam, S.; Intan, N. N.; Pfaendtner, J. Effect of Graphitic Anode Surface Functionalization on the Structure and Dynamics of Electrolytes at the Interface. *J. Chem. Phys.* **2021**, *155* (13), 134702.

(143) Dang, L. X.; Sun, X.; Ginovska-Pangovska, B.; Annapureddy, H. V. R.; Truong, T. B. Understanding Ion-Ion Interactions in Bulk and Aqueous Interfaces Using Molecular Simulations.

(144) Ensing, B.; Meijer, E. J.; Blöchl, P. E.; Baerends, E. J. Solvation Effects on the SN2 Reaction between CH3Cl and Cl- in Water. *J. Phys. Chem. A* **2001**, *105* (13), 3300–3310.

(145) Leitold, C.; Mundy, C. J.; Baer, M. D.; Schenter, G. K.; Peters, B. Solvent Reaction Coordinate for an SN2 Reaction. *J. Chem. Phys.* **2020**, *153* (2), 024103.

(146) Peters, B. Reaction Coordinates and Mechanistic Hypothesis Tests. *Annu. Rev. Phys. Chem.* **2016**, *67* (1), 669–690.

(147) Peters, B.; Trout, B. L. Obtaining Reaction Coordinates by Likelihood Maximization. *J. Chem. Phys.* **2006**, *125* (5).

(148) Grossfield, A. WHAM: The Weighted Histogram Analysis Method.

(149) Martinez, L.; Andrade, R.; Birgin, E. G.; Martínez, J. M. PACKMOL: A Package for Building Initial Configurations for Molecular Dynamics Simulations. *J. Comput. Chem.* **2009**, *30* (13), 2157–2164.

(150) Peters, B. *Reaction Rate Theory and Rare Events*; Elsevier: Amsterdam, The Netherlands, 2017.

(151) Tiwary, P.; Parrinello, M. From Metadynamics to Dynamics. *Phys. Rev. Lett.* **2013**, *111* (23), 1–5.

(152) Ells, A. W.; May, R.; Marbella, L. E. Potassium Fluoride and Carbonate Lead to Cell Failure in Potassium-Ion Batteries. *ACS Appl. Mater. Interfaces* **2021**, *13*, 53841–53849.

(153) Gibson, L. D.; Pfaendtner, J.; Mundy, C. J. Probing the Thermodynamics and Kinetics of Ethylene Carbonate Reduction at the Electrode-Electrolyte Interface with Molecular Simulations. *J. Chem. Phys.* **2021**, *155*, 204703.